

EXPERIMENTAL STUDIES OF THE INFLUENCE OF THE PROPERTIES OF
THE MATRIX OF A DEBRIS FLOW ON ITS EROSIONAL BEHAVIOR

A THESIS

SUBMITTED TO THE FACULTY OF
UNIVERSITY OF MINNESOTA

BY

JARED MULLENBACH

IN PARTIAL FULFILLMENT OF THE REQUIREMENTS
FOR THE DEGREE OF MASTER OF SCIENCE

ADVISOR: KIMBERLY HILL

March 2018

© Jared Mullenbach 2018

Acknowledgements

Before beginning, I would like to extend my appreciation to the individuals who made this work possible: to my adviser, Dr. Kimberly Hill, your knowledge and guidance was essential to my success and completion of my MS and corresponding thesis; to Anthony Longjas, Amirreza Ghasemi, Feng Qingfeng, and Paul Fritton for assistance in research and experiment completion; to my committee members, Dr. Voller and Dr. Paola, whom make this completion possible; to my parents, I owe everything to your ever long encouragement and dedication to me; to my friends and family, I thank you for your endless support and friendship.

You are all so important to me.

Dedication

For my sister,

Your persistent correction was my key to learning

Now it is my key to researching in life

Table of Contents

List of Tables.....	v
List of Figures.....	vi
1 Introduction.....	1
1.1 Debris flow properties and dynamics	1
1.2 Interstitial fluids: fines content; excess pore pressure, and other dynamics	6
1.3 Entrainment of bed material by debris flows.....	9
1.4 Focus of experimental debris flow studies	11
2 Methods	13
2.1 Experimental design	13
2.1.1 Table top debris flow flume	13
2.1.2 Particles.....	14
2.1.3 Interstitial fluid.....	16
2.1.4 Instrumentation	17
2.2 Procedure	19
2.3 Experimental Conditions	20
2.3.1 Neutral Angle.....	21
2.3.2 Viscosity Dependence.....	22
2.4 Data Analysis.....	23
2.4.1 Video Analysis.....	23
2.4.2 Pore fluid pressure analysis	38
2.5 Scaling and Similitude	41
2.5.1 Rationale for Dimensional Analysis.....	41
2.5.2 Debris Flow Variables.....	42
3 Results: effects of interstitial fluid viscosity on entrainment dynamics	47
3.1 Net erosion.....	47
3.2 Instantaneous entrainment rate	50
3.3 Measures of Proposed Erosion Drivers	56

3.3.1	Bed shear stress	57
3.3.2	Granular temperature at bed-flow interface	59
3.3.3	Pore Fluid Pressure	60
4	Discussion of laboratory experiments.....	67
4.1	Implications of m_e results for measures of real debris flow dynamics and hazards.....	70
4.1.1	Relative m_e Insensitivity to Interstitial Fluid Viscosity	70
4.1.2	Neutral Angle Dependence on Viscosity	71
4.2	Dependence on Entrainment Dynamics on Viscosity.....	71
4.2.1	Entrainment depth and rate	72
4.2.2	Shear stress and granular temperature	73
4.2.3	Pore fluid pressure	74
5	Field Results	83
5.1	Summary of Area.....	84
5.2	Fan analysis	89
5.2.1	Relation to Lab data	94
6	Summary and Outlook.....	96
	References.....	99
	Appendix.....	104
I.	Definition of symbols	104
II.	Field Locations and descriptions	106

List of Tables

<i>Table 2-1</i>	15
<i>Table 2-2</i>	16
<i>Table 2-3</i>	19
<i>Table 2-4</i>	22
<i>Table 2-5</i>	23
<i>Table 2-6</i>	43
<i>Table 2-7</i>	44
<i>Table 2-8</i>	45
<i>Table 3-1</i>	49

List of Figures

<i>Figure 1-1</i>	4
<i>Figure 2-1</i>	14
<i>Figure 2-2</i>	15
<i>Figure 2-3</i>	197
<i>Figure 2-4</i>	19
<i>Figure 2-5</i>	25
<i>Figure 2-6</i>	28
<i>Figure 2-7</i>	29
<i>Figure 2-8</i>	30
<i>Figure 2-9</i>	32
<i>Figure 2-10</i>	33
<i>Figure 2-11</i>	34
<i>Figure 2-12</i>	35
<i>Figure 2-13</i>	36
<i>Figure 2-14</i>	37
<i>Figure 2-15</i>	39
<i>Figure 2-16</i>	39
<i>Figure 2-17</i>	40
<i>Figure 3-1</i>	49
<i>Figure 3-2</i>	50
<i>Figure 3-3</i>	51
<i>Figure 3-4</i>	53
<i>Figure 3-5</i>	54
<i>Figure 3-6</i>	55
<i>Figure 3-7</i>	56
<i>Figure 3-8</i>	57
<i>Figure 3-9</i>	58
<i>Figure 3-10</i>	60
<i>Figure 3-11</i>	61

Figure 3-12..... 62
Figure 3-13..... 64
Figure 3-14..... 66
Figure 3-15..... 67
Figure 4-1..... 76
Figure 4-2..... 77
Figure 4-3..... 78
Figure 4-4..... 80
Figure 4-5..... 81
Figure 4-6..... 82
Figure 5-1..... 85
Figure 5-2..... 86
Figure 5-3..... 86
Figure 5-4..... 87
Figure 5-5..... 87
Figure 5-6..... 88
Figure 5-7..... 90
Figure 5-8..... 91
Figure 5-2..... 92

1 Introduction

Debris flows – massive flows of fluid and particles – create significant hazard for communities established in or near mountainous regions. The destructive potential of debris flows is well documented throughout the world; in Japan, an average of 90 lives per year are lost [Takahashi, 1981] and in 1985, British Columbia saw over \$100 million dollars of damage to property and transportation losses [Hungry *et. al.*, 1987]. There is evidence that the frequency of debris flows and hazards associated with them are increasing associated with changes in macro and micro climate and in land use, resulting in modification in rainfall patterns and changes in local sediment supply (e.g., [Pierce *et al.*, 2004; Stoffel and Beniston, 2006; Floris *et al.*, 2010]). Thus there is an increasing need for models that can mechanistically account for the manner in which physical parameters give rise to certain debris flow behaviors.

Debris flow modeling is undergoing exciting growth [e.g., Iverson and Denlinger, 2001; Bouchut *et al.*, 2014]. However, the mechanics of several factors that influence associated landscape evolution and hazard prediction are not understood. In particular, the “bulking up” process of debris flows, that is, the entrainment of loose sediment, and the counterpart, deposition, are important in their influence on the mobility of the flow itself. A better understanding of the particle dynamics associated with these processes is needed for debris flows where particle interactions are first order effects, for example, in “stony” debris flows [Shieh *et al.*, 1996] and the snout of a typical debris flow [Stock and Dietrich, 2006]. In this Chapter, we first review basic properties and behaviors of debris flows and then describe current understanding of entrainment processes that influence growth rate and geomorphological influence of debris flows.

1.1 Debris flow properties and dynamics

The debris flows that are the focus of this thesis form in steep upland regions when there is both sufficient fluid (e.g., from a recent or concurrent rainfall) and loose particles along the path of the flow (e.g., from recent or ongoing tectonic activity and local rockfalls and landslides). Particles can range in size from microns, e.g., clay and silt, to meters, e.g., boulders [Takahashi, 1981]. Flows are initiated when water runs through sediment with a sufficiently quantity of fine particles to mobilize coarser particles, as detailed below. In response to a sufficiently steep slope, a mixture of particles and fluids travel in something resembling a single-phase flow rather than a bedload or suspended load transport of particles, [Hungr, 2005]. In other words, debris flows are unique because they move much like a fluid even if they contain boulder-sized particles.

Historically, the dynamic behavior of debris flows has been represented by a relatively simple rheology. The simplest that have been commonly used to represent full 3-D flow of these multiphase systems is a Bingham rheology:

$$\tau = \tau_y + k_B \dot{\gamma} \quad (1.1)$$

In this equation, τ_y represents the yield stress, below which there is no movement, and k_B (often referred to as a *plastic* viscosity) is an empirically determined parameter that indicates the sensitivity of the shear rate $\dot{\gamma}$ to additional shear stress, τ .

The slightly more complex Herschel-Bulkley model has also been used to represent movement in the fluid matrix [Coussot, 1996; Mueller et al., 2009],

$$\tau = \tau_y + k_{HB} \dot{\gamma}^a \quad (1.2)$$

In this equation, again, τ is the local shear stress [Pa], τ_y is yield stress [Pa], k_{HB} [$Pa \times s^a$] is known as the *consistency* index (an empirical parameter), $\dot{\gamma}$ is the shear rate [s^{-1}], and a is a power law exponent. τ_y , k_{HB} , and a are all empirically determined parameters. When $a > 1$, the flow is shear thickening and when $0 < a < 1$ the flow is shear-thinning. If $a=1$, the flow is essentially Bingham, and the consistency index is replaced by the plastic viscosity [Major, 1992].

Iverson [2003] suggested that it is qualitatively as well as quantitatively unrealistic to represent a debris flow by a single rheological model. Specifically, he described the Bingham model, based on Coulomb strength, as accurate only for flows of mud slurries, not the significantly more complex particle-fluid dynamics that arise with the addition of high concentrations of particles larger than sand. He pointed out that in these cases, as a debris flow evolves, the strength (i.e., yield stress) is constantly changing due to the fluctuations in pore pressure as the flow progresses.

Capturing all this additional complexity in an already complex topography is extremely difficult. Indeed, while full three dimensional models that account for local rheologies as in Equations 1 and 2 may be most ideal for simulating debris flows, they are computationally expensive. In their place, computationally efficient depth-averaged models have been proposed to mechanistically deal with natural geophysical flows (e.g., Iverson, 2012; Bouchut *et al.*, 2014). With a few assumptions the conservation of mass and downslope momentum conservation equations take the form of (e.g., Iverson 2012):

$$\frac{\partial h}{\partial t} + \frac{\partial(h\bar{v}_x)}{\partial x} = \dot{e} \quad (1.3)$$

$$\rho \left[\frac{\partial(h\bar{v}_x)}{\partial t} + \frac{\partial(h\bar{v}_x^2)}{\partial x} \right] = \int_{z_{1bot}}^{z_{1top}} (\Sigma F) dz + \rho v_{x,bot} \dot{e} \quad (1.4)$$

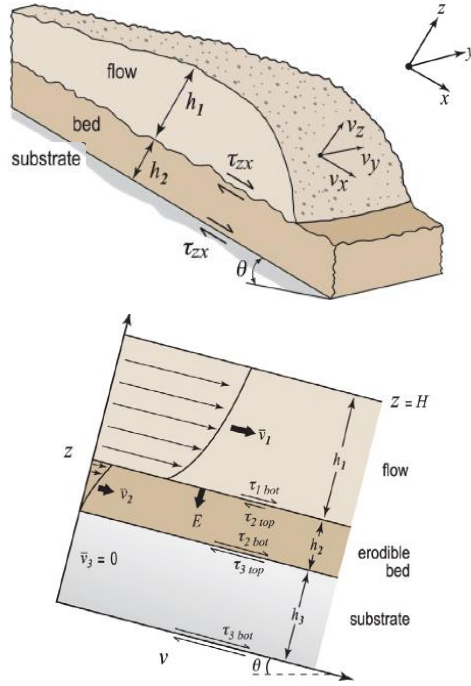


Figure 1-1: Illustration of a cross section of a debris flow over an erodible bed from Iverson [2012], (top) with erosion rate E (notated as \dot{e} , throughout this thesis) illustrated, (bottom).

where the variables are as illustrated in **Figure 1-1**: F is the net force per unit volume on a “slab” of debris flow; $v_{x,bot} = v_x(z = z_{bot})$, and the overbar indicates an integration over the depth of the flow. f includes the weight of the flowing mass, frictional interaction with the bed, and differential pressure, such as due to a gradient in the thickness.

This expression in **Equation 1.4** allows for a more detailed view of how particle-fluid dynamics influence the flow behavior. In particular, Iverson [2012] expressed the total local force in the downslope direction $F_{tot} = \int_{z_{1bot}}^{z_{1top}} (\Sigma F) dz A$ according to:

$$F_{tot} \approx [\rho g h \sin \theta - \rho g h (\delta h / \delta x) - \tau] A \quad (1.5)$$

In this equation, the first term is the weight, the second is the pressure differential, and the final is the shear stress. A represents the local contact area of the flow; ρ [kg/m³] is

the bulk density ($\rho = \rho_s(1 - \eta) + \rho_f\eta$) of the flow and τ is the resistive stress of the particles in the bed. In a particulate system, this resistive stress at the bed is often modelled using a Coulomb friction law as Bagnold first did [Bagnold, 1954]:

$$\tau = \mu_c \sigma_{eff} \quad (1.6)$$

Here, σ_{eff} is considered the normal stress borne by the particles associated with the weight of the particles alone, and μ_c is a Coulomb friction coefficient. When an interstitial fluid is present, the normal stress borne by the particles can be significantly reduced. According to Terzaghi's [1943] effective stress principle, this effect is modelled according to:

$$\sigma_{eff} = \sigma_{tot} - P \quad (1.7)$$

where σ_{tot} is the total normal stress from bulk density, and P is the pore fluid pressure. In a simple flow, P can be represented by the hydrostatic fluid pressure P_{hyd} at the base of the flow:

$$P_{hyd} = \rho_f g h \cos\theta \quad (1.8)$$

and the stresses may be represented according to the depth-integrated weight of the particles and fluid in the overlying flow so that:

$$\sigma_{tot} = \rho g h \cos\theta \quad (1.9a)$$

$$\sigma_{eff} = (\rho - \rho_f) g h \cos\theta \quad (1.9b)$$

On the other hand, if the pore fluid pressure is increased for some reason, the effective stress borne by interparticle contacts can be reduced significantly. In a debris flow, minimally, P is increased through the suspension of fine particles in the interstitial fluid, effectively increasing the buoyancy force on the fluids. Many have posited that P may

also be increased through dynamic effects induced by the nature of the jostled and sheared particles in the fluid.

The effect of the properties of the interstitial fluid in general and dynamics that lead to increased pore pressure in particular are sufficiently important for the topics of this thesis that we focus the next section on specific quantities that govern these details.

1.2 Interstitial fluids: fines content; excess pore pressure, and other dynamics

The interstitial fluid properties of a debris flow are particularly important for governing their dynamics and distinguishing them from sediment transporting flows (such as debris floods). The feature that is typically identified with this involves the suspension of fine particles. Specifically fine particles do not settle over the duration of a debris flow (e.g., *Major*, [1992]). Because of this, they become part of the interstitial fluid even though, in reality, they are solid particles. Those that may be considered in the “suspended” category may even be particles as large as sand-sized or pebble-sized particles [*Kaitna et al.*, 2016]. As the particles are part of the fluid, both the effective viscosity and density may increase. This can alter the bulk debris flow behavior in many ways. Here we focus on the manner in which it affects the effective stress directly through the interstitial fluid density (**Equation 1.7**) and indirectly through what might be called an “excess pore pressure”.

The changes in interstitial fluid that affect the pore fluid pressure and, subsequently, the effective stress involve both density and viscosity of the interstitial fluid. As the fluid density increases, so does the hydrostatic pressure, trivially increasing the pore fluid pressure expressed in **Equation 1.8**. According to **Equation 1.7** this increase in P results in a decrease in σ_{eff} , therefore decreasing the resistive stress on the flow from the bed, τ (**Equation 1.5**).

An increase in viscosity affects the local pore fluid pressure somewhat differently and in a way not completely yet quantified. To describe this, it is helpful to think about a very locally variable pressure gradient that arises from the natural jostling that occurs among particles in these sheared flows. As Bagnold [1954] described, particles are not simply shearing in layers as could be conceptualized in a laminar-like (layered) flow, rather, they undergo a series of collisions. In a particle-fluid flow, when the particles *would* otherwise collide, a larger pressure gradient can build among the particles that could prevent this. Depending on the viscosity of the fluid that is under pressure, the interstitial fluid flow will respond to the pressure gradients differently,

When particles approach one another with what might have been a relatively fast collision with air as the interstitial fluid, fluids with a higher viscosity or those with a more complex rheology may mitigate this situation. For example, a higher viscosity fluid responds more slowly to increasing pore pressure gradients associated with particles approaching one another. An interstitial fluid with a less viscous fluid will flow more quickly in response to the associated changing pressure gradient than a higher viscosity fluid [e.g., *Darcy* [1856] experiments on pressure head and conductivity]. This results in a sustained local excess pore pressure, P_e , and reduced interparticle contacts. If the interstitial fluid viscosity is sufficiently high, we posit that the particle-particle contact will be further reduced, and the excess pore pressure may replace Bagnold's [1954] collisional pressure in suspending particles, preventing them from contacting. In this case, the weight of the particles that would otherwise be borne by interparticle contacts (collisions), instead is borne by the fluid, increasing the local pore fluid pressure indirectly. While there are differing opinions as to whether or not this could occur in steady flows (e.g., *Mangeney*, [2009]), there is some evidence that it is important (e.g., *Pierson*, [1981] & *Kaitna et al.*, [2016]).

This process has been observed previously in debris flows when *Pierson* [1981] showed that there could be an average pore fluid pressure greater than the hydrostatic pressure

over the duration of a debris flow. He posited also that the pore pressure is maintained because the poor sorting restricts the fluid from moving quickly, suggesting that grain size distribution affects the pore fluid pressure. *Kaitna et al.* [2016] found that as fines increase in the interstitial fluid, the excess pore pressure (at times, beyond that indicated by the density of the suspension alone) increases most significantly.

While this effect is plausible, the details are very much in contention (Iverson, [1997], *Mangeney*, 2009, *Kaitna et al.*, 2016). One of the reasons for the disagreement in the literature is likely rooted in the difficulty to systematically study the effect of varying fine particles on the flow behavior. Using fine particles like clay and silt would obscure details needed to measure local and global dynamics. A notable guide for doing this effectively comes from statements such as those in *Iverson* [1997], indicating that the viscosity of a typical field-scale pore fluid is between 10^{-3} Pa-s (water, few fines) and 10^{-1} Pa-s (thicker fluid with higher fine particle fraction). While the rheology of the interstitial fluid may strictly be more complex than this Newtonian viscosity representation implies, this provides some help to experimentalists interested in this effect. Simply, to first order, viscous effects of fine particles in the interstitial fluid may be represented by simply changing the viscosity of the interstitial fluid via mixtures of different fluids that maintain the non-opacity of water alone.

In addition to the effect of suspension of fine particles on the effective pore fluid pressure, there are other details of the flow dynamics likely changed. Most significant is the fact that the addition of fine particles into what otherwise may be water alone as the interstitial fluid is typically accredited for causing the particles and fluid to move together as a nearly single phase [*Whipple and Dunne*, 1992]. *Enos* [1977] posits that the strength of a debris flow is tied directly to the percentage of matrix contained within the flow with more matrix correlating with an increased strength; this is due to the fines holding in pore fluid pressure [*Major*, 1996]. The interstitial fluid rheology may also have a direct effect on the entrainment rate ($\dot{\epsilon}$ in **Equation 1.3**). These relationships are much less well

established; we focus primarily on the effect of the varying interstitial fluid properties on the entrainment rate in this thesis.

1.3 Entrainment of bed material by debris flows

Also, debris flows often have a viscous pore fluid that gathers up more and more material, or entrains, as it carves through channels or down slopes [Iverson, 1997]. More entrainment has been found to be correlated with more destructive flows [Stiny, 1910]. The evolution and growth of a flow can be related to many different properties. Initial topography, grain size distribution, local relief, lithology, and water content are a few of the known factors [described in, for example, Varnes, [1978]; Whipple and Dunne, [1992]; Pierson and Costa, [1987]. The physical mechanisms that govern the growth of the flow, or entrainment itself are still unclear and may be due to the collision of grains, friction between grains, and viscosity of the fluid [Iverson, 1997].

Entrainment of bed material by debris flows has been attributed to several mechanisms. One way to understand how the flow picks up more material is to delve into the analysis of the micro-scale grain-grain collisions. As more collisions occur, more particles begin moving and the depth of the movement of particles and flow increases. In this thesis, we attempt to explain why the position of this stationary-moving interface is accelerating or decelerating as the flow progresses. Analysis of the instantaneous direction and velocity of individual particles and their relationship with surrounding particles and fluid change enables us to describe how different factors such as bulk density [Iverson, 1997], granular temperature [Iverson, 1997], and basal pore-fluid pressure [Major and Iverson, 1999; Kaitna et al., 2016] affect debris flows. In this thesis, the main focus will be on pore fluid pressure.

Model work has advanced significantly in terms of its representation of the relationship between erosion rates and flow dynamics, such as mobility [Iverson, 2015]. However, the dominant influences of the erosion rate are still much in question. Bouchaud [1994]

proposed that the erosion rate \dot{e} is proportional to the local flow depth and the difference between the angle of inclination and a neutral angle, an angle for which no net deposition or entrainment would occur. *Boudreaux* [2010] proposed that for thick enough flows \dot{e} is independent of flow thickness, but dependent on the difference between the angle of inclination and a neutral angle. *Pitman* [2005] proposed that \dot{e} is proportional to the local depth-averaged flow velocity. Through different means, *Fraccarollo* [2005] and *Iverson* [2012] derived a form for \dot{e} that included shear stresses and velocities associated with the flow and bed.

While most of the theoretical development has focused on details in the flow, there are notable exceptions. For example, *Jenkins* and *Berzi* [private communication, 2014], suggested that \dot{e} depends on “force chains”, i.e., correlated interparticle contacts in the bed, and the speed of disturbances that make or break these force chains. *Iverson* [2014] demonstrated how bed moisture could affect \dot{e} through the mobilizing effect of pore fluid pressures. Small-scale experiments have indicated important details of the bed as well. In particular, increasing the size of bed sediment size relative to that in the flow *Egashira* [2001] or changing the fraction of clay in the flow and bed [*deHaas*, 2015 and *deHaas*, 2016b] can influence entrainment rate. Laboratory flume experiments [*Mangeney et al.*, 2007 and *Farin et al.*, 2014] indicate bed compaction influences run-out distance and, likely, entrainment rates, supported by numerical simulations [*Mangeney et al.*, 2007, *Iverson*, 2000]. We have previously demonstrated how subtle differences in the bed induced by preparation or previous flows -- with no apparent difference in bed compaction -- can have dramatic differences on the net entrainment rate of bed particles by an experimental flow [*Hill*, 2013 and *Moberly*, 2015].

Field observations (e.g., in: the Italian Eastern Alps [*Berti*, 2000]), the Kazakhstan Chemolgan test site [*Rickenmann*, 2003], Illgraben, Switzerland [*McArdell*, 2007, *Berger*, 2011, *Schurch*, 2011], and Chalk Cliffs Colorado, U.S. [*McCoy*, 2012; *McCoy*, 2013] and large-scale physical experiments (e.g. *Iverson*, [2011]) have provided insights

as well, though not always in agreement. From these field data, measures of erosion rate were found to be correlated with bed stress, τ , [Iverson, 2015], velocity fluctuations [Berger, 2011] (such as granular temperature T , energy associated with velocity fluctuations), and basal pore fluid pressure [Iverson, 2012]. Typically, only net (not instantaneous) local entrainment is measurable, though there is growing potential for collecting these data through methods such as erodible sensors [Berger, 2011] and basal pore pressure sensors [Iverson, 2012]. While excess pore pressure has been primarily associated theoretically with friction on the flow, there is some evidence of its importance in erosion rates as well [Berger *et al.*, 2011].

1.4 Focus of experimental debris flow studies

The main goal of this thesis is to understand the effects of a changing interstitial fluid rheology on debris flows, primarily as it pertains to entrainment. To do so, we focus on the relatively simple problem of a changing interstitial fluid viscosity, rather than the grain size distribution (e.g., through fine particle content) of the whole flow or a more complex rheology. A greater understanding of this domain will give insight on first order details of a debris flow's physical characteristics and can aid in modeling debris flow dynamics and associated hazards. First, we will provide an in-depth discussion on our table-top experiments to determine effects of interstitial fluid viscosities on mono-sized particle-fluid flows in a (relatively) controlled environment. We focus on measures from high speed high resolution digital photography of the flow and pore pressure measurements to understand the interplay between pore pressure, interstitial fluid viscosity, and entrainment dynamics of relatively simple particle-fluid flows. Later a discussion on the field relationships between grain size distributions, taken from historical debris flows, on morphology will elucidate a relation to real world application of this work.

The rest of this thesis is organized as follows: Chapter 2 provides a description of our experimental setup and procedure and our data analysis techniques. In Chapter 3, we present the results from the analysis of our experimental data. In Chapter 4 we discuss how we have found varying the interstitial fluid viscosity effects bed entrainment by experimental debris flows and pore fluid pressure dynamics. In Chapter 5 we describe field grain size distribution results from a field site at Owen's Valley, California, and a brief relation of experimental to field data. Finally, in Chapter 6 we present a summary and our outlook for what next steps our results suggest for improving mechanistic understanding of debris flow dynamics.

2 Methods

In this chapter, we present the details of the experimental setup and experimental procedure as well as the particle tracking algorithms used for the data analysis. We also demonstrate how we measure specific debris flow metrics (e.g., entrainment height, entrainment rate, shear stress, granular temperature etc.) introduced in Chapter 1 that were investigated in this work.

2.1 Experimental design

2.1.1 Table top debris flow flume

The experimental debris flow flume has a metal base and transparent Plexiglas walls so that the flows may be monitored visually from the side walls. The base consists of two parts: an upper rigid bed and lower erodible bed (see **Figure 2-1** for dimensions). The flume contains a hinge at the downstream end and a steel link chain at the upstream end, connected to the ceiling; the angle of inclination is increased via steel link winch and has the ability to reach 30° . For these experiments, we performed experiments with the flume inclined to angles ranging from $15\text{-}18^\circ$. To emulate bed roughness in the field and to reduce particle slipping, sandpaper (grade 36) was affixed to the rigid bed. The base of the erodible bed is 0.077 m deeper than the rigid bed, effectively a container in which beads that could be eroded by the flow are contained. The transition between the rigid bed and the erodible bed is spanned by a mesh layer inclined at a 20° angle from the flume bed (see **Figure 2-1**). This minimizes excessive scour from particles leaving the rigid bed and allows for interstitial fluid to be pumped through the erodible bed.

For the “dam break” experiments we performed for this thesis, there are three release points along the rigid bed: IP1, IP1.5, and IP2. At each release point, there is a swinging

gate that may be pinned in place to constrain an initial supply of particles or pinned upward to allow for the passage of particles. At the beginning of a particular experiment, the constraining gate is pivoted about its hinge, swiveling down-flume, to release the constrained particles.

A tube connects the fluid from a pump submerged in fluid in a container at the downstream end in the flume to a nozzle located at the upstream end of the erodible bed. In this way, the fluid in the bed may be controlled separately from that in the supply.

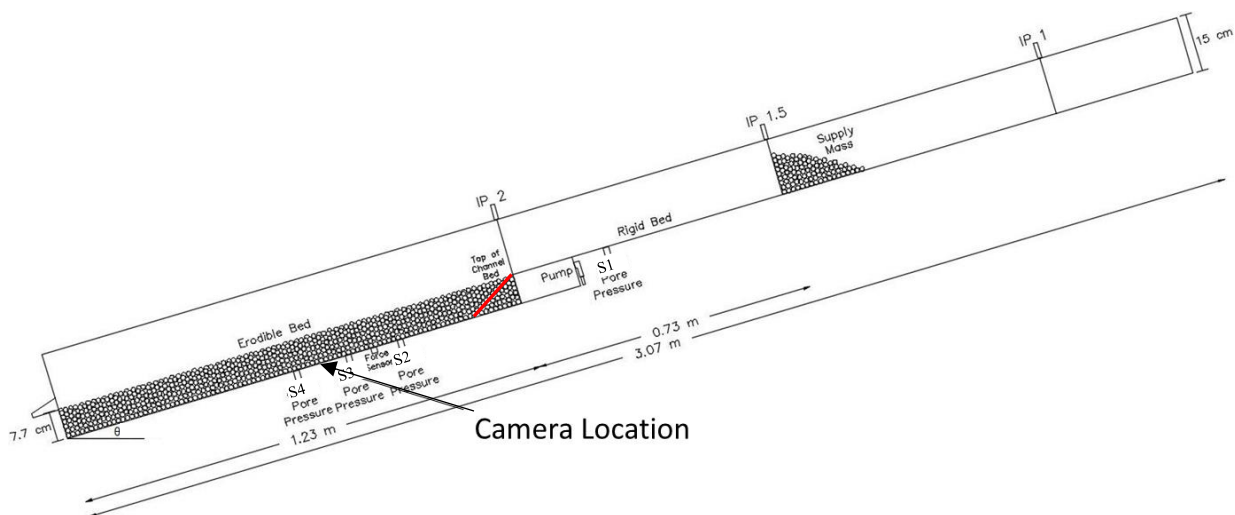


Figure 2-1. Sketch of debris flow flume. IP 1.5 (initial position) is the position of experimentation. The lengths of each experimental dimension are listed here and the instrumentation dimensions on Table 1. Notice the mesh layer (red) that protects from scour.

2.1.2 Particles

We use Zirconium Silicate beads (Quackenbush Co.) for the experiments described here because the opacity and near-sphericity was helpful for optimizing our particle tracking algorithm (**Table 2-1**). Additionally, the higher density (compared with natural particles) allowed for inertial effects to be closer to that of natural debris flows (**Table 2-1**). Spherical particles are commonly used for simplification in this field [Yohannes *et al.*, 2012; Mangeney *et al.*, 2010; Farin *et al.*, 2013, Moberly, 2015].

Table 2-1. Bead properties. Note that density and diameter are based on the values provided by the manufacturer. We determined the coefficient of restitution and approximate shape.

Bead Properties	Zirconium Silicate
bead diameter (m)	0.002
material density (kg/m ³)	4100
Coefficient of Restitution	0.9
Shape	subspherical

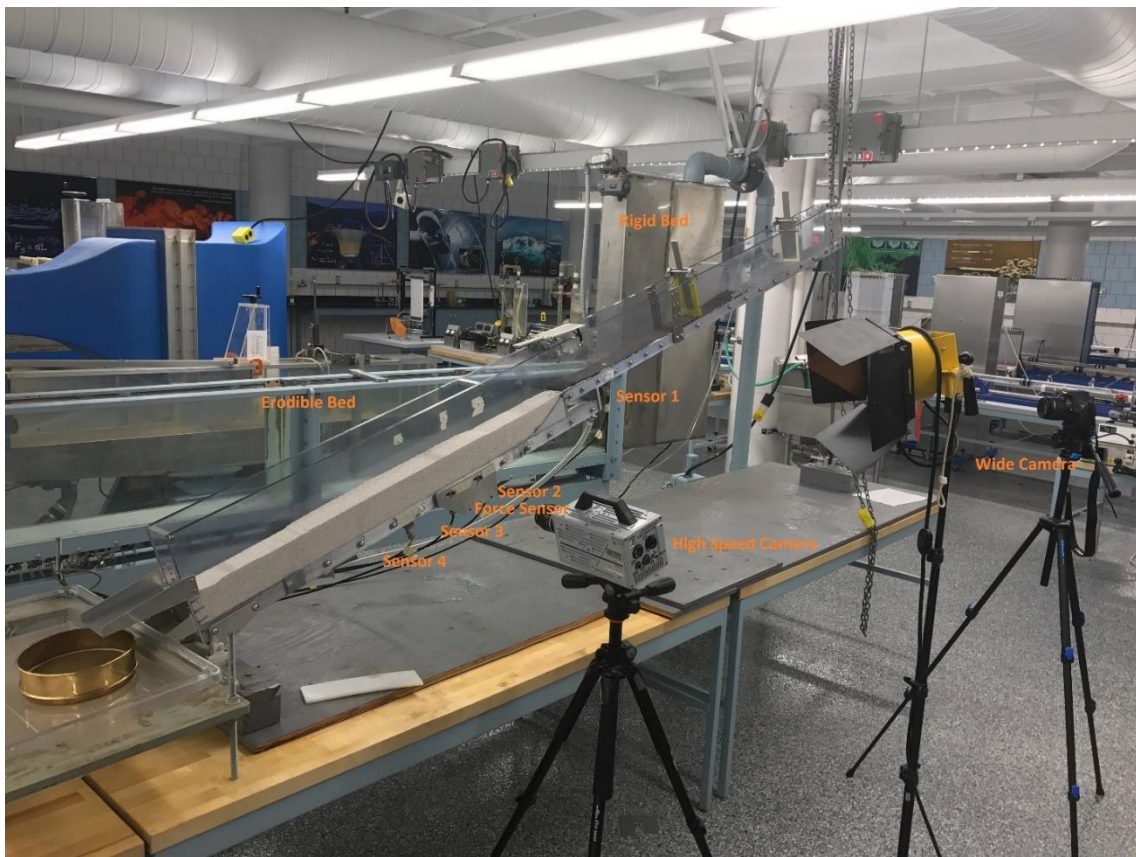


Figure 2-2. Setup of Experimental Flume located in the Ed Bowers Fluid Mechanics Lab in the Civil Engineering Building at the University of Minnesota.

2.1.3 Interstitial fluid

As discussed in Chapter 1, rather than investigating the explicit effect of different concentrations of fine particles, we investigate a representative effect of those fines, primarily in their influence on the viscosity of the interstitial fluid [Iverson, 1997]. To generate different viscosities for these experiments, rather than adding different concentrations of fine particles within the flow, we used mixtures of glycerol and water. To generate specific viscosities, we modified the ratio of glycerol to water content in the supply and erodible bed. In this study, we used water for 1 cP fluid and added different amounts of glycerin to generate 5, 12, 19, 25, 50, and 62 cP for the viscosity of interstitial fluid (densities and viscosities in **Table 2-2**). To generate an accurate viscosity reading, we used a Brookfield Viscometer (**Figure 2-3**). Viscosity measurements were taken prior to and immediately following experiments to identify discrepancies.

Table 2-2. Viscosities and densities for interstitial fluids used in our experiments. Note that all temperatures are kept near 20° C. Note that the numbers in this table are from Cheng [2008], the measured viscosities in our experiments are in Table 2. The viscosity was completed using a known supply of glycerin and water and combined, mixed well, and tested via a viscometer (**Figure 2-3**).

Water (% by vol)	Glycerin (% by vol)	% glycerin by mass	Density, ρ (kg/m ³)	Dynamic visc., μ (cP)
100	0	0	998	1
59	41	46.8	1107	5
43	57	62.5	1147	12
36	64	69	1163	19
34	66	71.1	1173	25
25	75	79.2	1197	50
24	74	80	1200	62



Figure 2-3. The Brookfield Viscometer used pre- and post- experimentation.

2.1.4 Instrumentation

To monitor flow dynamics, we used two cameras, four basal pore fluid pressure sensors, one basal force sensor, and a digital scale. We used a Canon Rebel T5 camera to record the macroscopic flow at the vicinity of the rigid bed. The relatively low-speed low-resolution recording allows us to record dynamics throughout the experiment over a relatively wide range of the experiment. However, since the temporal and spatial resolution are poor we cannot derive detailed particle scale dynamics from the images captured from this camera. We use a high-resolution high-speed camera to monitor dynamics relevant to particle-scale interactions near the erodible bed (Photron FASTCAM SA series). For all experiments described in this thesis, the high speed camera was focused at 0.79 m from the exit of the flume, near the middle of the erodible bed. The recording catches the beginning of the flow and continues for a maximum length of 5.45 s per experiment, generating 1000 frames per second (fps). We focus and

position the camera at the beginning of each experiment so that it captures the full depth of each flow throughout this ~ 5.5 s and approximately 6.0 cm wide.

The force sensor (Interface: Model SMT S-Type); diameter, $d = 1.27$ cm, sampling frequency, $f_s = 200$ Hz) is located at the base of the erodible bed at 0.93 m from the downstream end of the flume and monitors the evolution of the total normal stress as it evolves during each experiment. The 4 pore fluid pressure sensors (Keller Inc., model PAA-9-FLY; $f_s = 10,000/\text{sec}$) monitor the basal interstitial fluid pressures at 3 locations on the erodible bed and 1 location on the non-erodible bed, as listed in **Table 2-3**. Prior to releasing the supply (flow) we use a computer to activate all four sensors and monitor the details for a total time of 20 s, effectively recording these dynamics measuring through the duration of flow. To guarantee that only the fluid pressure (e.g. no particle contact forces) were applied to the sensor, two stiff mesh layers were enclosed within a metal top (**Figure 2-4**) on top of a membrane that adjusted based on strictly fluid pressure.

We note that the readings of the pore pressure sensors are extremely sensitive to surrounding conditions. The readings are relative to those at the beginning at each experiment and needed to be calibrated daily. To overcome this issue, before each experiment, we calibrate the pore pressure sensors using several incremental volumes of water in a sealed column above each sensor. To do so, we use a known height of a fluid applied vertically above the sensor and multiplied by the density of water to calibrate the specific measurements each day.

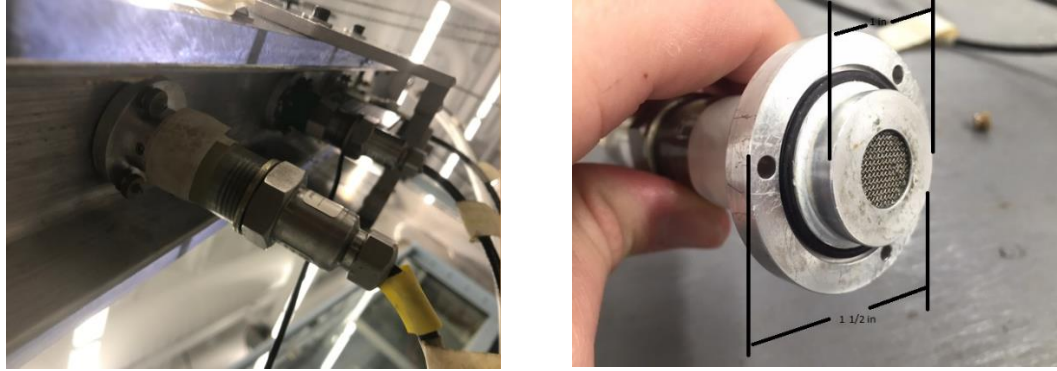


Figure 2-4. (Left) Image of Pore pressure sensors applied to the bottom of the experimental apparatus. (Right) Image of the sensor off of the flume. See *Kaitma et al.* [2016] for more information on these pore pressure sensors.

We measured the mass in the supply, mass in the erodible bed, and mass out of the flume after an experiment via a digital scale with 0.05 g uncertainty. The flume was adjusted to the desired angle monitored by a battery-powered digital level with an accuracy of ± 0.2 degrees. During dry experiments (no fluid in erodible bed or supply) we track the humidity and ensure all particles were anti-static treated, yet for the majority of the flows described in this thesis, the particles were saturated, so these effects were not relevant.

Table 2-3. Instrumentation distances. Note distance, (x) is measured up-flume from the exit ($x=0$).

Instrument	Sensor 1	Sensor 2	Sensor 3	Sensor 4	Force Sensor	High-speed camera
x [m]	1.49	1.03	0.78	0.63	0.84	0.70

2.2 Procedure

During each experimental run we followed a meticulous procedure to maximize reproducibility of the experiment. First we check the flume to make sure it is clean and free of unwanted debris (e.g., dust, particles, fluid). Next, we weigh the supply and bed mass to use in the experiment. For each experiment we fill the erodible bed cavity to the

same level as the bottom of the rigid bed and use the same beads in the supply. Then we carefully level the surface of the erodible bed, so no pre-experimental ripples or bumps are present while making sure to not compact the beads. Once the level of particles is flat enough, we raise the apparatus to the proper angle and begin pumping fluid into a chamber downstream of the rigid bed. The fluid seeps through a mesh layer and begin permeating the erodible bed.

To calibrate the images acquired by the camera, prior to releasing the particles, we affix a piece of grid paper to the side of the flume, take a snapshot of it, and remove it before the flow is released. Once the erodible bed is saturated, we place the supply behind the gate and release it; this is a much more time sensitive step. In rapid succession, we: activate the Canon camera; we initialize the force and pore pressure sensors; we tap the sidewall of the flume (to be explained later); we input the fluid in the supply; we release the supply, and we activate the high speed camera. At least three people are needed to perform these steps within 10 seconds of sensor activation.

During the experiments, the beads first careen down flume over the rigid portion and begin bouncing atop the erodible bed beads. As the granular-dominated front of the flow transforms into a semi-continuous flow, stationary particles that were initially in the bed begin to move, their intensity depending upon the conditions of the flow. Finally, the moving particulate and fluid exit the experimental apparatus. We weigh and record the mass out of the system after each experiment, but do not keep records of the fluid weight out of the flume. We track the dynamics via high speed camera, pore fluid pressure sensors, and force sensor as described previously and presented in more details in Section 2.4. Finally, we take a snapshot of the final form of the erodible bed with the high speed camera.

2.3 Experimental Conditions

When completing the experiments within this thesis, we chose two sets of experimental conditions to determine specific relationships between interstitial fluid viscosity and debris flow dynamics. We chose one set of experimental conditions to determine the relationship between net entrainment and inclination angle to determine how the neutral angle (the angle at which the net mass out of the system is zero) depended on interstitial fluid viscosity. We used this to identify relatively constant run conditions from one experiment to the next for the second set of experiments. Specifically, we studied how the entrainment dynamics varied with interstitial fluid viscosity when the system was inclined at or near the neutral angle.

For all experiments, the boundary conditions that were identical for the majority of the experiments are as follows:

- Initial Position – IP 1.5
- Beads – 2 mm ZrSi particles (**Table 2-1**)
- Flume – Same as dimensions defined in diagram (**Figure 2-1**)

2.3.1 Neutral Angle

The effect of the neutral angle on entrainment dynamics has been investigated in *Tai and Kuo* [2008] and tracked on this flume in *Moberly* [2015]. However, the effect of viscosity on the neutral angle has yet to be systematically investigated. In this thesis, we completed neutral angle experiments for 4 different viscosities (**Table 2-4**).

Table 2-4. Summary of neutral angle experiments

Experiment*	# of Trials	Target Viscosity (cP)	Actual Viscosity (cP)	Angle (°)
E1_15_1_N3	3	1	1	15
E1_16_1_N3	3	1	1	16
E1_17_1_N3	3	1	1	17
E1_15_5_N3	3	5	5	15
E1_16_5_N3	3	5	5	16
E1_16.5_5_N3	3	5	5	16.5
E1_17_5_N3	3	5	5	17
E1_18_5_N3	3	5	5	18
E1_16_25_N3	3	25	27.5	16
E1_17_25_N3	3	25	27.5	17
E1_18_25_N3	3	25	27.5	18
E1_16_62_N3	3	50	62	16
E1_17_62_N3	3	50	62	17
E1_18_62_N3	3	50	62	18

*Experiment name formatted as follows: E#_θ_ μ_{fl}_I#, where E# refers to the “experiment group”, μ_{fl} is the fluid viscosity and I# indicated the number of duplicate experiments performed under those conditions.

2.3.2 Viscosity Dependence

To test the effect of altering viscosity on entrainment dynamics, we systematically altered the viscosity of the interstitial fluid μ_{fl} , by changing the concentration of glycerin to water content (see **Table 2-2**) for specific percentages of glycerin-water).

Table 2-5. Experimental Conditions for viscosity dependence experiments

Experiment*	# of trials	Angle of Inclination (°)	μ_{fl} target (cP)	μ_{fl} measured (cP)
E2_1_N1	1	16.5	1	1
E2_5_N1	1	16.5	5	5
E2_12_N2	2	16.5	12	12
E2_19_N2	2	16.5	19	20
E2_25_N2	2	16.5	25	25
E2_50_N1	1	16.5	50	50

*Experiment name formatted as follows: E#_ μ_{fl} _N#, where E# refers to the “experiment group”, μ_{fl} is the fluid viscosity and I# indicated the number of duplicate experiments performed under those conditions

2.4 Data Analysis

This section includes descriptions of the procedure we follow to analyze data acquired over the course of each experiment. Video analysis includes tracking the particles and finding spatial and temporal parameters related to these quantities. Sensor analysis includes the steps of raw data from the sensor to make data comparison possible. After the experiment is completed, macro and micro experimental results are analyzed. The primary macro result is the total mass out, m_o , of each experiment. No records of volume of fluid after flow are kept.

2.4.1 Video Analysis

We performed the following steps to process the digital images from the Photron camera:

- (1) Particle location
- (2) Particle tracking

- (3) Velocity and density field analysis
- (4) Height analysis
- (5) Entrainment analysis
- (6) Average stress analysis
- (7) Interfacial granular temperature analysis

Particle Location. In each picture acquired using the high resolution Photron camera, each particle is located according to brightness using a MATLAB program developed by researchers in the Georgetown Physics department [Blair and Dufresne, 2008]. We use the brightest local maximum to identify the center of the particle, and we assign a diameter to each local maximum (**Figure 2-5**). Each particle is given an ID number to identify it from frame to frame.

Particle Tracking. We then use a distance minimization algorithm we developed to track the location of each particle from one image to the next. If the particle exits the image, the ID number also exits the analysis; alternatively, if a particle enters the image, it is assigned a new ID number. We then use the particle displacements for further analysis (**Figure 2-5**).

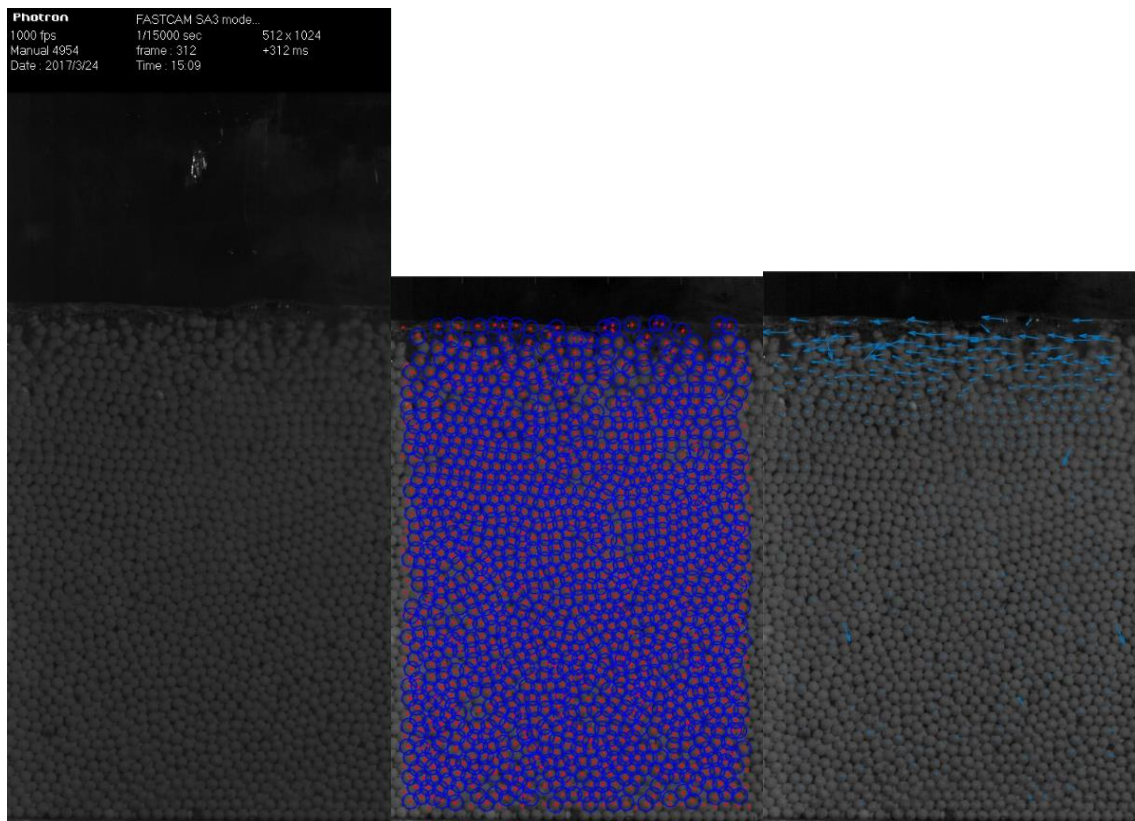


Figure 2-5. Analysis via brightness is completed on the image from high speed camera.

(Left) The raw image from the camera. (Center) The raw image is cropped and the particles are selected by a given brightness threshold. The red spots are the brightest maxima within a radius approximated by the blue circles. (Right) The particles advance along the direction of arrow and their velocities are scaled by size of the arrow. Flow is from right to left, and this example is from E2_12_T1.

Velocity and density field. We use the positions and displacements of each particle to derive entrainment behavior and other dynamics associated with the experimental debris flows. To do so, we first derive the data from each image into “horizontal” bins (i.e. bins parallel to the base of the flume) covering the extent of the image from top to bottom. The thickness of each bin is uniform throughout each image, and in these experiments is 21 bins/d (where $d=0.095$ mm, the average diameter of the beads we used). We time average the position data over the time step we determine best represents the data while minimizing noise: Δt (0.05 seconds).

We calculate an average volume fraction for each bin according to the procedure summarized in *Hill et al.* [2003], for $\langle f \rangle_{B_y}$

$$f(y) \equiv \langle f \rangle_{B_y} = \sum_i \sum_b V_i^b(B_y) / N_t V \quad (2.1)$$

and an average velocity for each bin by considering every particle within a bin $\langle u \rangle_{B_y}$, even if it is only partially included, again similar to *Hill et al.* [2003].

$$u(y) \equiv \langle u \rangle_{B_y} = \frac{\sum_{i=1}^{N_t} \sum_{b=1}^{N_{pi}} \frac{V_i^b(B_y) \times u_i^b}{\sum_{i=1}^{N_t} \sum_{b=1}^{N_{pi}} V_i^b(B_y)}}{\sum_{i=1}^{N_t} \sum_{b=1}^{N_{pi}} V_i^b(B_y)} \quad (2.2)$$

In these equations, $u(y)$ is the horizontal velocity (dependent on y); B_y refers to a horizontal bin, centered at y , of thickness Δy and volume V ; N_t is the number of images considered in the average (i.e., number of time steps; for these calculations 50 images per time step); N_{pi} is the number of particles in image i , and N_t is the number of images (i.e., time steps); u_i^b is the instantaneous horizontal velocity of the center of bead b in image i ; and $V_i^b(B_y)$ is the volume of the section of particle b which falls within bin B_y in image i .

Heights. To simplify the description of the flow, we denote three regions of the granular materials in the images we analyze (**Figure 1(b)-(d)**); We use $f(y)$ and $u(y)$ (because they are dependent on vertical position) to define qualitatively and quantitatively these three regions: (1) the stationary region, where the solid fraction is high and the velocities and temperatures are low; (2) the dense flow region, where the solid fraction is high, and the velocities and velocity fluctuations are moderate to high, and (3) the sparse flow region, where the solid fraction is low and the velocities and velocity fluctuations are both moderate to high. We define a critical velocity u_{crit} (detailed below) to define a boundary between stationary and dense flow regions and a critical solid fraction f_{crit_DFL} (also detailed below) to define a boundary between sparse and dense flow (see **Figure 2-6**).

The region of dense flow is characterized by a monotonically increasing average downstream velocity with increasing height from the bottom of this region. As *Komatsu*

et al. [2001] showed for erodible piles, we find that the mean velocity is finite at all depths. Specifically, for deep layers, the velocity profile decays exponentially with depth and has a characteristic decay length equal to the particle size [*Hill et al.* 2003; *Gioga et al.*, 2006]; this seems reasonable by visual inspection and we use it to identify a critical transition in our flow (see **Figure 2-6**). To identify an entrainment height that is quantifiable and reproducible, we choose a critical value of the average downstream velocity as one that falls within the creeping region; here we choose $u_{crit} = 0.01m/s$. Then, for each averaged profile j , (averaged over the data from $N_t = 50$ images) we fit the velocity data $u_j(y)$ in a small region near $u_j(y) = 0.01m/s$ using an exponential function that can be expressed according to:

$$y_{botfit,j}(u_j) = m_j \ln[u_j(y)] + b_j \quad (2.3)$$

Here, m_j and b_j are fitting coefficients determined from a linearized least square fit of this region of the velocity profile at interval j , at each time step. Then, we associate the boundary between stationary and dense flow regions as $y_{crit,j} = m_j \ln[0.01] + b_j$ and identify the entrainment height discussed in the thesis $H_{m,j} \equiv y_{crit,j}$ at each time interval over which the velocity profile is calculated (e.g., **Figure 2-6**). In **Figure 2-6** we see that between $-8 < \ln\langle u \rangle < -2$ the regression accurately predicts the velocity. More importantly, this fit finds a reproducible value for the base of the dense flow true to the actual velocity in this region.

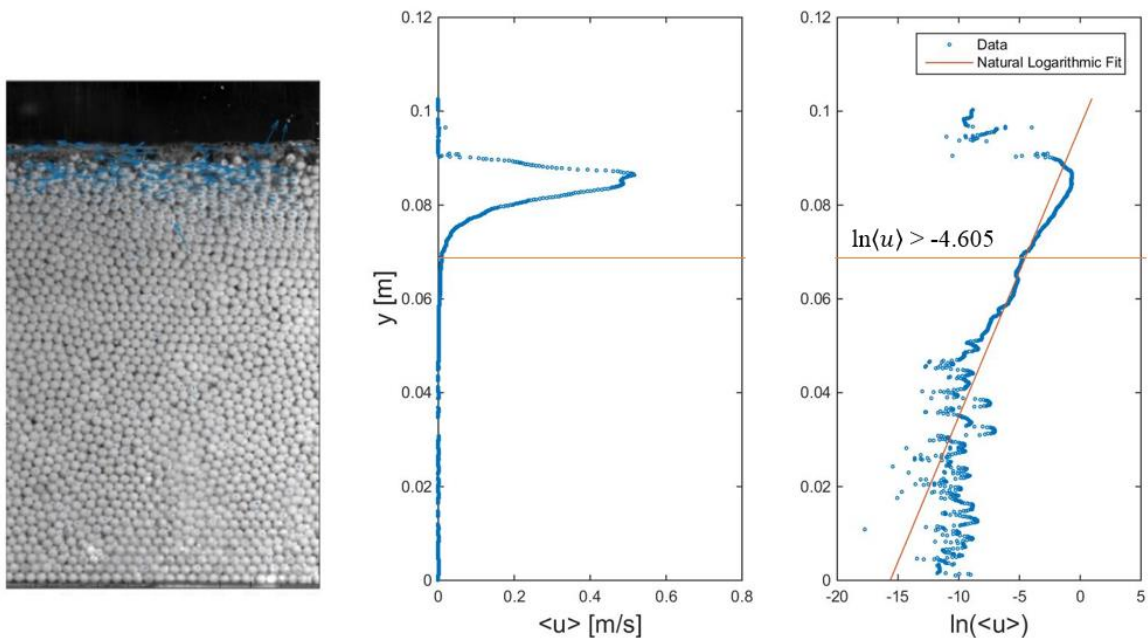


Figure 2-6. Tracking the particles yields a horizontal velocity profile (u). (Left) Plot of instantaneous velocities at frame 1000 (1 s); flow is from right to left (Center) The horizontal velocity is averaged and each point represents an average from each bin. (Right) The natural log of the velocity profile, the vertical line, u_{crit} , is set at $\ln(0.01) = -4.605$. The slope at the intersection of the plotted points and the u_{crit} line is defined by least squares regression. The entrainment height (H) is measured from the bottom of the bed to the interface between the flowing layer and the stationary layer (orange line). The movement of this boundary is a measure of the instantaneous erosion rate. This example is from E2_12_T1.

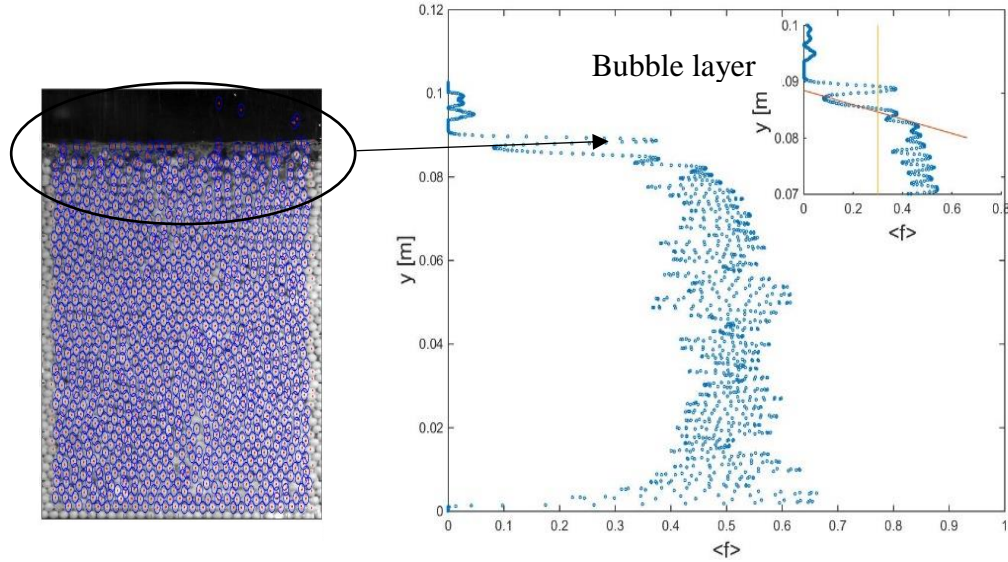


Figure 2-7. Density analysis described in the text. (Left) image of the particles with a high local brightness (red spots) and an approximate radius (blue circle). (Right) Example Volume Fraction profile at $t = 1$ s. In the inset is the linear fit (orange) based on 21 points surrounding the f_{crit} value (yellow line). Note the bubbles on the top of the left image.

To create a quantifiable, reproducible definition for the top of the dense flowing layer, we note that, with increasing distance from the bottom of the flow, the velocity remains high even in the top region as the solid fraction drops continuously (Compare **Figure 2-8** with **Figure 2-9**). We use the calculated solid fraction profile to define the interface between the sparse and the dense flow. Somewhat arbitrarily, we choose the section immediately surrounding the point at which the solid fraction first increases above the value of $f_{crit_DFL} = 0.3$ and we fit the data in a small interval surrounding this point using a linearized least squares fit line:

$$y_{topfit,j}(f_i) = A_j f_j(y) + B_j \quad (2-4)$$

Here, A_j and B_j are fitting coefficients determined from a linear least squares fit of this region of the velocity profile at time interval j , at each time interval (**Figure 2-7**). Then, we associate the boundary between stationary and dense flow regions as $y_{t,j} = 0.3A_j +$

B_j . We note that 0.3 was somewhat arbitrarily chosen as the transitional value for the critical solid fraction. We decided on this by comparing the results from using a few different values of y_{crit} (**Figure 2-8**). If f_{crit_DFL} was set as a higher value, the top of the dense flowing layer would decrease; additionally, it will become less stable because the volume fraction profile is unstable itself, fluctuating from image to image as particles dilate and contract (**Figure 2-7**). The results are qualitatively similar with different levels of noise and the best compromise where the results were minimally sensitive to the choice of y_{crit} was for $f_{crit} = 0.3$. Note with $y_{t,j}$ from **Equation 1.5** and H from **Equation 1.4**, we can define a thickness of the dense flowing layer at time interval j according to $h_j = y_{t,j} - H_{m,j}$.

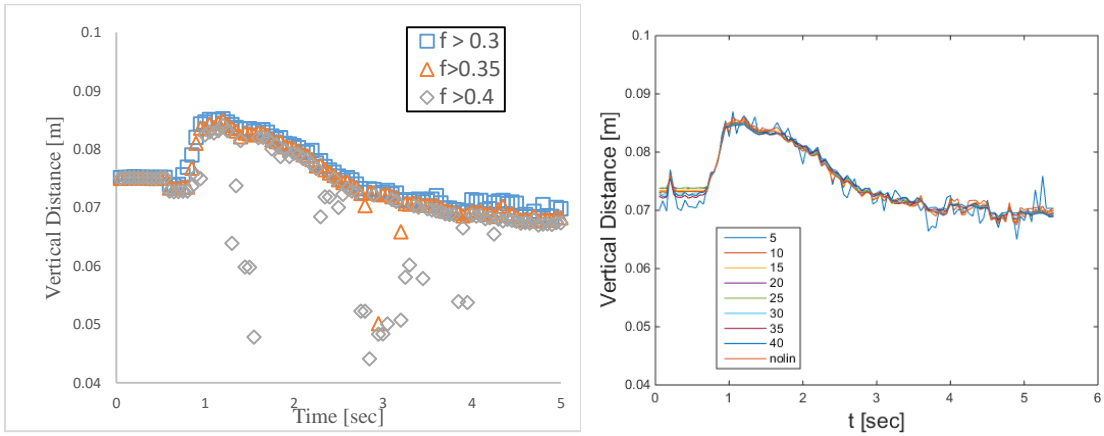


Figure 2-8. (Left) Plots illustrating the results from the different ways we define the top of the dense flowing layer in the text. The minimum volume fraction, f_{crit_DFL} , was altered and because of this, the top of the defined dense flowing layer would change. (Right) The top of the dense flowing layer is tested from 5 to 40 points on either side of f_{crit_DFL} . In addition a calculation using no linear fit (salmon) is displayed.

To define a top of the sparse flowing layer, we need an estimate for where there is both minimal particle concentration and no fluid. To do this, we made use of the fact that for these systems, a fluid/bubble layer formed on the top of the flow that delineated the top of the fluid layer. This was captured in the particle location algorithm as “false

particles”. We can see the effect of this in the calculated density profile as a bump at the top of the plot in **Figure 2-7**. We used the data below this region to identify a region appropriate for approximating the top of this sparse flow. Still, this was a rather noisy start to a solution that might otherwise be similar to the fit we used for the top of the dense flow.

Once we effectively eliminated the bubble region from the calculation, we tried two things with the remaining data:

1. First, we use a similar method to that we described above for the top of the dense flowing layer. Specifically, we found a suitable critical value of f for the dense to sparse transition ($f \sim 0.05$) and performed a linear least squares fit to data surrounding that point. The results for different segments of the data surrounding this point are shown in **Figure 2-9a**, compare with **Figure 2-9b**).
2. The second method is simpler in that we identify exactly the point at which f first descends to a critical value, chosen through trial and error based on minimizing the noise.

When using method 1, the results could be in theory robust; however, this strategy typically includes pseudo-particles from the top of the layer (thus rendering it strictly incorrect). Results from method 2 using the critical value of $f_{crit_top} = 0.1$ yield what appears to be a reasonable result, qualitatively consistent with the results from method 1, yet significantly smoother. So we used this method for identifying the top of the flow layer. The results from both methods are illustrated for one case in **Figure 2-9**. We note they both indicate the thickness of this top sparse flowing layer is approximately 2 bead diameters.

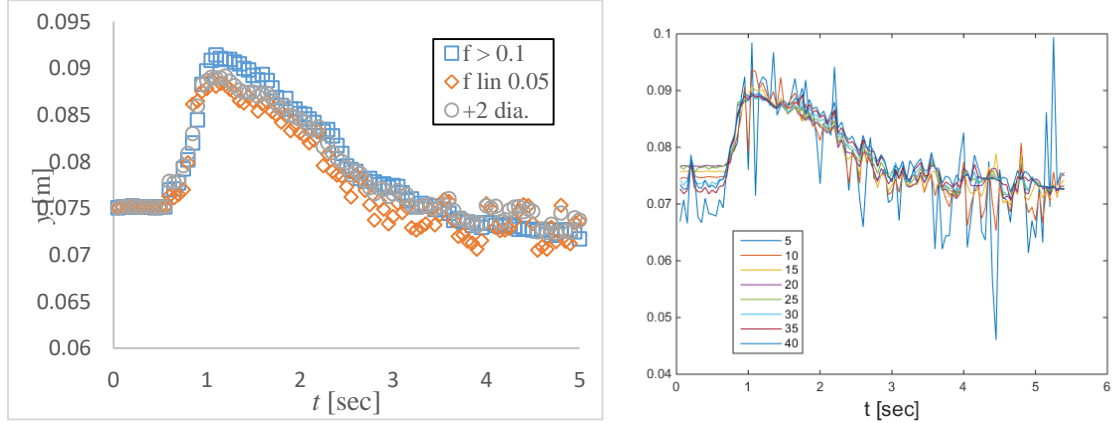


Figure 2-9. (Left) The top of the fluid layer ($y_{f_crit_top}$) is found in different ways as described previously. $f > 0.1$ (blue square) refers to the method of one setting a definite value $f_{crit} = 0.1$. Orange diamonds refers to the method of linear interpolation similar to **Equation 2-6**. Grey circles refer to the pseudo-method of addition of 2 bead diameters for reference. (Right) The top of the flow is tested 5 to 40 points on either side where f_{crit_top} is equal to 0.1.

When analyzing the data of the top of the dense flowing layer, we noticed that the top of the flow contained a fluid layer not previously encountered in dry experiments [Moberly, 2015]. The difficulty in measuring this new layer was evident because of the bright spots that appear in bubbles above this fluid layer. To counteract this effect, we compare the effectiveness of different methods

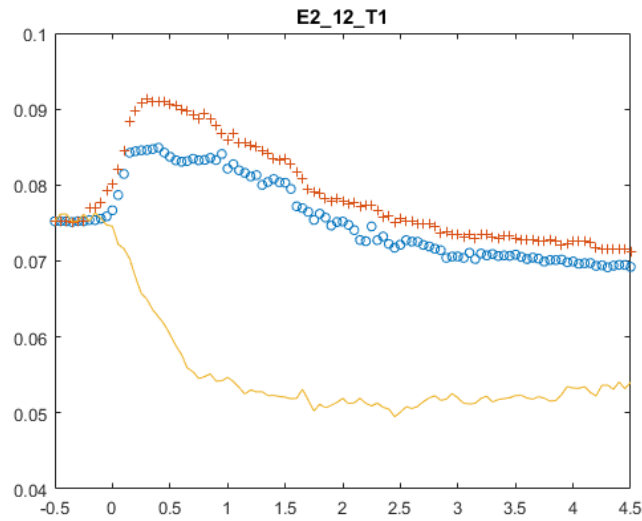


Figure 2-10: The three different regimes we consider in these experiments are above. (+) is the top of the fluid layer defined by f_{crit_top} , (circles) is the top of the dense flowing layer defined by f_{crit} , and solid line is the entrainment height, H , defined by a linear fit around u_{crit} . This example is from E2_12_T1.

All interfaces/heights for a particular experiment are shown in **Figure 2-10**. We note that we associate each with a physically significant quantity. The top of the fluid layer is the hydrograph of the top of the flow; the top of the dense flowing layer is a dense hydrograph, and the yellow line tracks the depth at which particulate is moving.

Entrainment and entrainment rate discussion. The corresponding y value from u_{crit} is what we will call the entrainment height, H , (referred to previously as $H_{m,j}$) (**Figure 2-11**).

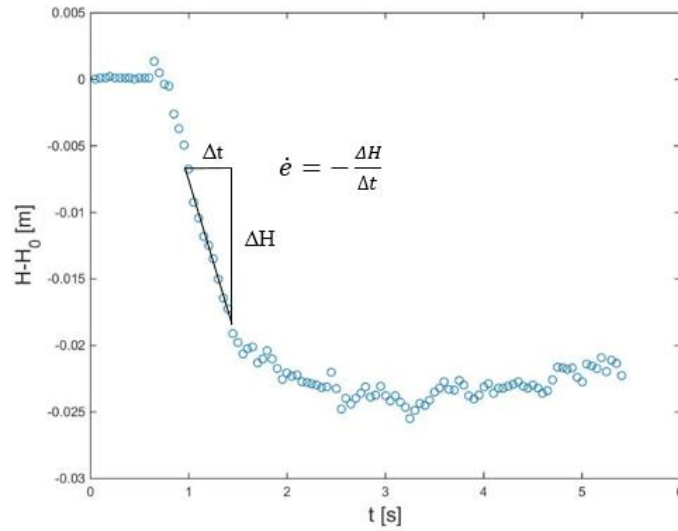


Figure 2-11. Zeroed entrainment height, $H-H_0$, where H_0 is the initial depth, vs time for E2_12_T1. The entrainment rate is the average slope over 9 points (4 before and 4 after each data point).

We track this value throughout each experiment and find a range of time steps and compute a slope, yielding the entrainment rate, \dot{e} .

$$\dot{e} = -\frac{\Delta H}{\Delta t} \quad (2.5)$$

The entrainment rate profile depends upon how many frames are chosen to average through; with less time steps, the entrainment rate can become more precise but also contain more noise, while the opposite is true for a wider time average. We chose a middle ground at 4 points before and 4 after, 9 total points used for average (**Figure 2-12**). Notice that the peak entrainment rate decreases when more points are averaged.

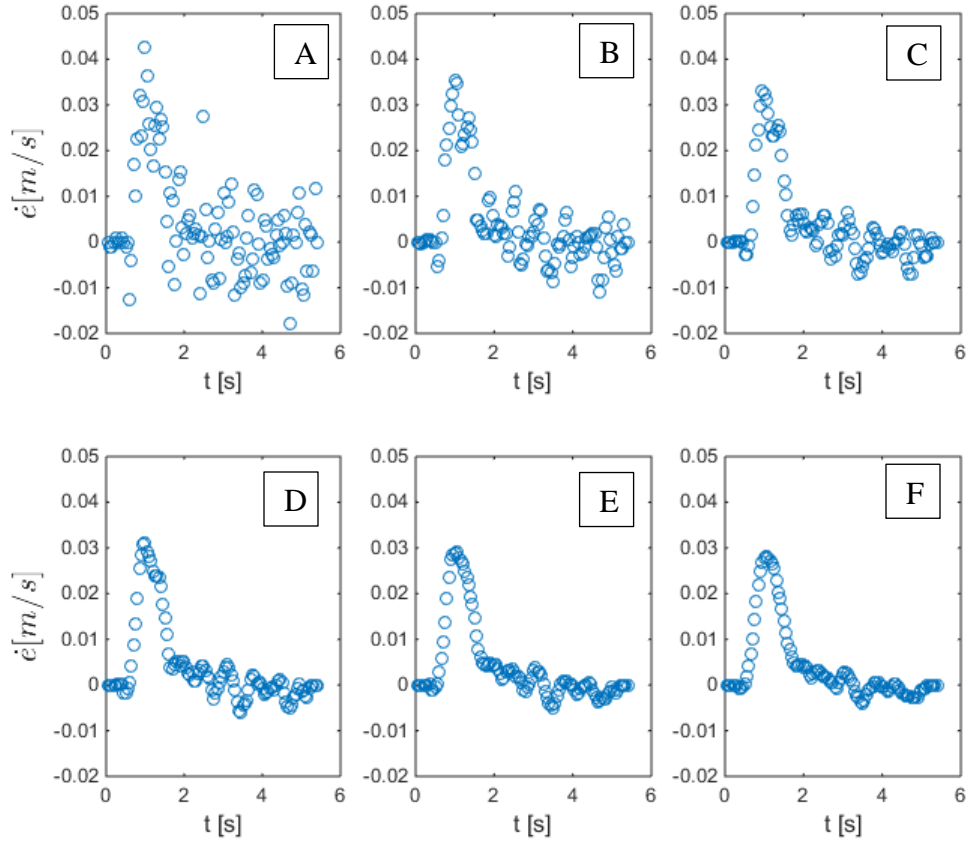


Figure 2-12. Methods of calculating the entrainment rate depending on the slope over (A) 3, (B) 5, (C) 7, (D) 9, (E) 11, and (F) 13 points. For each case, the middle point of the linearization has an equal number of averaged points on either side (e.g. 3 has 1 point on either side to compute the slope). For the remainder of these tests (D) is used. From E2_12_T1.

Average stress analysis. One of the major goals of these experiments is to determine the driver behind entrainment. There are multiple different potential entrainment “drivers”: shear stress, pore fluid pressure, granular temperature, or others. To figure whether one of our datasets is driven by one of these dynamics, we attempt to find a correlation between entrainment rate and a physical mechanism. With a definition of the dense flowing layer, h_{DFL} , and top of the fluid layer, h_{top} , we define further parameters of interest such as the granular temperature T and shear stress, τ .

Shear stress is based off of the top of the flowing layer. The shear stress, τ , is calculated as

$$\tau(y) = (\rho_s \sum_H^{top} \langle f \rangle_{Bi} + \rho_f (1 - \sum_H^{top} \langle f \rangle_{Bi})) g \sin \theta \quad (2.6)$$

where ρ_s and ρ_f [kg/m³] are the density of both the fluid and particle, respectively, θ [°] is the angle of bed incline, $H = H/\Delta z$ and $y_{top} = (H + h + h_{top})/\Delta z$, ($\Delta z = 1/21$ [bins] and is the height of a bin) and g [m/s²] is the acceleration due to gravity. Including the dense flowing layer in the calculation for shear stress has been previously used for these experiments [Moberly, 2015; Longjas et al., 2017]. However, with the addition of fluid into these experiments, the new layer of fluid is likely affecting the shear stress and progression of the flow and is compared in the following (**Figure 2-13**).

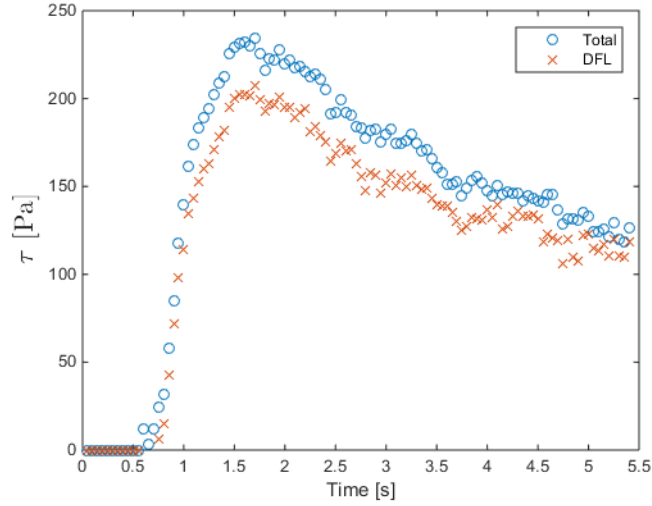


Figure 2-13. Plot of shear stress (τ) through time. Two different methods are considered: The dense flowing layer is the height, h_{DFL} (x) or the entire flow is considered, $h_{DFL} + h_{top}$ (circles).

Interfacial granular temperature analysis. With an average velocity, we calculate the velocity fluctuations (horizontal, u' and vertical, v') from each particle's instantaneous velocity within a bin. We find the average horizontal and vertical fluctuations, $\overline{u'u'}$ and $\overline{v'v'}$ respectively, of each bin from the average u' and v' across each bin in the dense flowing layer. In addition to the granular temperature, a comparison of the Reynold's

Shear Stress is found by determining average shear stress fluctuations, $\overline{u'v'}$. These fluctuations can be further applied into a combination of the average horizontal and vertical velocity fluctuation through the granular temperature, $\langle T \rangle$, given as:

$$\langle T \rangle_{BZ} = \sum_i \sum_b V_i^b \left((v_i^b - \bar{v}_{BZ})^2 + (u_i^b - \bar{u}_{BZ})^2 \right) / N_t V \quad (2.7)$$

And where the Reynold's Shear Stress, $\langle \tau_R \rangle$, is defined as:

$$\langle \tau_R \rangle_{BZ} = \sum_i \sum_b V_i^b \left((v_i^b - \bar{v}_{BZ})(u_i^b - \bar{u}_{BZ}) \right) / N_t V$$

Where the average horizontal and vertical velocity in bin, BZ , is \bar{u}_{BZ} and \bar{v}_{BZ} , respectively. In **Figure 2-14**, we calculate the temperature and Reynold's shear stress 2 bead diameters away from the entrainment height, H . This way we can more closely analyze the interface between moving and non-moving particles while not including too much interaction from particles that are too far away to have any affect.

The Granular Temperature and Reynold's Shear Stress is averaged similarly to the entrainment rate, yielding \bar{T} and $\bar{\tau}_R$, respectively; the previous four and following four data points are averaged against each other and set at the middle data point.

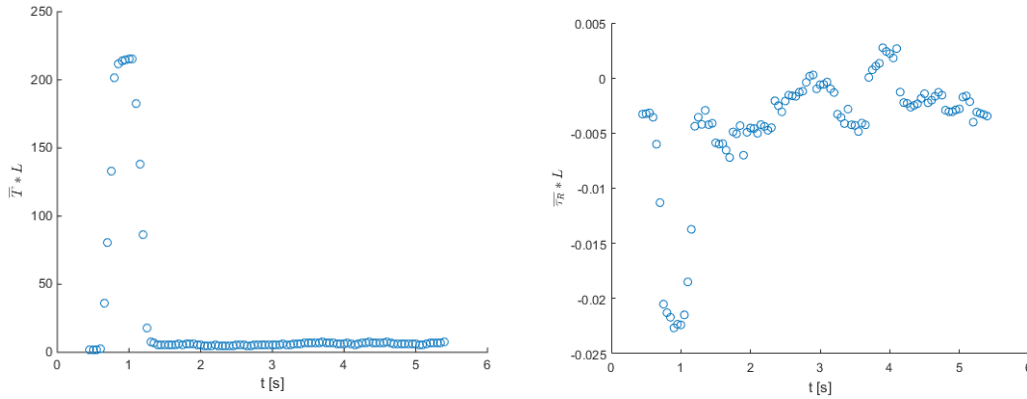


Figure 2-14. (Left) Plotting \bar{T} through time. The peak is a plateau because there is only one value that is much larger than the others. The granular temperature increases first, then stabilizes (due to averaging scheme), then decreases from its maximum to a near zero \bar{T} within 0.5 s. From E2_12_T1. (Right) Plotting $\bar{\tau}_R$ through time. The absolute value of the peak here occurs at the same time.

Dense and sparse discharge rates: unifying the start times. With profiles for $\langle u \rangle$ and $\langle f \rangle$, the flow rate is calculated (**Equation 2.8**), and with that, we can define a new shifted time to align our data by a certain criterion. We found that the best way to match up different experiments was to use the point when the flow enters the sight of the high-speed camera.

$$Q = \sum_{y=1}^{y=H+h_{DFL}+h_{top}} \langle f \rangle * \langle u \rangle \quad (2.8)$$

Furthermore, the point at which the flow is of a density great enough to be a developed, dense flow was used for shifting. We find where the flow becomes more than 20% dense (20% of bins that are moving are $\bar{f} > 0.3$) and define this point as t_s or $t = 0$. This shifting will allow temporal alignment.

2.4.2 Pore fluid pressure analysis

Pressure sensor data. The next step is to compare the data we gather from the pore pressure sensor against the data from our high-speed camera. The complete analysis of pore pressure data includes three different phases. First the recorded data is converted from volts to pascal within a visual basic program, generating raw data (**Figure 2-15**). Next, the raw data is shifted by the pore pressure of the sensor just before the flow arrives. This is called the zeroed pore pressure (**Figure 2-16**). Because the pore pressure from the pore pressure sensor mentioned above includes noise, a 50-point moving average was applied to the pore pressure data for an effective sampling rate of 200 Hz (**Figure 2-17**).

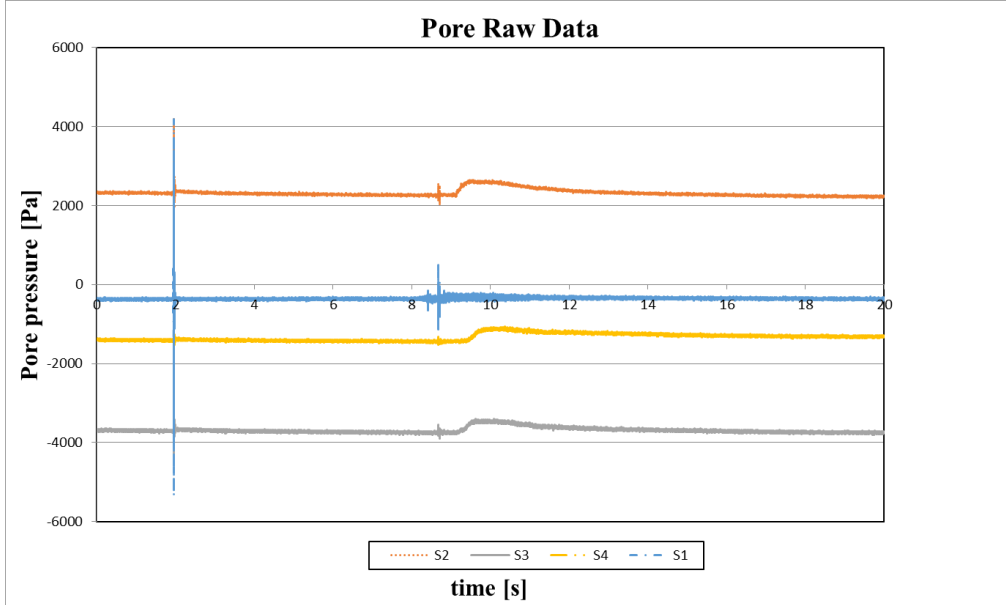


Figure 2-15. Pore Pressure Raw Data from sensors 1-4. There is an initial pressure offset as the sensors are not aligned by initial voltage reading.

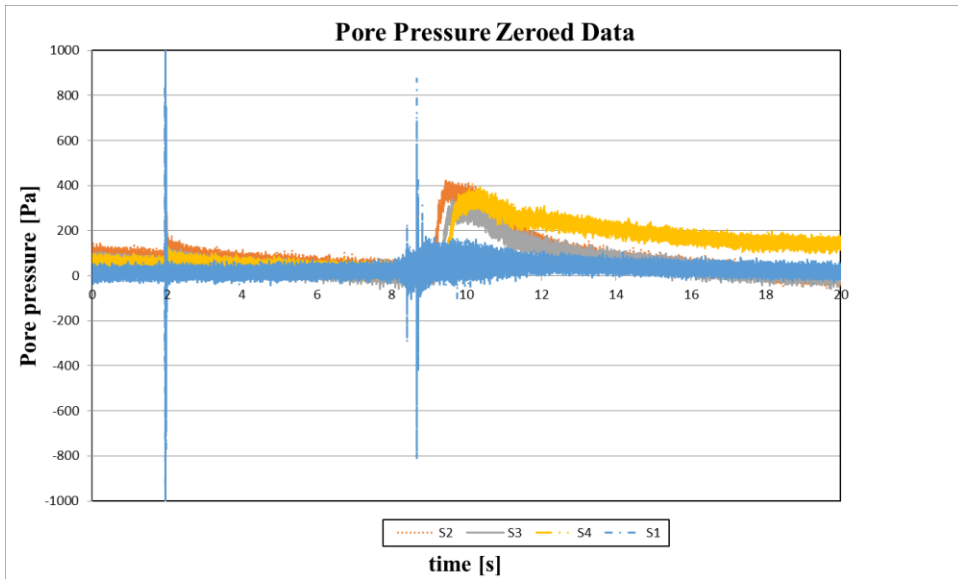


Figure 2-16. Zeroed Pore Pressure Data. The data was shifted by subtracting the value of pore pressure before flow arrival.

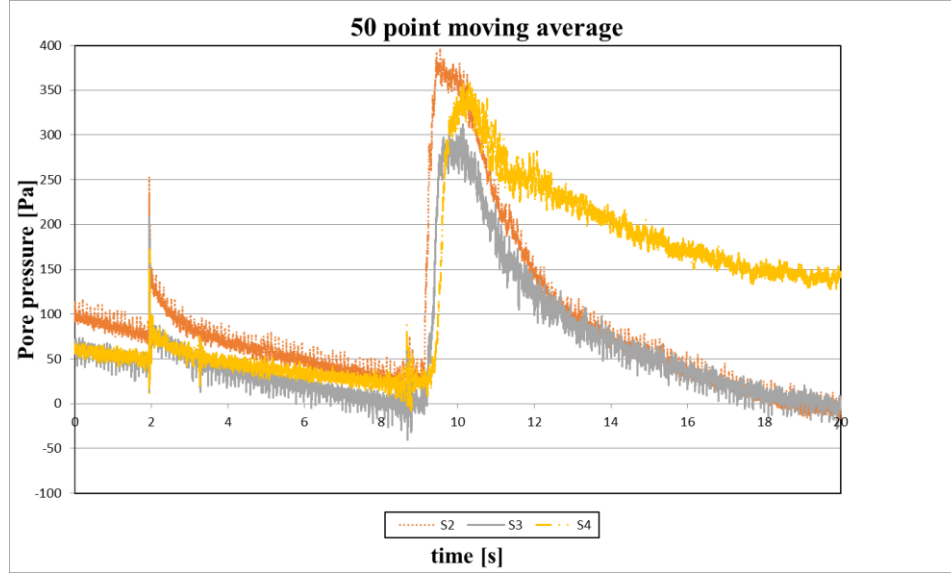


Figure 2-17. 50-point moving average applied to the pore pressure data. Note that Sensor 1 (S1) is not included because we are focused on the dynamics of pore pressure in the erodible bed (**Figure 2-1**). This example is from E2_12_T1.

The pore pressure data output reads the time that the trigger for the sensor is activated and when the video has begun recording; because the video has 500 frames before the trigger input for recording, the pore pressure time is further shifted. In addition, the pore pressure sensors would be matched by initial pore pressure in the bed above the sensor. To do this the average of the first 3 measurements of the top of the flow, h_{avg} , is converted into pascal ($P = \rho_f g h_{avg} \cos\theta$) and added to the zeroed pore pressure measurement. We then select every 500th measurement of pore fluid pressure, beginning at the shifted position, to match the two datasets together.

Image data and model pore fluid pressures. To generate initial comparisons of the pore fluid pressure from the high-speed camera, we say that the total height of the bed was completely saturated, including the dense flowing layer, and in addition, say that the top of the fluid layer was contributing to the total pore fluid pressure, P ,

$$P_{DFL_f} = \rho_f g h_{DFL} \cos\theta \quad (2.9a)$$

$$P_{top_f} = \rho_f g h_{top} \cos\theta \quad (2.9b)$$

$$P_{st_f} = \rho_f g H \cos\theta \quad (2.9c)$$

$$P_{calc} = P_{top_f} + P_{DFL_f} + P_{st_f} \quad (2.9d)$$

Where P_{calc} [Pa] is the total pore fluid pressure calculated from the video analysis, P_{top_f} and P_{DFL_f} are the pore pressure contributions from the top of the flow and dense flowing layer, respectively, and P_{st_f} is the pore fluid pressure from the stationary layer.

2.5 Scaling and Similitude

2.5.1 Rationale for Dimensional Analysis

Traditionally, scaling and similitude has been used to compare the experimental to a natural effect. For debris flows, there are limitations to scaling down the natural disaster. Replicas of the initial topography, size of particles, and movement of the flow as a whole cannot realistically be accomplished within a laboratory setting. Most importantly, debris flows in nature are too dangerous to get close enough to accurately and precisely measure their true dynamics. More so, if a technique is developed that allows for analysis, affecting the progress of the flow as it moves must always be a concern. However, while limited in complexity, systematic experimental results do yield findings on individual variables in a safe setting. Once an experiment is designed, it is necessary to confirm if it is accurately predicting the effects of debris flow, and if it is not, to what magnitude is a certain parameter differing from nature. The basis behind this process, also called dimensional analysis, is to first reduce all variables to their base quantities (relevant here are length, mass, and time). This process can be intensive and is formalized through the Buckingham π theorem (Buckingham, 1914).

As mentioned, similitude has commonly been used to directly model a phenomenon in nature; however, within this thesis, we are not trying to do this. We are using a controlled experiment to find the effect of interstitial fluid viscosity on entrainment on an erodible

bed of mono-sized particles. In other words, we are systematically varying a single variable to determine its effect on a particular dynamic.

2.5.2 Debris Flow Variables

Here important variables are discussed to complete the scaling and similitude; they are divided into three different categories: geometric, kinematic, and material property. For geometric properties: L , is the length of the flow, from the head of the flow to the end of the tail, H_{\max} is the maximum height of the flow throughout the flow, d is the averaged particle diameter, and θ is the angle of inclination of the flow. For kinematic variables: g is the acceleration due to gravity, η is the mean sediment porosity, $\dot{\gamma}$ is the shear rate, and D is the hydraulic diffusivity (a constant based off other specified functions [*Savage and Iverson, 2003*]). Finally, the properties of materials are as follows: μ_f is the interstitial fluid viscosity, ρ_s is the solid grain density, ρ is the bulk density, ρ_f is the interstitial fluid density, and ρ_0 is a normal reference density at static equilibrium (based off *Iverson et al., [2010]* a ratio of $\rho_0 = \rho/1.07$ will be utilized). **Table 2-6** lists the dimensional parameters from *Iverson et al. [2010]* (column 2-4) with comparison to our flume (column 5 and 6).

Table 2-6. Dimensional and naturally dimensionless parameters measured from our flume in the U of M Fluid Mechanics Lab (CE). Note that D and ϕ were assumed to be similar to *Iverson et al.* [2010].

Dimensional Parameters	Tabletop*	USGS Flume*	Nature*	CE H ₂ O	CE 50 cP
d (m)	0.01	0.01	0.01	0.002	0.002
L (m)	N/A	95	10 ³	3	3
H_{max} (m)	0.03	0.3	3	0.02	0.02
ρ_s (kg/m³)	2700	2700	2700	4100	4100
ρ_f (kg/m³)	1200	1200	1200	1000	1197
μ_f (Pa-s)	0.1	0.1	0.1	0.001	0.05
g (m/s²)	9.81	9.81	9.81	9.81	9.81
$\dot{\gamma}$ (s⁻¹)	N/A	101	33.0	271	271
η ()	0.37	0.37	0.37	0.37	0.37
D (m²/s)	10 ⁻⁵	10 ⁻⁵	10 ⁻⁵	10 ⁻⁵	10 ⁻⁵
ϕ (°)	39	39	39	39	39
θ (°)	31	31	31	16.5	16.5

*Data from *Iverson et al.* [2010].

Furthermore, from Iverson [2010], there are stresses and pressures that have been previously used for similitude. These are used to further generate more equations to match variables. The following dimensionless parameters were utilized for scaling between different size and viscosity flows given in **Table 2-7**: τ [Pa] is the estimated basal shear stress as defined in **Equation 1.6**, σ_{bed} [Pa] is the estimated basal normal stress ($\sigma_{bed} = \rho g H_{max} \cos\theta$), p_{bed} [Pa] is the estimated basal pore fluid pressure ($p_{bed} = \rho_f g h \cos\theta$), and τ_y [Pa] is a yield stress (as in **Equations 1.1** and **1.2**), and σ_{eff} is the effective stress as defined in through **Equation 1.9b**.

Table 2-7. Calculation of stresses utilized in a typical experiment; used in **Table 2-8**.

Stresses and pressures [Pa]	Equation	CE H ₂ O	CE 50 cP
τ_y	(assumed similar to nature)	100	100
p_{bed}	$\rho_f g H_{max} \cos\theta$	200	220
σ_{bed}	$\rho g H_{max} \cos\theta$	400	400
σ_{eff}	$\sigma_{bed} - p_{bed}$	200	220
τ	$[\sigma_{bed} - p_{bed}] \tan\varphi$	500	596

Finally, the comparison of 10 different dimensionless parameters chosen to be similar to *Iverson et al.*, [2010] are calculated in **Table 2-8**. We see that there are 9 dimensional parameters (**Table 2-6**), we have 3 physical variables (length, time, and mass), so from the Buckingham π theorem (1914) we require 6 dimensionless variables. The following variables are used for this analysis, ε is a height-length ratio, R is a bulk density ratio defined as 1.07, R_f is the fluid to reference density ratio, C is a ratio of the shear stress to the maximum shear stress (corresponding to the maximum height) of a well-mixed flow, Y is the ratio of the yield strength to the maximum shear stress (corresponding to the maximum height) of a well-mixed flow, Q is the excess shear stress ratio, N_R is a ratio of the inertial forces to the viscous forces (similar to Reynold's number), N_P is a ratio of the inertial forces to the diffusive force, d/H is a ratio of the diameter of the particles to the height of the flow, S is the ratio of the grain collision stresses to the gravitational shear stresses, and finally, I represents the inertial forces to the forces acted upon the flow.

Table 2-8. Dimensionless parameters calculated based on parameters estimated by *Iverson et al.* [2010] (first 3 columns) and those from our experiments using water and 50 cP glycerin/water mixtures as interstitial fluids in our experiments.

Dimensionless Parameters	Equation	Tabletop*	USGS*	Nature*	UM H ₂ O	UM glycerine
ε	$\varepsilon = \frac{H_{max}}{L}$	0.01	0.01	0.01	0.01	0.01
R	$R = \frac{\rho}{\rho_0}$	1.07	1.07	1.07	1.07	1.07
R_f	$R_f = \frac{\rho_f}{\rho_0}$	0.60	0.60	0.60	0.50	0.60
C	$C = \frac{\tau}{\rho_0 g H_{max}}$	0.5	0.5	0.5	0.36	0.39
Y	$Y = \frac{\tau_y}{\rho_0 g H_{max}}$	0.20	0.02	2.E-03	0.25	0.25
Q	$Q = \frac{\tau}{\tau_y}$	9.15	91.5	915	4.98	5.96
N_R	$N_R = \frac{\rho_0 H_{max} \sqrt{gL}}{\mu_f}$	3E+03	1E+04	3E+06	2E+05	4E+03
N_P	$N_P = \frac{\sqrt{L/g}}{H_{max}^2/D}$	6.E-03	2.E-04	6.E-06	1.E-02	1.E-02
d/H	d/H_{max}	0.3	3E-02	3E-03	0.1	0.1
S	$S = \frac{\rho_s \dot{\gamma}^2 d^2}{\sigma_{eff}}$	10	0.1	1.0E-03	4.6	4.2
I	$I = S^{1/2}$	3.2	0.3	3.2E-02	2.1	2.1

*Data from *Iverson et al.* [2010].

It seems that some scales are consistent while others vary significantly (**Table 2-8**). Calculations of the dimensionless parameters yield similar results (within 1 order of magnitude of each other) between ε , R , R_f , and C . One dramatic difference between nature and experimental results, both for *Iverson et al.* [2010] and our results, is seen in the ratio of flow motion to pore fluid pressure diffusion timescales, N_p . Another notable difference is between the Savage number and, therefore, inertial number I values at the U of M are similar to the tabletop experiments *Iverson et al.* [2010] presents but vary from those in nature by a wide margin. Because I is utilized so prevalently in description for rheology [*Forterre and Pouliquen*, 2008; *GDR MiDi*, 2003; *Cassar et al.*, 2005], solving debris flow rheology based on table-top experiments may be troublesome. Still, the purpose of these experiments is not to solve the rigorous rheology debris flow question, but to focus on the granular interaction between interstitial fluid and particle in a controlled setting. Looking between columns 6 and 7 (**Table 2-8**), we see that our two experiments only change the viscosity (and therefore the fluid and bulk density). With this, the Reynold's number changes by 2 orders of magnitude; however, our water and highest viscosity experiments are within an order of magnitude elsewhere.

One drawback of using a table-top flume for relation to the field is that some effects of natural debris flows will be inaccurately represented. For instance, typically in nature a debris flow will expand perpendicular to flow, forming a flow margin leading to levees and possible avulsions; this flow margin is not developed in our system because to track the particle physics with our method, we needed the side of the flow to be similar across the entire width of the flume. The effect of other quantities such as fluid yield strength, viscous flow resistance, grain inertia, and pore fluid pressure may be disproportionately represented in the tabletop debris flow experiments [*Iverson et al.*, 2010]. Yet, there is one fault in comparing these numbers to *Iverson et al.*; we do not know how close "close" is. It is difficult to say what a significant difference or similarity is in these comparisons.

3 Results: effects of interstitial fluid viscosity on entrainment dynamics

In this section, we review the results from our experimentation. Through both macro and micro-scale results, we determine how the changing of viscosity affects the advance of our experimental debris flows.

3.1 Net erosion

The net mass eroded from the flume bed provides a relatively simple measure of debris flow erosion. The measure produces relatively little mechanistic information on what controls bed erosion. Yet there are a number of reasons to consider how the net erosion is affected by changing interstitial fluid. First, it provides a first-order result of what might be called the entrainment magnitude or “strength” of a debris flow over a bed [Moberly, 2015; Longjas *et al.*, 2017]. The net erosion is directly related to the size of the experimental flow, associated with the massive hazard associated with field-scale debris flows. It also provides a baseline measure of erosion that is easily compared with other experiments and field scale results where there may be significantly reduced instantaneous data available such as that we obtain through particle tracking capabilities. Thus, we discuss our measurements of net erosion in some detail here.

To obtain a relative measure of net erosion (of particles only), m_e , from one experiment to the next we focus on a measure of growth of material over the duration of the experiment. To do so, we subtract the mass output from the system from that of the supply m_s (particles only) and divide it by the original mass supplied:

$$m_e = \frac{m_s - m_o}{m_s} \quad (13)$$

If $m_e > 0$, fewer particle mass leaves the flume than was supplied by the initial flow, so the experiment may be denoted *net depositional*. If $m_e < 0$ more particle mass exit the flume than was supplied, so the experiment may be denoted *net erosional*. Further, for the cases where $m_e < 0$ the magnitude $|m_e|$ can be thought of as the fraction by which the debris flow increases over the duration of the experiment before it is deposited at the outlet. The results from these experiments are shown in **Figs. 3-1** and **3-2**.

Perhaps surprisingly for such a simple measure, the relative net mass out of the flume is quite noisy. In the end we found the noisiness was likely related to the sensitivity of these results to the proximity of particle-fluid mixture in the bed to full saturation. To help alleviate this issue, we performed multiple trials for each experiment at each angle. We performed a linearized least square fit for each viscosity to obtain a general trend (**Figure 3-1**).

From these results we note that for all systems, the net erosion increases with angle of inclination, with similar slopes for all except the highest interstitial viscosity we used. This is similar to previous experiments using dry flows [*Moberly, 2015* and *Longjas et al., 2017*]. For this there was a slightly higher sensitivity of erosion rate to increase in angle for the 50 cP experiment, but otherwise, this dependence is similar for all systems. From these data, we can also calculate a neutral angle, defined by the angle at which there is no net erosion or deposition, a measure that can be associated with the yield strength of the system. We calculate this for each system based on the linearized best fit to the data (**Table 3-1**). In this case the neutral angle is similar for all systems (approximately 16.5°) except that for the lowest viscosity interstitial fluid, for which the neutral angle just over one degree smaller.

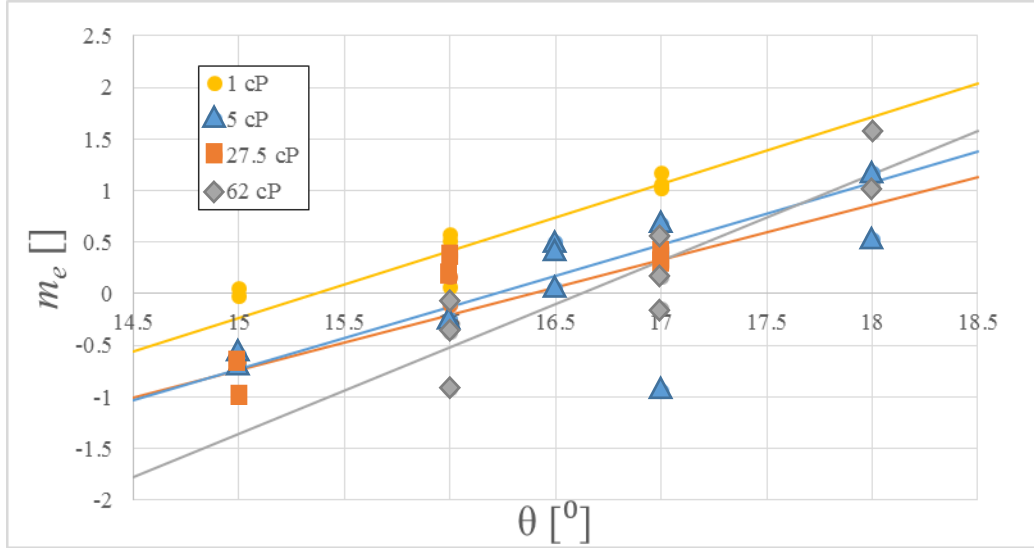


Figure 3-1. Results from experiments performed to determine the dependence of net erosion on flume inclination angle and interstitial fluid viscosity. The neutral angle of each data set is where the linear fit of each data set crosses the x-axis.

Table 3-3. Coefficients obtained from linearized least squares fort for the neutral angle results

Viscosity (cP)	slope	y-intercept	Neutral Angle ($^{\circ}$)
1	0.6485	-9.9609	15.36
5	0.5367	-8.7944	16.39
25	0.6026	-9.7733	16.22
62	0.8413	13.983	16.62

shown in Figure 3-1.

To determine acceptable boundary conditions under which to perform all of the erosion rate experiments, we re-plot the m_e data in **Figure 3-1** as a function of viscosity. With those data, we plot additional net erosion results from experiments using three additional interstitial fluid viscosities $\mu_{fl} = 12, 19, \text{ and } 50$. We performed the experiments to obtain these data using a flume inclination angle $\theta = 16.5^{\circ}$, the approximate neutral angle found from the glycerin-water experiments (**Figure 3-1**). The results plotted in **Figure 3-2** show that the net mass eroded from the bed near an inclination angle of $\theta = 16.5^{\circ}$ is similar (slightly positive or approximately zero) for all systems, with a slightly

decreasing trend with increasing interstitial fluid viscosity. Thus, we choose this angle of inclination to compare the erosion rate data from our experiments.

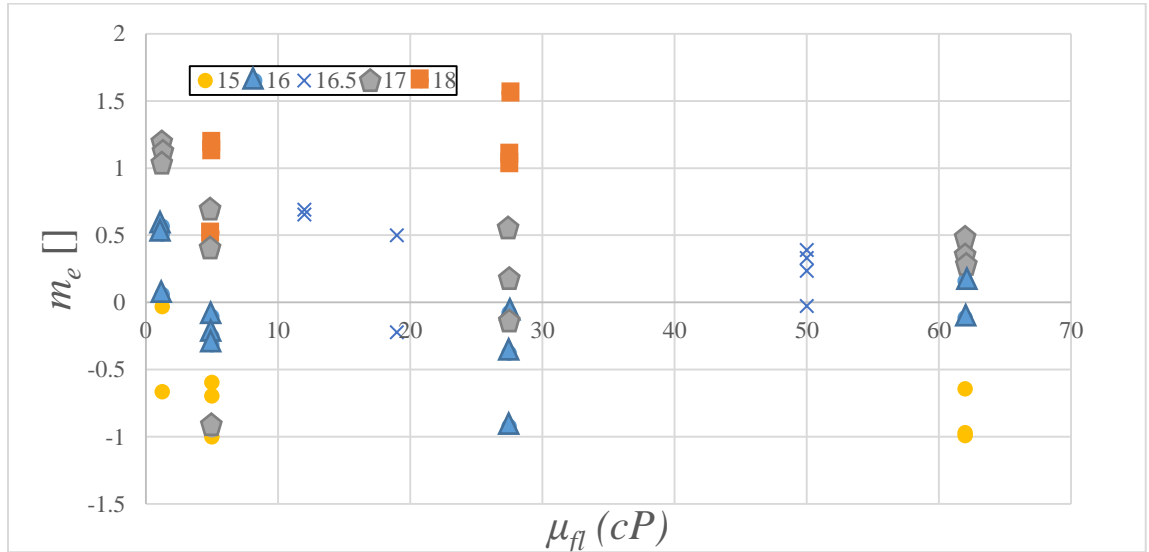


Figure 3-2. Plot of the mass eroded, m_e , plotted as a function of the interstitial fluid viscosity, μ_{fl} . Data includes all data shown in **Figure 3-1** along with additional data for three additional viscosities used for the instantaneous erosion experiments (below).

3.2 Instantaneous entrainment rate

While the net mass out is similar for most of the experiments described in section 3.1 when the flume was inclined at 16.5°, there is much more richness in the instantaneous data, such as the critical heights defined previously and in **Figure 3-3**. As the flow passes through, the interfaces between dense and sparse flows and between flowing and moving layers dramatically changes. We plot these for our entrainment rate experiments (experiment set 2) in **Figure 3-4**.

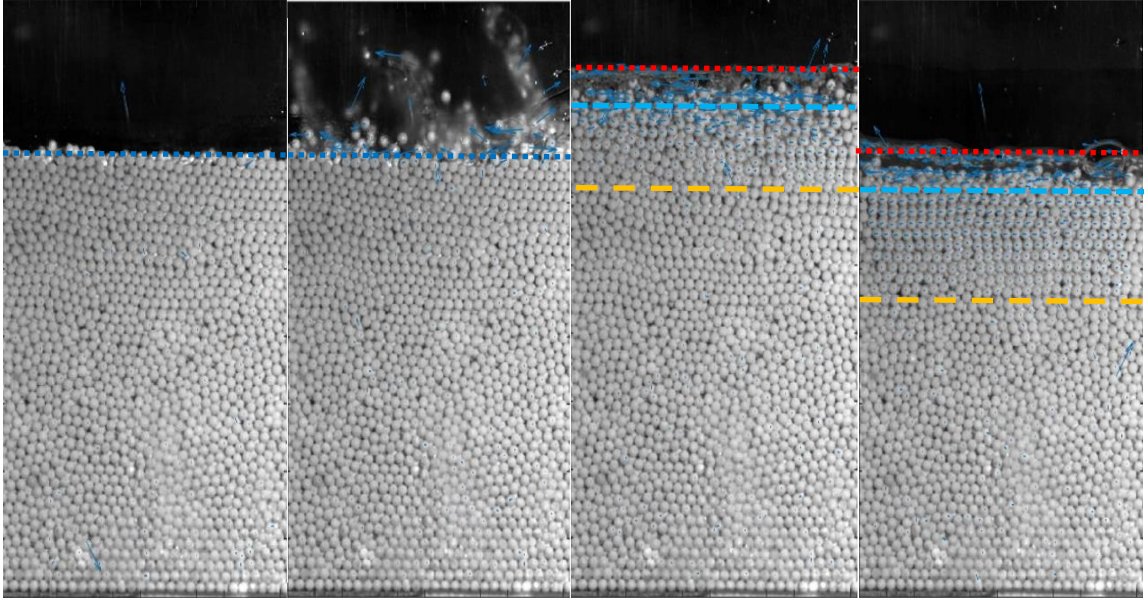


Figure 3-3. The instantaneous velocity of each particle from the tracking algorithm is shown in these images. The images from left to right are at $t = 0$, $t = 0.75$ (near flow transition), $t = 1.2$, and $t = 3$ seconds from the E2_12_T1 experiment. Lines denote the transitional layers: fluid top layer (short dash), dense flowing layer (dash), and entrainment height (long dash).

From the plots in **Figure 3-4**, we can see that for all experiments the tops of the dense and sparse flowing layers, y_{top} and y_{DFL} , respectively (that could be associated with the hydrographs for different cases) increase early in the experiments and keep a relatively constant distance from one another. The thickness of the sparse layer associated with the difference between these two heights is relatively constant for all flows and approximately equal to a few particle diameters (see also **Figure 3-5(a)**). A small exception might be that the thickness of the fluid layer decreases in some cases (5 cP and 12 cP), but is relatively consistent throughout higher viscosity (25 and 50 cP) systems. The height associated with the bottom of the flow, H (that we associate with an entrainment height) decreases with the initial impact of the flow. Initially, H starts at the top of the bed, as there is no movement. Then, just particles reach the camera imaging location, but soon after this the bulk flow, including interstitial fluid and particle, arrives. When the bulk flow enters, the originally stationary particles begin moving, thus lowering the entrainment height in each case. Beyond those similarities there are

significant differences from one experiment to the next as the interstitial fluid viscosity increases.

One notable difference involves the timing of the increase and decrease of the tops of the dense and sparse flowing layers – i.e., the shapes of these “hydrographs”. For the lower viscosity interstitial fluids, the heights peak relatively early in the experiments and then quickly decrease as the flow passes the camera. For the higher viscosity interstitial fluid experiments, the initial peak in each of these hydrographs occurs relatively quickly, but the decrease is somewhat longer indicating a longer “tail” to these flows. For the experiments with the highest interstitial fluid viscosities (E2_50), the hydrograph increases and does not decrease over the duration of the image analysis, indicating a significantly longer tail to the flows.

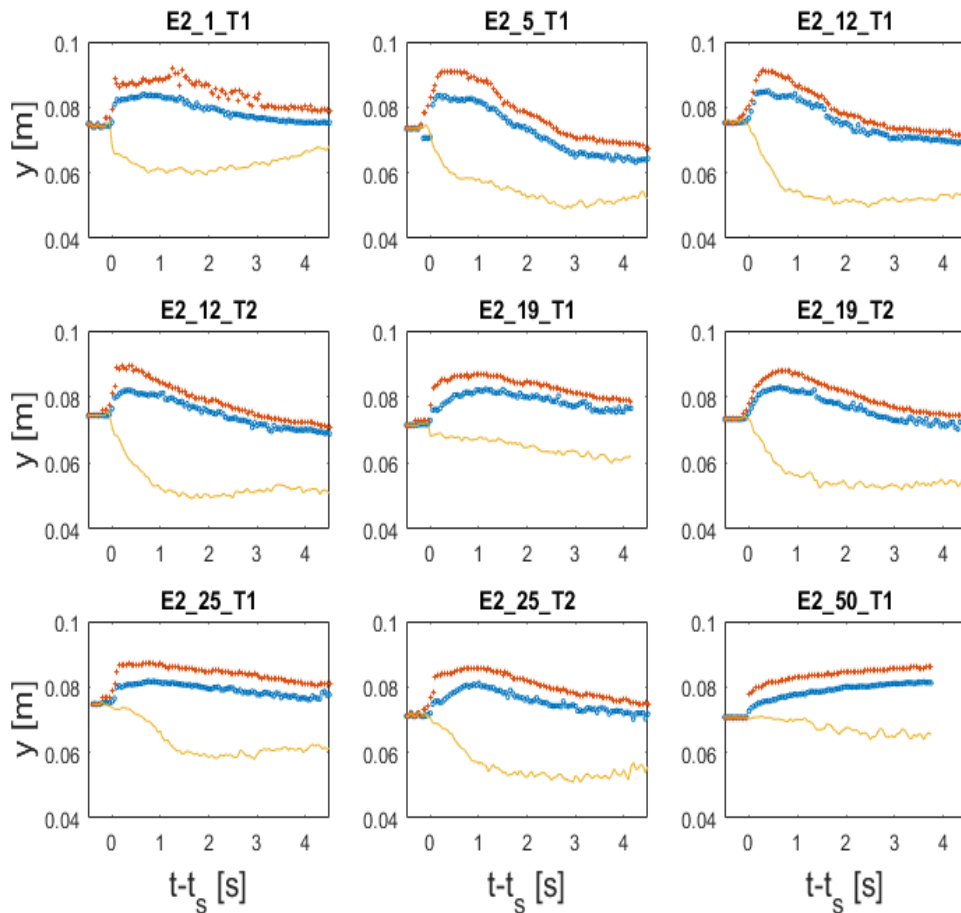


Figure 3-4. Different critical y values. The top of the dense flowing layer, y_{DFL} (circle), top of the fluid layer, y_{top} (+), and the entrainment height, y_{crit} (line).

The time dependence of the entrainment height – that is, the interface between the flowing layer and stationary bed and thus directly related to the instantaneous entrainment of the bed material into the flow, also changes with changes in the interstitial fluid viscosity (see also **Figure 3-5**). For the experiments with the lowest interstitial fluid viscosity (1 cP) the entrainment height, H , decreases quickly and the recovers (quickest for the experiments with water). For the experiments with intermediate interstitial fluid viscosities (5 cP and 12 cP), the entrainment height decreases the most indicating the

most (local) entrainment and associated bed disturbance over the duration of the experiment. For experiments with slightly higher interstitial fluid viscosities (19 cP and 25 cP) H decreases somewhat less, and does not start to recover over the duration of the imaging. For the experiments with the highest interstitial fluid viscosity (50 cP), H decreases significantly more slowly and does not even plateau over the duration of the imaging.

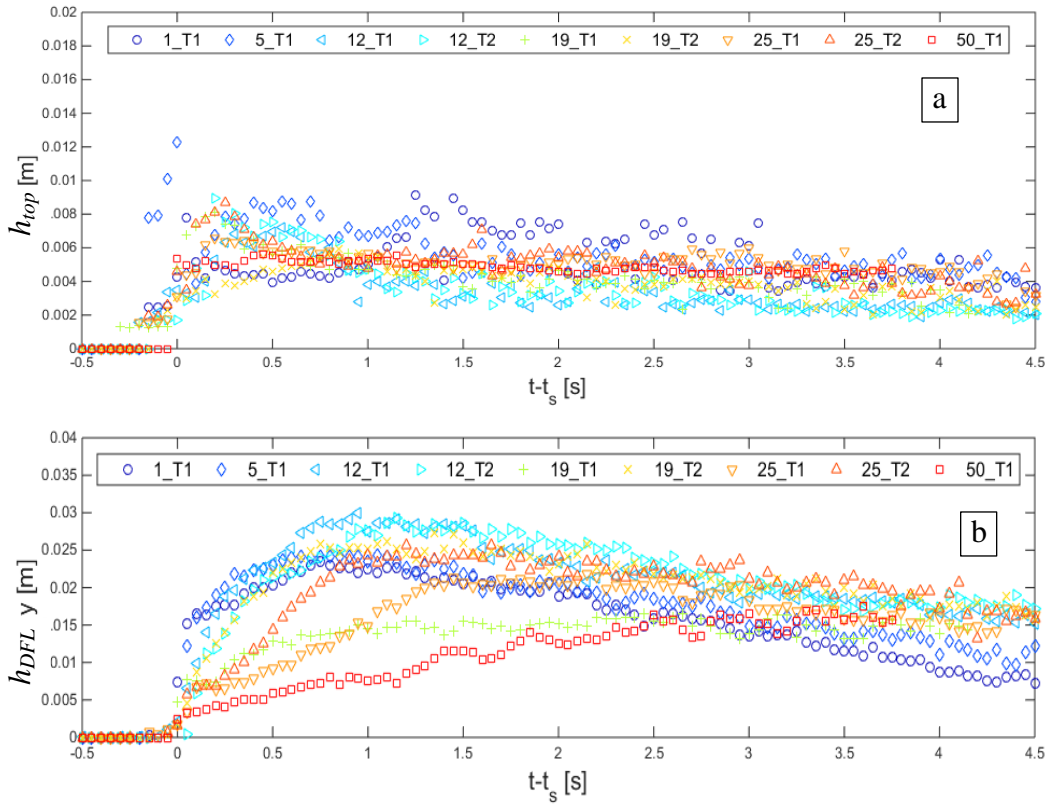


Figure 3-5. (Top) Thickness of the sparse fluid-like layer, $h_{top} = y_{top} - y_{DFL}$, through time. Some datasets are noisier than others. (Bottom) thickness of the dense flowing layer, $h_{DFL} = y_{DFL} - H$, through time.

The difference between the top and bottom of the flowing layer, $h_{DFL} = y_{DFL} - H$, the thickness of the dense part of the flowing layer, has perhaps the most systematic changes with changes in viscosity. Namely, the peak in the thickness occurs the soonest for the experiments for the lowest viscosity interstitial fluids and is increasingly delayed with

increasing interstitial fluid viscosities. With the exception of the experiments with the 12 cP viscosity interstitial fluid, the peak value of the thickness decreases with increasing viscosity, and the peak also broadens.

As mentioned earlier, the time dependence of the moving interface between stationary and moving particles, also known as the entrainment height, is critical to understanding the dynamics of a debris flow, particularly associated with the entrainment rate. In **Figure 3-7** we plot the temporal derivative of H , $\dot{e} = -dH/dt.$, and recall that a high entrainment rate signals that the flow is entraining material quickly; a low entrainment rate signals that the flow is entraining material slowly, and a negative entrainment rate signals that the flow is depositing into the bed.

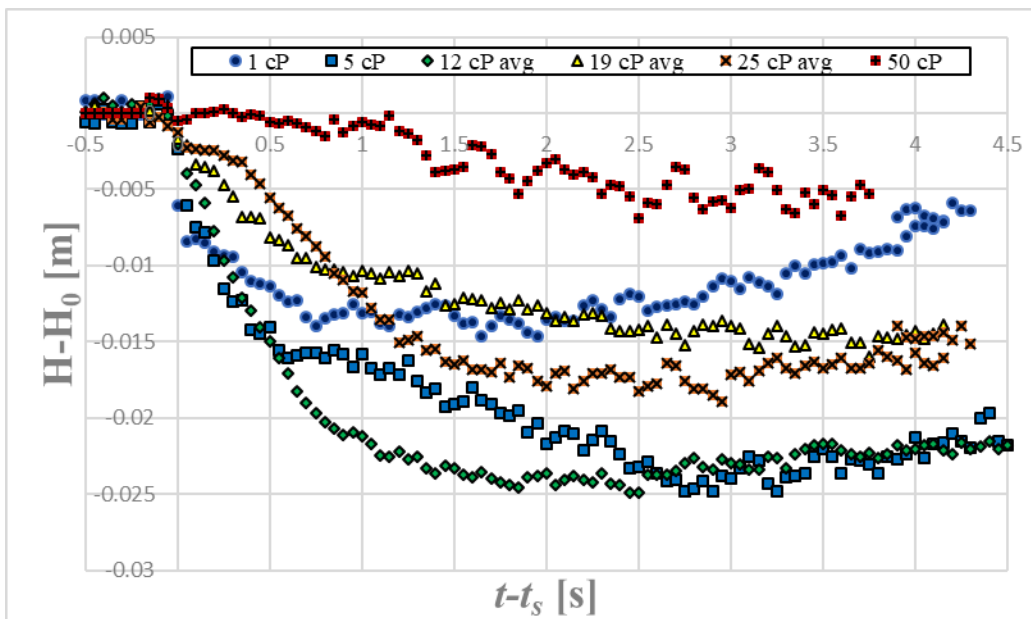


Figure 3-6. The entrainment height, H is tracked through time. For 12, 19, and 25 cP there are 2 datasets averaged and for 1, 5, and 50 cP a single set is tracked here.

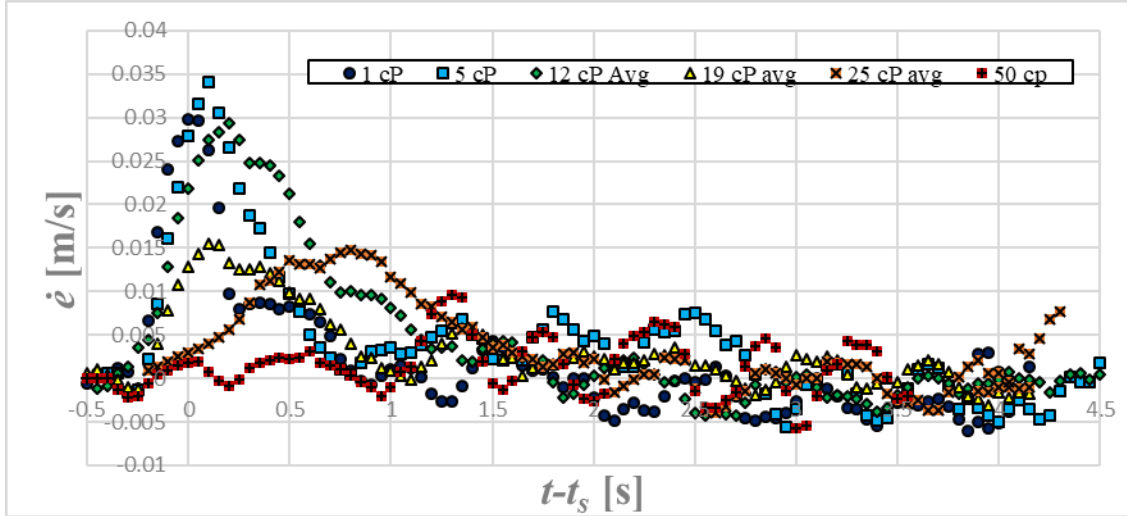


Figure 3-7. Entrainment rate (\dot{e}) as a function of time plotted for experiments with viscosities as noted in the legend.

As the drop of the entrainment height associated with the flow front is so dramatic, the entrainment rate is typically highest within 0.5 s of when the flow reaches the camera focal point. After the peak, the entrainment rate drops relatively quickly, associated with a plateau in the entrainment height. The flows with the highest interstitial fluid viscosities (25 cP and 50 cP) provide exceptions. The peak in entrainment height for the 25 cP experiment occurs somewhat later than the lower viscosity experiments and the peak also decreases somewhat slower, associated with the later plateau in the entrainment height plot. The entrainment rate for the 50 cP experiment is slightly positive throughout the whole experiment, corresponding to an entrainment height that slowly increases and does not appear to reach its minimum while the camera is still recording.

3.3 Measures of Proposed Erosion Drivers

In this section we report three measures of previously proposed erosion drivers introduced in Chapter 1: (1) a measure of the shear stress on the bed; (2) a measure of the granular temperature at the bed / flow interface, and (3) pore fluid pressures

3.3.1 Bed shear stress

In **Figure 3.9** we plot the time dependence of the bed shear stress based on the weight of the overlying material (**Equation 2-10**). This measure is proportional to the average density in the full depth of the flow (sparse and dense flowing layer) multiplied by the depth of the flow ($y_{top} - H$). Since the solid fraction is not uniform throughout this flow, the shear stress is loosely but not strictly proportional to the depth of the flow. As the top of the dense flowing layer increases, the shear stress increases as well. The shear stress reaches a maximum between 0.7-1 s for the 1 cP experiment. Notice that in the 50 cP case, τ increases from beginning to end of the video and also starts at lower shear stress.

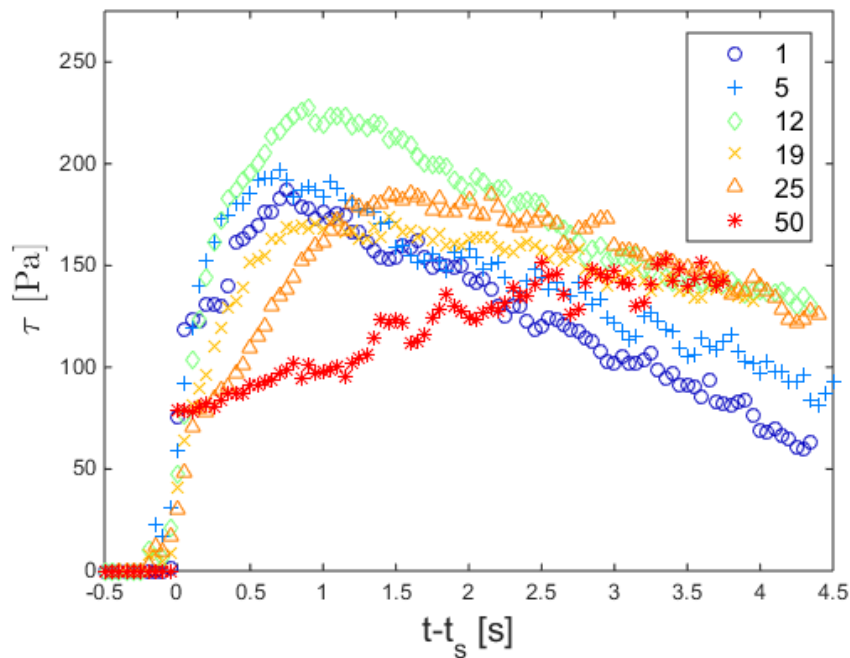


Figure 3-8. Shear stress (τ) through time for experiments with different viscosities. This includes both the dense and sparse flowing layers. The 12, 19, and 25 cP data are averaged between 2 trials.

In many ways since the shear stress is loosely associated with the flowing layer thickness, and the sparse flowing layer has a relatively constant thickness, similar for all

experiments regardless of the interstitial fluid viscosity, the shear stress has many of the same qualities that we described for the dense flowing layer. The shear stress, τ experiences systematic changes with changes in viscosity. Namely, the peak in the shear stress occurs the soonest for the experiments using the lowest viscosity interstitial fluids and is increasingly delayed with increasing interstitial fluid viscosities. With the exception of the experiments with the 12 cP viscosity interstitial fluid, the peak value of τ decreases with increasing viscosity, and the peak also broadens.

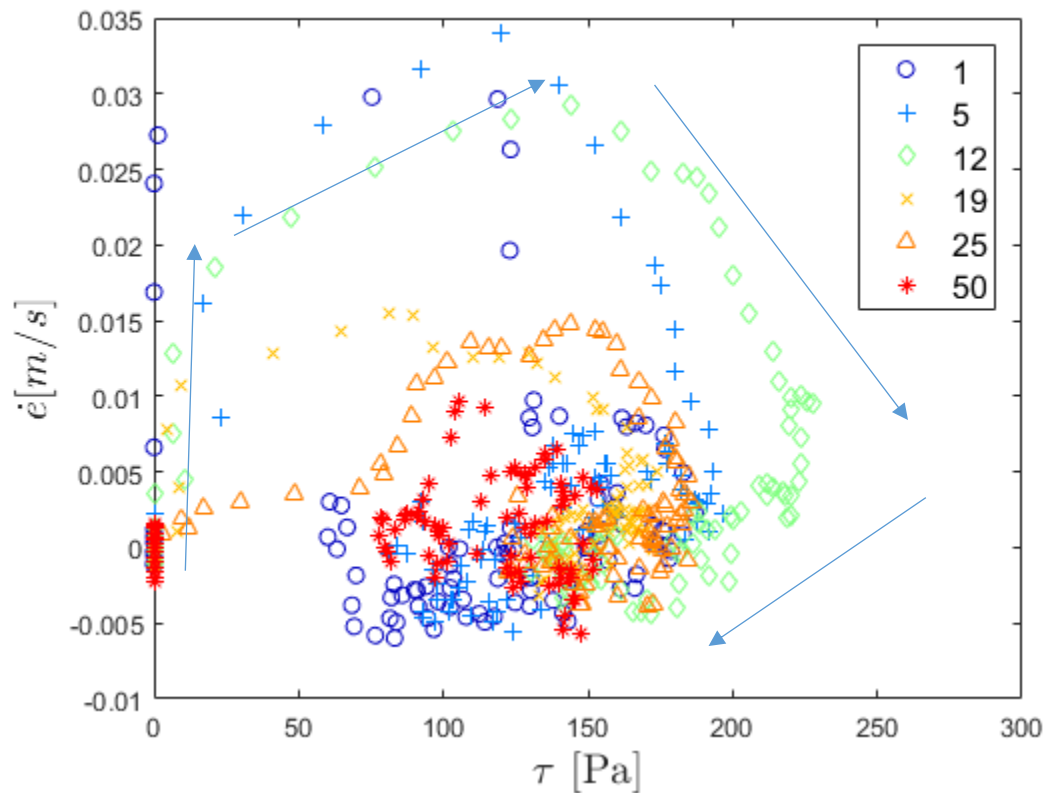


Figure 3-9. A parametric plot of the entrainment rate versus shear stress from the data in **Figs. 3-7** and **3-8**. Interstitial fluid viscosities are noted in the legend. Arrows note the change in data with progression in time.

To investigate the hypothesis that the entrainment rate depends on bed shear stress, we present a parametric plot of the entrainment rate data with the shear stress in Figure 3-9. The arrows indicate the co-evolution of \dot{e} and τ in time. First \dot{e} increases and τ remains

zero. Then there is a short period that the two increase together. Then after \dot{e} has reached its peak, τ typically is still increasing while \dot{e} falls. Finally \dot{e} stabilizes and τ begins decreasing. From these data, we can see that, at best, there is only a short-lived positive relationship between \dot{e} and τ , and as noted for dry flows [Delaney, 2015 Longjas et al., 2017], likely it is not a causal relationship. This will be further elaborated in Chapter 4.

3.3.2 Granular temperature at bed-flow interface

As mentioned in Chapter 1, granular temperature *has* been correlated with entrainment rate both in field measurements [Berger, 2011; McArdell, 2007] and smaller laboratory experiments [Moberly, 2015; Longjas et al 2017]. We investigated whether or not this correlation holds in our wet smaller laboratory experiments. The results in all cases were that, unlike our dry experiments, there was essentially no positive correlation between granular temperature and entrainment rate, as shown for one case in Figure 3-10. As shown by the arrows which follow the co-evolution of T and \dot{e} with time. The granular temperature first increases with the initial very sparse flow before entrainment rate begins to grow. Then T stagnates while entrainment rate increases; followed by T dropping and \dot{e} staying near maximum. Finally \dot{e} decreases as the temperature is near zero for the remainder of the flow. This all occurs in a counter-clockwise fashion in **Figure 3-10**.

For Reynold's shear stress, similar advancement through time is witnessed, but τ_R rather than increasing and then decreasing like T , decreases and then increases. Throughout these experiments, τ_R is significantly smaller than T suggesting that the horizontal velocity and fluctuations are a greater component. Therefore, Reynold's shear stress is ignored throughout the remainder of this thesis. These results are comparable for all experiments, so we do not explore them further in this thesis.

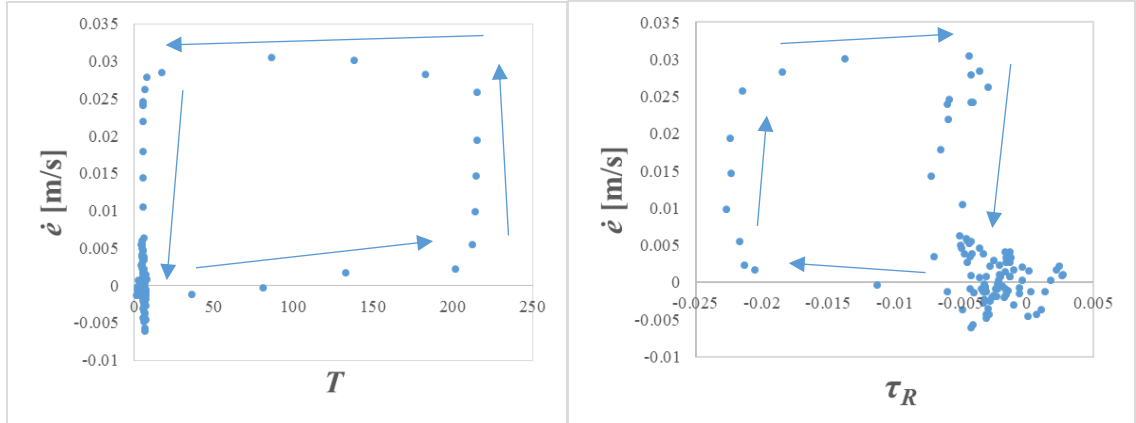


Figure 3-10. (Left) A parametric plot of the entrainment rate as a function of the granular temperature, T from E2_12_T1. (Right) A parametric plot of the entrainment rate as a function of the Reynold's Shear Stress, τ_R from E2_12_T1.

3.3.3 Pore Fluid Pressure

Before considering the effect of pore fluid pressure on entrainment rates, we first consider the pressure data from one experiment. In **Figure 3-11(a)** we re-plot the data from **Figure 2-12**, with the time shift we use for all the other data in this chapter. Each sensor provides a set of data akin to a hydrograph for the pore flow. As the debris flow passes over the bed over the sensor, the pore pressure dramatically increases and slowly decreases, not unlike the time dependent height of the flow itself. The upstream pore pressure sensor reaches a peak before the other sensors; the downstream pore pressure sensor peaks last. The shift in peaks from one sensor to the next provides a measure of the rate of advancement of the front of the debris flow. Additionally, the peak and width of the pulse changes from one sensor to the next, suggesting that the debris flow height changes downstream as it entrains or deposits particles and fluids. The changes in the shapes from one sensor to the next likely provide information about the manner with which the fluid rises or falls at different points in the flow as the pulse diffuses as well as travels downstream. These and other flow dynamics are beyond the scope of this thesis, so we focus primarily on how the pore pressure evolution relates to the entrainment dynamics. To compare these data directly with the entrainment data, similar to the earlier

data, for the rest of this section, we plot only one out of every five-hundredth pressure data points of the filtered data (**Figure 3-11(b)**).

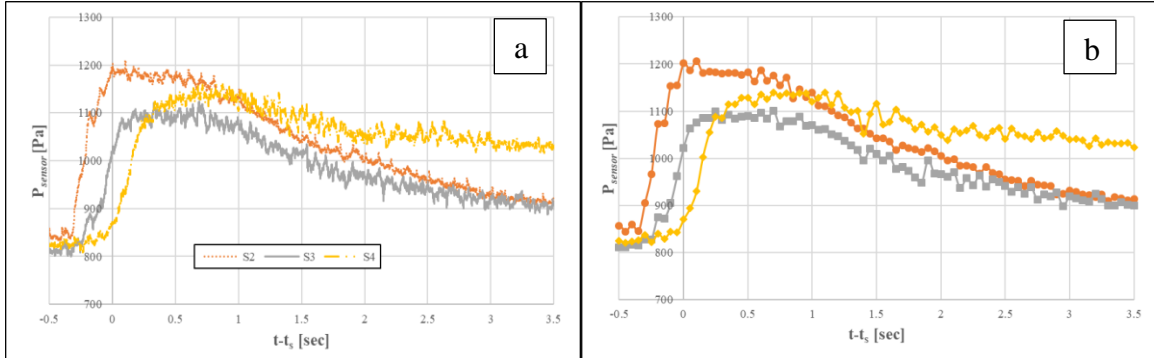


Figure 3-11. The Pressure from **Figure 2-17** is adjusted by an initial pore fluid pressure in the bed. (Right) The data with every 500th point selected, ready to be compared with the calculated pore fluid pressure.

For each condition, we consider the pore fluid pressure as measured by the sensors for one set of results for each viscosity in **Figure 3-12**. We note that the pressure sensor operation is extremely sensitive and, in many cases, only two sensors in the erodible bed were operational at a time. These are plotted along with the pore pressure calculated from data in the digital images based on assumptions that hydrostatic contributions *only* to pore fluid pressures (i.e., ρ_f = the density of the interstitial fluid) **Equation 2.9**.

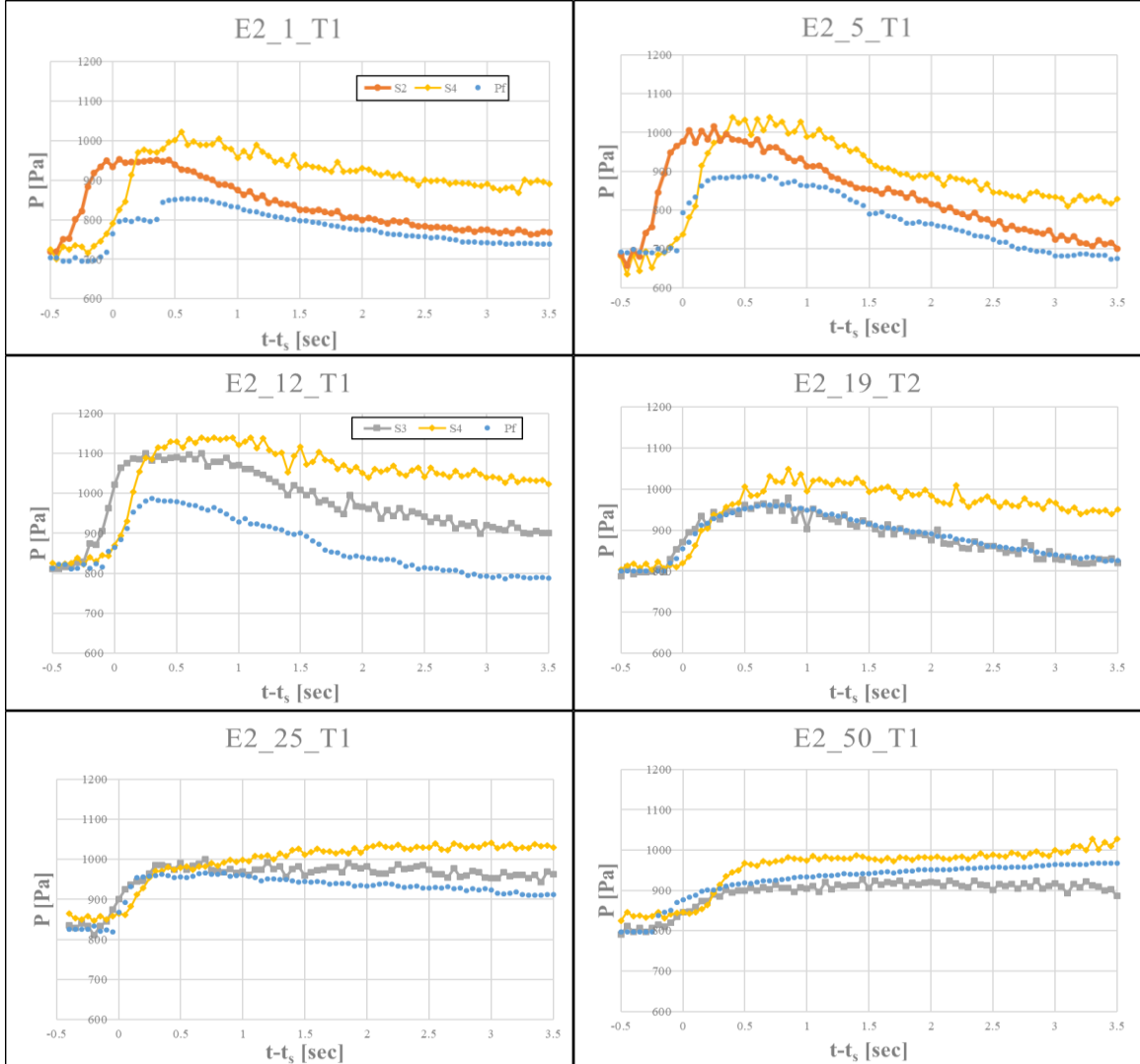


Figure 3-12: Pore pressure sensor data similar to **Figure 3-11b** from two representative sensors (in order of distance downstream: circle, square, and diamond). The pore pressure determined based on digital image analysis (dots) is calculated according to **Equation 1.9**.

In all cases, observations about the pore pressure sensor measurements could be similar to those in **Figure 3-11**. Namely, the downstream pressures peak later and higher, consistent with a peak particle-fluid flow height that is travelling downstream and increasing as it does so. The peak in the pore pressure calculated from the digital images occurs shortly before that of S4, consistent with the fact that we focus the camera at a spot between S3 and S4. Notably, the peak of this calculated pore pressure is less than

the peaks in the measured pore pressures. The difference between image-derived pore pressure and measured pore pressure decreases as the interstitial fluid viscosity increases and appears nearly eliminated for the 50 cP experiment.

To provide a more direct, quantitative comparison between measured and image-derived pore pressure, for each experiment we perform a weighted average of the measured pore pressures based on their relative distance downstream compared with that of the focus of the camera. The results are plotted with the estimated pore pressures in **Figure 3-13**.

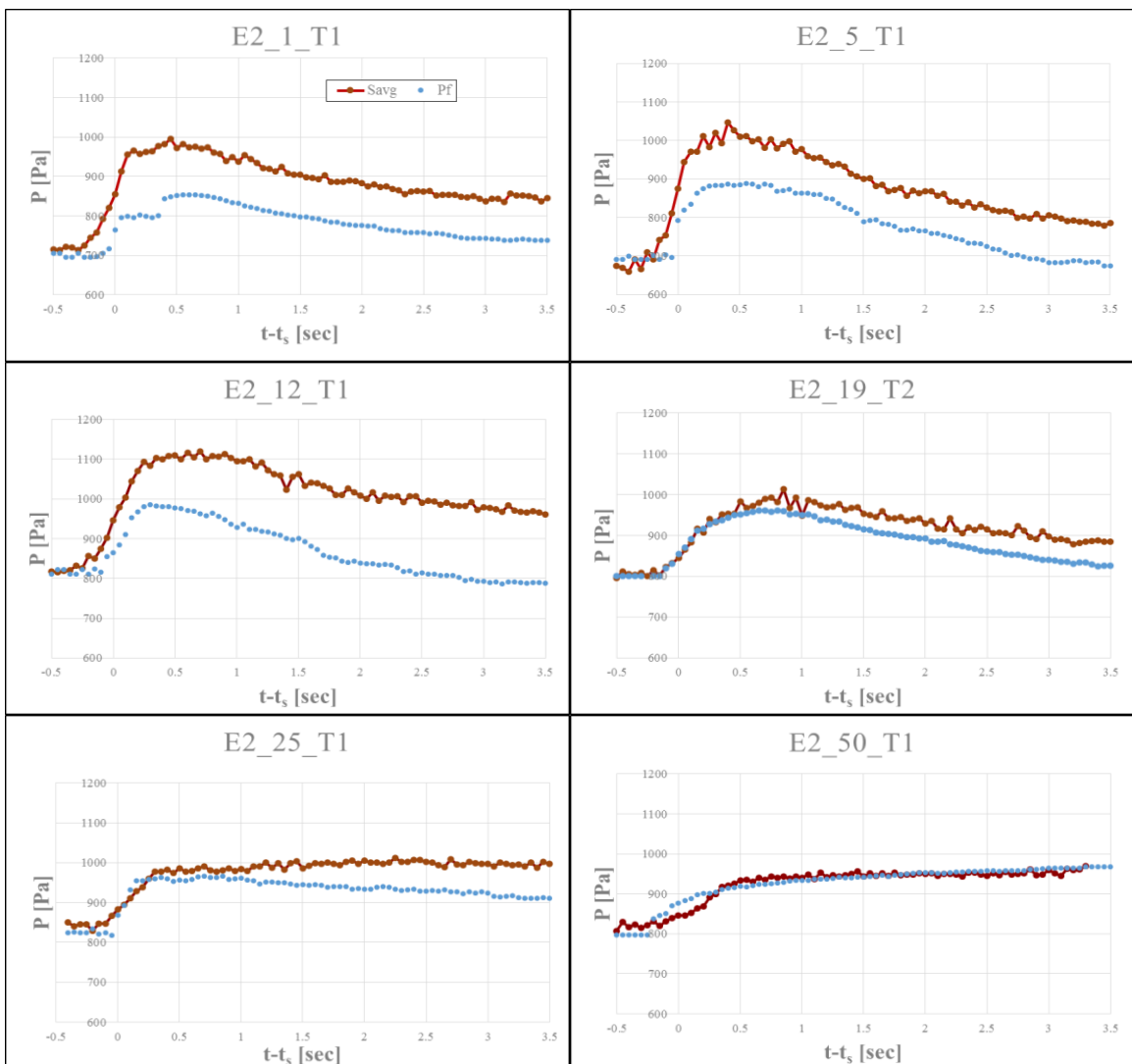


Figure 3-13. P_{sen} (using a weighted average pore pressure between two sensors, S_{avg}) plotted against P_{calc} (saying the density is only fluid, P_f) for each interstitial fluid viscosity trial.

In these plots, there is a clear and systematic difference between measured pore pressure and that calculated based on the digital images based on **Equation 2.9**. This difference tends to decrease as the viscosity of the interstitial fluid decreases, until it is essentially eliminated for the highest viscosity experiment (50 cP). For the lowest viscosity experiments (1 cP and 5 cP), the difference appears nearly constant throughout the experiment, and the measured and calculated pore fluid pressures peak at essentially the same time. For the intermediate viscosity experiments (12 cP and 19 cP) the measured pore fluid pressures seem to peak after the calculated pore fluid pressure. For the next highest viscosity experiments (25 cP) the measured value continues to increase (slowly) after the calculated value peaks and begins to decrease (slowly). The pressures are nearly equal for the measured and calculated pore pressures for the highest viscosity interstitial fluid experiment (50 cP).

Plots of the excess pore pressure in **Figure 3-14** ($P_e = P_f - S_{avg}$ from the data in the figures) clarify these variations. For the experiments with the lowest interstitial fluid viscosities (1, 5, and 12 cP), the excess pore pressure is significant, supporting the observation that the image-derived data (**Equation 2.9** based on the density of the interstitial fluid) is significantly less than the pressure sensor data. The magnitude of the excess pore pressure decreases significantly for higher interstitial fluid viscosities (19 cP and 25 cP) though for these cases the difference increases with increasing time beyond the peak flow. For the experiments with the highest viscosity interstitial fluid, P_e is approximately 0 throughout the experiment. P_e actually dips below 0 near the beginning possibly related to an initial contraction of the bed when the debris flow impinges on the bed.

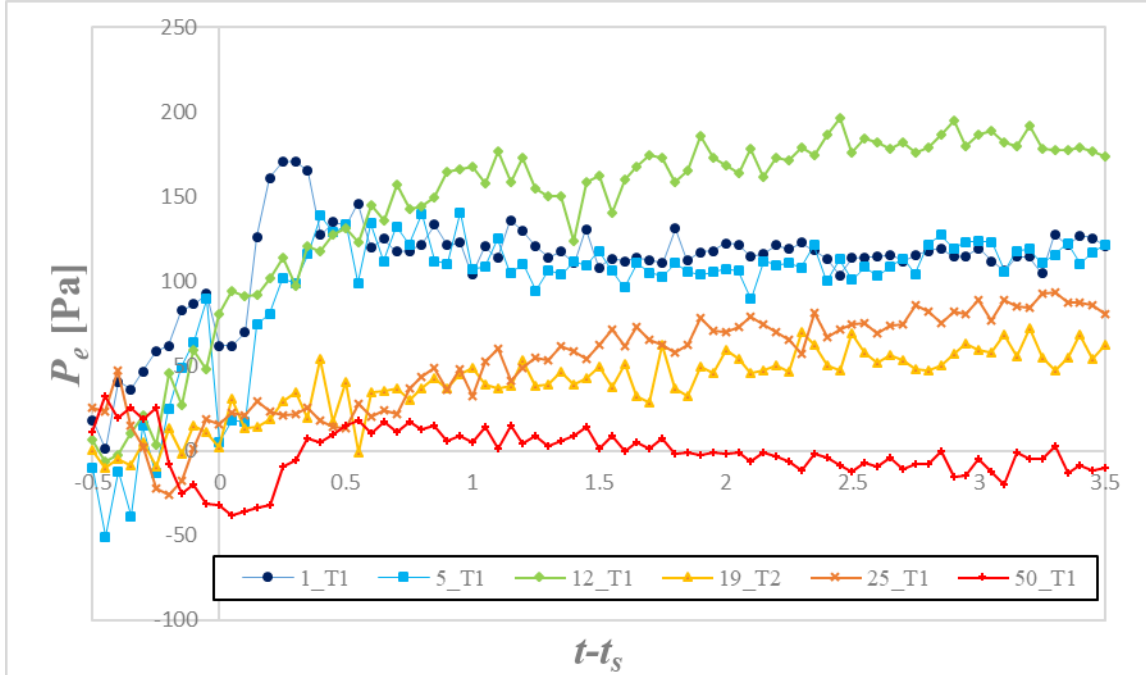
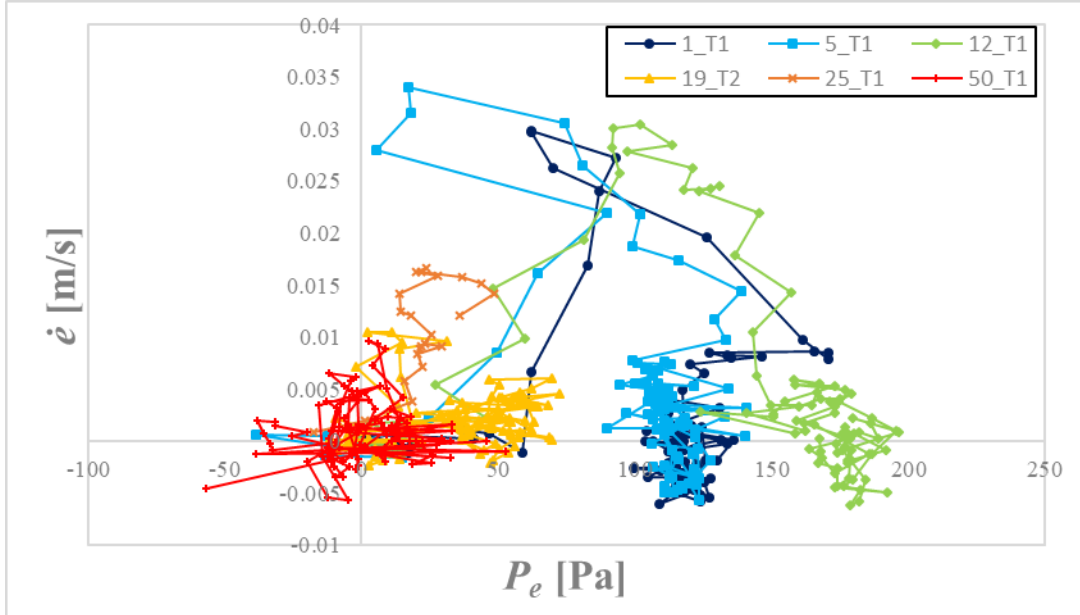
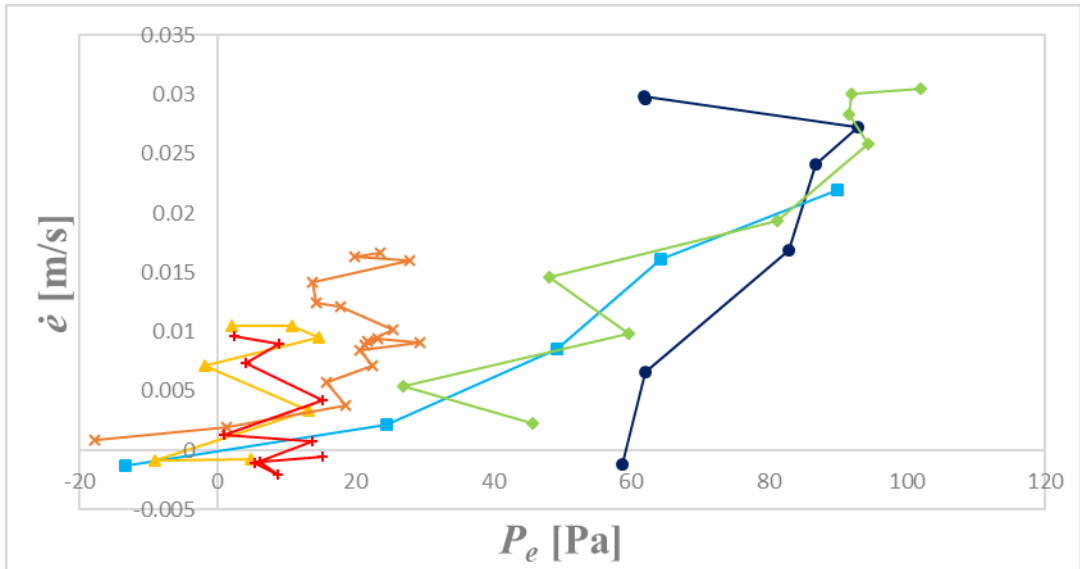


Figure 3-14. The excess pore fluid pressure ($P_e = P_{sen} - P_f$) is plotted for each interstitial fluid viscosity trial through time.

To explore whether or not the excess pore fluid pressure may be related to erosion rate, we plot a parametric plot of \dot{e} vs. P_e in **Figure 3-15(a)**, and a subset of these data along the approach to the peak in \dot{e} in **Figure 3-15(b)**. While through much of the experiment, the data plotted in **Figure 3-15(a)** indicate that \dot{e} is not well-correlated with P_e , the correlation between \dot{e} and P_e early in the experiment (**Figure 3-15(b)**) indicates that there may be a causal relationship during the increase of \dot{e} . We will further discuss the significance of this and the variability of these results with viscosity in Chapter 4.



(a)



(b)

Figure 3-15. (a) The entrainment rate, \dot{e} , plotted against the excess pore pressure from **Figure 3-14**. (b) The timeframe when the entrainment rate increases is magnified.

4 Discussion of laboratory experiments

We performed laboratory debris flow experiments to develop a mechanistic understanding of how erosional behaviors of a debris flow vary with changes in the interstitial fluid viscosity. To do so we considered both the net eroded mass, m_e , a measure of hazard associated with the size of a full-scale debris flow and the local instantaneous entrainment rate \dot{e} , a measure of the local time-dependent volumetric entrainment of stationary material into the flow:

- We found that for the boundary conditions and parameters in our debris flow experiments, the net eroded mass, m_e , depends strongly, specifically, linearly, on angle of inclination and only weakly on changes in our Newtonian interstitial fluids.
 - For any particular viscosity there is an approximate linear relationship between m_e and angle of inclination. This is similar to dry flows both in nature [Bouchaud, 1994] and on tabletop experiments with dry particle flows [Moberly, 2015 and Longjas et al., 2017]
 - There is a relatively high variability in m_e for any particular conditions; this sensitivity in m_e results from the saturation level of the erodible bed
 - Within the noise we can find a fitted “neutral angle”, the angle of inclination that yields an equal mass into the supply as out of the flume that provided relatively similar boundary conditions under which to perform our time-dependent erosion conditions.
- For understanding the dynamics of the experimental debris flows relevant to the instantaneous entrainment rate, we identified three qualitatively distinct vertical regions in the bed-flow architecture that smoothly transition in solid fraction, velocity, and granular temperature from one to the next:
 - a sparse energetic region on the top of the flow characterized by a low solid fraction, high velocities, and high velocity variances, bounded by:

- $y_{f_crit_top}$, on the top, identified according to a fixed low value of solid fraction and a representation of a local hydrograph
 - y_{DFL} , on the bottom, identified according to a fixed higher value of solid fraction and considered a point at which the solid fraction transitions to a higher more steady value approaching that of random loose packing.
 - a dense flowing layer characterized by a laminar-like transport of particles with a higher somewhat more constant solid fraction and slower velocities and velocity fluctuations than the top flowing layer. It is bounded by:
 - y_{DFL} on the top, summarized above
 - H on the bottom, identified according to a fixed (low) value of the downstream velocity, and a representation of the boundary between erodible bed and flow
 - The erodible bed, where the particles are essentially randomly close packed and nearly zero velocity, bounded by:
 - H , as defined above
 - the bottom of the flume
- In contrast to the essential independence of m_e from interstitial fluid viscosity of our experimental debris flows, the variations in dynamics of these layers and their boundaries show a high degree of sensitivity to this viscosity
- H decreases primarily when the flow first impacts the erodible bed. It decreases more quickly in lower interstitial fluid viscosity experiments but rapidly recovers; the minimum entrainment height of higher viscosities remains deeper longer even though this minimum is reached later, showing a similar result to the temporal elongation of h_{top}
- We used the time dependence of H to define the spatially and temporally variable entrainment rate, \dot{e} , a descriptor for the growth of a debris flow, a quantity that also, subsequently, varies substantially with interstitial fluid viscosity:

- \dot{e} peaks quickly and to a higher value for lower interstitial fluid viscosity experiments
- For the highest interstitial fluid viscosities, the peak in \dot{e} is significantly broader and smaller suggesting slower dynamics even as the net erosion is not substantially different
- We used digital image analysis and pore pressure sensors to study three previously proposed mechanisms for entrainment: shear stress, τ , granular temperature, T , and pore fluid pressure, P
 - Because τ is directly related to the height of both flowing layers ($h_{top} + h_{DFL}$), the trends through time are similar (e.g. peak shear stress and temporal elongation). We found little if any direct relationship between τ and \dot{e} .
 - In contrast with observations in dry particle flows (e.g., *Moberly, 2015; Longjas et al., 2017*) the granular temperature in these experiments similarly does not yield a clear correlation with entrainment rate, so we do not discuss it further here.
 - The temporal relationship between pore fluid pressures and entrainment rate seem to hold the most promising correlations for building an understanding of the effect of interstitial fluid viscosity on entrainment rates
- The basal pore fluid pressure P_{sen} measured directly is qualitatively similar to the image-based calculated pore fluid pressure, P_{calc} based on flow thickness and solid fractions, though there are substantial quantitative differences that vary with interstitial fluid viscosities. What we define as an excess pore pressure: $P_e = P_{sen} - P_{calc}$ is highest for the cases with the lowest interstitial fluid viscosities and the initial growth in P_e seems correlated with the initial growth in entrainment rate.

4.1 Implications of m_e results for measures of real debris flow dynamics and hazards

Before discussing the results in a bit more detail, we are admittedly cautious about applying the net erosion results in any substantial way to real debris flows. These results, more than anything else in the thesis, must be limited by size and dynamics scaling limitations, as well as the geometry of our fixed-side-wall, rectangular flume. On the other hand, some of the qualitative and quantitative results from these experiments in general and the distinct differences in the viscosity dependence of the results suggest specific lessons that should be considered in the context of interpreting and predicting field-scale flows and hazards.

4.1.1 Relative m_e Insensitivity to Interstitial Fluid Viscosity

As we noted above, our measurements of m_e are relatively independent of interstitial fluid viscosity compared with dynamics measurements of entrainment rate and other variables. Admittedly, this difference is not necessarily surprising. We note that m_e is a measure that integrates the effects of complex dynamics over the entire duration of the experiment whereas \dot{e} is reflective of a much more limited set of interactions. Still, it is not uncommon to use representative singly-valued results from the field such as net erosion to develop model parameters for predicting dynamics and associated hazards as well as understanding details such as material parameters, soil moisture, and climate effects of past debris flow events.

Indeed, we note that we have found that for dry debris flow experiments previously performed in the same flume, peak erosion rates scale similarly with net eroded mass [Moberly, 2015; Longjas *et al.*, 2017]. In contrast, the eroded mass in these experiments does not correlate well with peak erosion rates, even when eliminating outliers caused by an inadequately saturated bed. We suggest that the qualitative differences between the

dependence of instantaneous vs. longterm average debris flow measures on important debris flow properties (such as interstitial fluid viscosities) and boundary conditions represent an important set of results from these experiments that should be considered in more detail for future modeling efforts.

4.1.2 Neutral Angle Dependence on Viscosity

While the previous section suggests caution in over-interpreting the average results obtained from m_e , there are some details we feel are suggestive to a better understanding of debris flow dynamics, particular that of the neutral angle. The neutral angle is the angle at which there is no net mass out of the system. In experiment set 1, we systematically altered the viscosity of the interstitial fluid to see whether there would be a correlation between viscosity and neutral angle (e.g., higher viscosity \rightarrow higher neutral angle). However, we saw that the neutral angle is independent of the fluid viscosity. It is interesting to note that the neutral angle for 5, 25 and 62 cP are all near 16.5° suggesting a threshold (nonlinear) relationship between the viscosity and the neutral angle. The neutral angle for water was found to be 15.5° . However, this result is heavily dependent on the saturation of the erodible bed and is sensitive to the initial angle of inclination of the flume; any small difference could dramatically alter the relationship we see here. If the neutral angle experiments were performed again, additional trials at 12, 19, and 50 cP would be useful to clarify these relationships.

4.2 Dependence on Entrainment Dynamics on Viscosity

Here, we investigate the effect of the interstitial fluid matrix of a debris flow on its behaviors through laboratory experiments of particle-fluid flows and their erosive behaviors in an instrumented flume. We systematically vary, independently, the interstitial fluid in our debris flow and the erodible bed over which it flows. The results

from chapter 3 are elucidated for macroscopic results (mass eroded) and microscopic findings (video analyzed data) after the neutral angle has been determined. In particular, the effect of physical mechanisms (shear stress, granular temperature, and pore fluid pressure) are summarized.

4.2.1 Entrainment depth and rate

There has been previous discussion on how a higher fines content, and therefore higher viscosity, is related to magnitude [Major and Iverson, 1999; de Haas et al., 2016], yet how viscosity drives the ability for a debris flow to entrain has been largely left unresolved largely because of the difficulty in performing systematic experiments with these flows. We found that as the viscosity increases, the maximum entrainment does not necessarily increase. In fact, we found that the maximum entrainment depth is highest for cases with lower interstitial fluid viscosity, with the exception of water as the interstitial fluid. This result is surprising considering the non-linear relationship between the two components. In addition, this suggests that the maximum depth of entrainment is driven by something other than the physical mechanisms that are derived from viscosity.

One profound result of these experiments is that the fluid viscosity affects the entrainment rate of the system. The maximum entrainment rate is highest for lower viscosity systems. This means that, while the entrainment depth may be deepest for the 5 and 12 cP cases, the velocity of the stationary and vertically moving interface does not move as quickly for the highest entrainment depth. In addition, the maximum entrainment rate occurs earlier in lower viscosity cases. While the higher viscosities may not reach the maximum that the lower viscosities do, it is interesting to note that \dot{e} remains high for longer with higher viscosities.

The top of the fluid layer is essentially the hydrograph of the flow; basing some conclusions off of this, we see that the peak flow height across all flows is similar, with a slightly greater peak flow height being seen in 12 and 19 cP experiments and a

significantly lower height in 50 cP. Because the higher viscosity systems have a lower flow height and contain the same initial volume, we know that the flows are travelling differently as they continue down the flume. In particular, the flow expands in the direction of flow, more so in higher viscosity than lower. This result also makes sense when looking at the maximum entrainment depth (**Figure 2-6**) which occurs at the end of the video for 50 cP.

4.2.2 Shear stress and granular temperature

One of the physical mechanisms that we expected to be related to the entrainment rate was shear stress. However, we found that entrainment rate increases with shear stress but only once the entrainment rate is almost at maximum. The maximum time period the two variables are correlated positively is 0.25 seconds (5 and 12 cP) after which all cases have a similar effect suggesting little relationship between the two. This calls into question related models for debris flow entrainment. For example, *Iverson* [2012] proposed that the entrainment rate is proportional to the excess shear stress at the entrainment interface. While we track the same interface, we found no such relationship. Additionally, *Iverson* [2012] theorized that at this interface there should be a discontinuity in the velocity profile. In our velocity profiles, we see no such discontinuity. While this indicates a reason for concern in models which rely on bed shear stress to predict and model entrainment rates, we note that there is a significant difference between the systems we study and the systems *Iverson's* [2012] model attempts to capture in terms of both particle size distribution and scale. The effects of these differences are a topic of ongoing investigation.

For a more general discussion of the shear stress results, particularly as they vary with interstitial fluid viscosity, we consider first the maximum shear stress. We observed this maximum is observed under similar interstitial fluid viscosity to that under which we observed the maximum entrainment depth. This means that the shear stress associated with the mass (e.g., the thickness) of the dense flowing layer (and possibly the top fluid

layer) can be associated with a maximum *depth* of entrainment even if it is not directly related to the entrainment rate. Similarly, as interstitial fluid viscosity increases, the peak in both maximum shear stress and maximum entrainment depth occur later in the experiment, supporting an underlying correlation between entrainment depth and shear stress, or at least between entrainment depth and debris flow thickness. Thus, in cases where an entrainment depth is needed, for example, in understanding the depth to which an underlying bed material is disturbed, a flow thickness might be sufficient.

4.2.3 Pore fluid pressure

Our results for pore pressure indicate that entrainment rate may be substantially influenced by excess pore pressure – the amount that measured pore pressure is increased compared to that predictive from hydrostatic conditions. In this section we try to understand what might be the source of this excess pore pressure and how our understanding of this could elucidate an increased entrainment rate with increased excess pore pressure.

We first try to account for the excess pore pressure by considering our observations of the different parts of the flow. We note that for most of the systems, the particles in the top layer are significantly sparser than the dense layer, and the interparticle contacts are somewhat less than in the dense layer and likely mitigated by fluid-particle interactions. Thus it is possible that the particles are in something like turbulent or collisional suspension. If this is the case, then we can consider them as part of the fluid in this layer and thus contribute effectively to an increased weight of the fluid, and an increased hydrostatic pressure. We replace the calculation of P in Equation 2.9d with:

$$P_{calc}' = P_{top_f}' + P_{DFL_f} + P_{st_f} \quad 4.1$$

where

$$P'_{top_f} = \rho g h_{top} \cos\theta \quad 4.2$$

And where, as before, ρ is the bulk average density ($\rho = \rho_s(1 - \eta) + \rho_f\eta$) in the region of interest; here, the depth-averaged bulk density in the sparse layer. In other words, we posit that even though the particle density is greater than that of the fluid density the particles within the top fluid layer are fluidized and represent their effect on the depth dependent density accordingly (**Figure 4-1**).

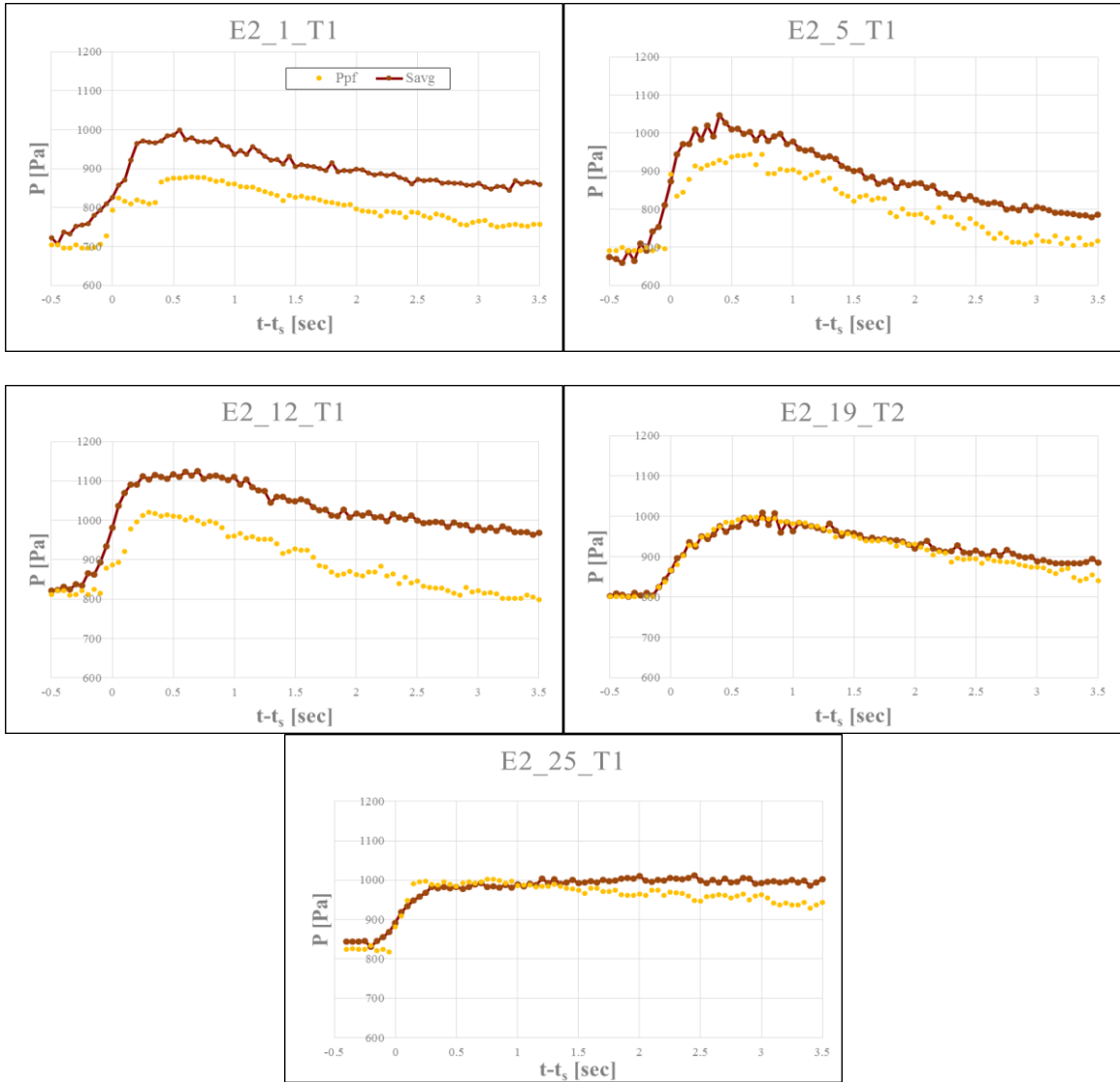


Figure 4-1. P_{sen} (using a weighted average pore pressure between two sensors, equal to Savg) plotted with P' calculated assuming the particles in the sparse layer are fluidized

(Equation. 4.2) for the five cases for which there appears to be some excess pore fluid pressure (excluding the 50 cp case).

We note that since the 50 cP experiments seems to have no excess pore pressure, we do not consider the top fluid layer to be in suspension, though this interstitial fluid viscosity-dependent cut-off behavior is a topic of interest for the future. We plot the excess pore pressure that remains after this consideration ($P_e' = P_{sen} - P_{calc}'$) in **Figure 4-2**. From this plot, it appears that for the experimental results from the systems of lowest interstitial fluid viscosity the excess pore pressure can be mostly accounted for by assuming that the particles in the sparse layer are fluidized. However, for the cases with the lower interstitial fluid viscosities there is some excess pore pressure that fully represented through the fluidization of the sparse layer.

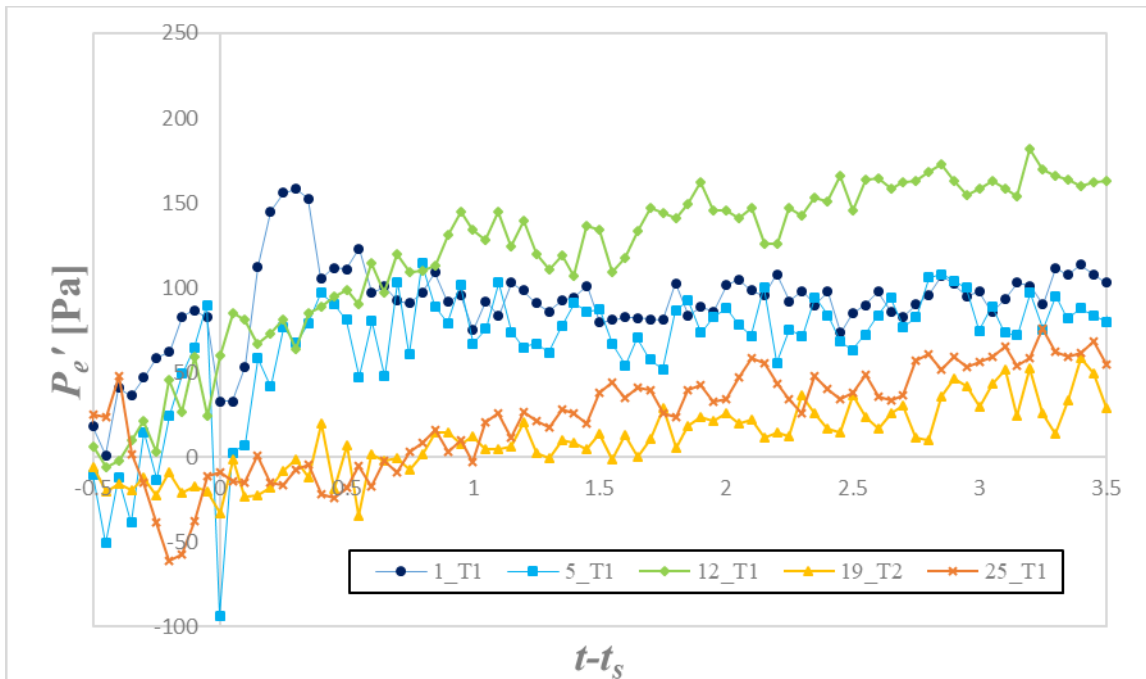


Figure 4-2. P_e' ($P_e' = P_{sen} - P_{calc}'$) is plotted through time, where P_{calc}' is the pore pressure of top fluid layer where the fluid and particle are fluidized.

To determine if the newly calculated excess pore fluid pressure P_e' is better correlated with the increase in entrainment rate, we parametrically plot the two variables against one another (**Fig 4-3**) over the same temporal range plotted in Figure 3-15(b). When looking at this figure, we see that the entrainment rate of the lower interstitial fluid viscosity systems seems to increase simultaneously to pore fluid pressure; whereas, the higher viscosity systems have a less convincing correlation. That is for the cases of the higher viscosity interstitial fluids, the correlation between excess pore fluid pressure P_e' and entrainment rate (**Figure 3-15(b)**) seem slightly better than the correlation between P_e' and entrainment rate (**Figure 4-3**). For the lower viscosity cases, the opposite is true.

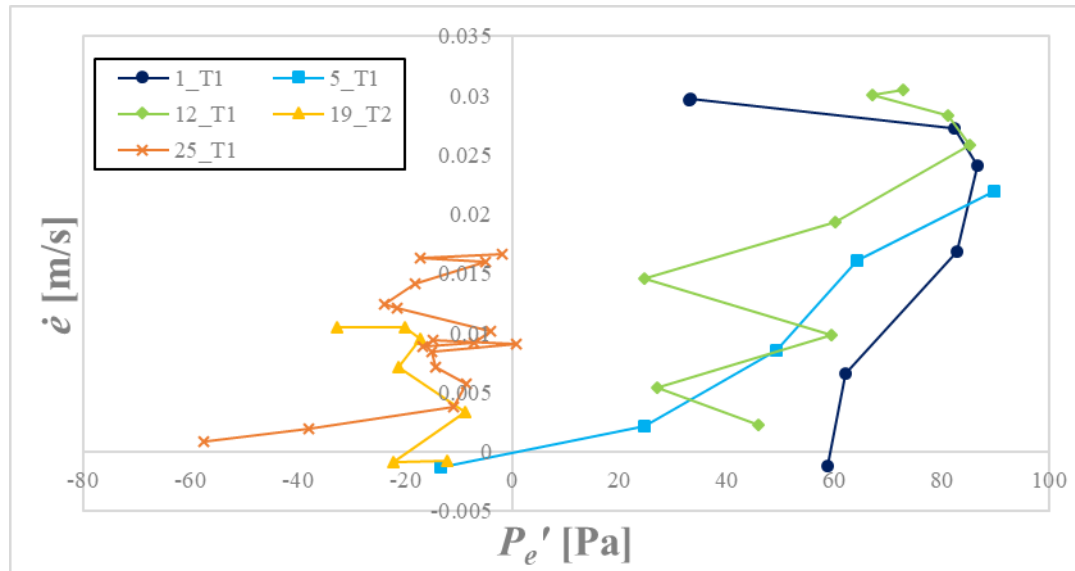


Figure 4-3. \dot{e} plotted against P_e' from **Figure 4-2** This is from a small portion where \dot{e} is increasing

We further investigate the source of the excess interstitial pore fluid, that is, that not accounted for by P_{calc}' for the cases with the lowest interstitial fluid viscosity trials (1, 5 and 12 cP). Based on our results that a fluidization of the particles in the top sparse layer seems to provide a reasonable source for part of the excess pore fluid pressure for all cases except those with the most viscous interstitial fluid, we consider the possibility that

in the least viscous cases, the sparse layer could be fluidized as well. Based on this, we calculate a new image-based pore pressure P_{calc} '':

$$P_{calc}'' = P_{top_f}'' + P_{DFL_f}' + P_{st_f}'' \quad 4.3$$

where

$$P_{DFL_f}'' = \rho g h_{DFL} \cos\theta \quad 4.4$$

where, again, ρ is the bulk average density ($\rho = \rho_s(1 - \eta) + \rho_f\eta$) in the region of interest; here, the depth-averaged bulk density in the dense flowing layer. In Figure 4.4, we see that this significantly over-estimates the pore fluid pressure as measured by the pressure sensors. To account for this, we note that our assignment of material to the top sparse layer vs. that we assign to the dense layer is based on an arbitrary definition of a critical solid fraction here. Further fluidization may be better associated with a critical shear velocity, perhaps in combination with a solid fraction. In other words, our consideration of what parts of the moving layer might be fluidized and might not be fluidized is in and of itself rather arbitrary. Thus, we investigate the effectiveness in assuming that part of what we call the dense layer is fluidized as well. We test this idea by re-calculating a fluid-based pressure resulting on assuming different fractions of the dense layer ξ are fluidized. In other words, in equation 4.3 and 4.4 we re-define P'_{DFL_f} according to:

$$P'_{DFL_f,\xi} = \rho_{DFL,\xi} g h_{DFL} \cos\theta \quad 4.5$$

In this equation, we note that $\rho_{DFL,\xi} = \rho_s(1 - \eta\xi) + \rho_f\eta\xi$ replaces the bulk density calculated for this region when assuming the particles are fluidized over the entire depth. When $\xi = 1$, the results are identical to the use of P'_{DFL_f} from Equation 4.4 used in Equation 4.3. When $\xi = 0$, the case is identical to that of Equations 4.1 and 4.2, when we assumed none of the particles in the dense layer are fluidized. The results for different

values of ξ are plotted in (Figure 4-4) for the three cases with the lowest interstitial fluid viscosity.

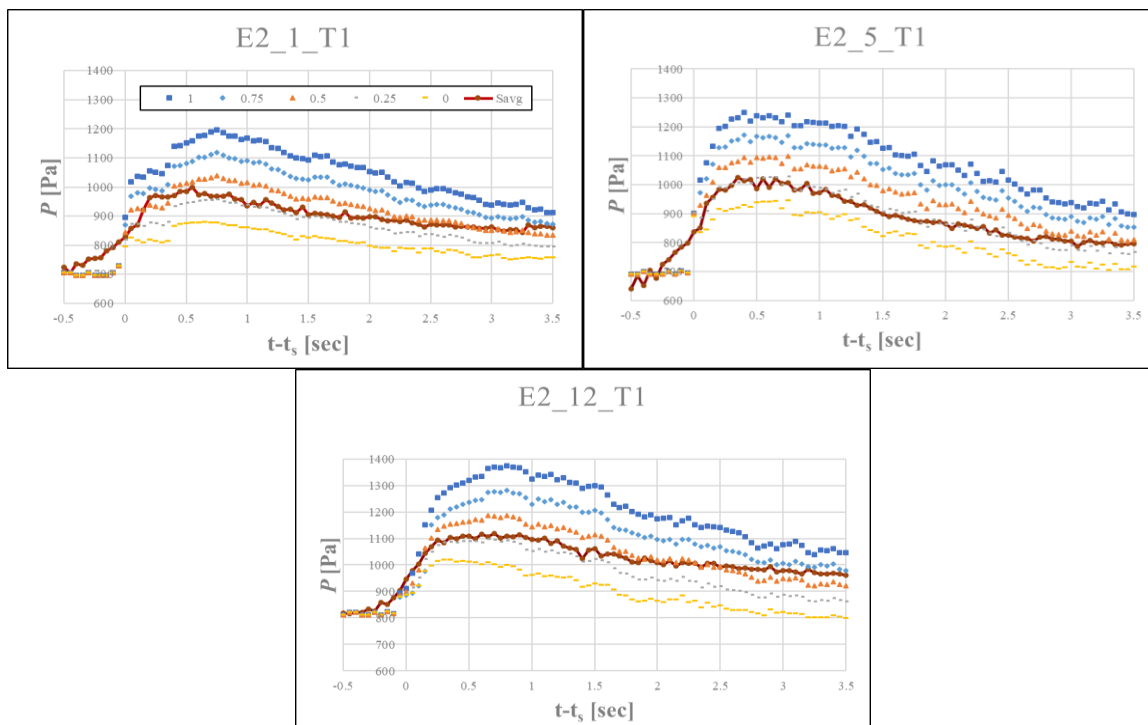


Figure 4-4. P_{sen} (Savg) is plotted against percentages of dense flowing layer assumed in suspension (for calculation of Equation 4.5) as labeled in the legend. Note that 0 is equal to P_{pf} from Figure 4-3 for each individual trial.

For all three of these cases with lowest interstitial viscosities, a value of $\xi = 0.25$ seems to bring the measured pressure closest to the image-based calculated pressure, particularly for the first 2 seconds of the experiment. For a more quantitative comparison,

we define a new excess pore pressure based on this ($P_e'' = P_{sen} - P_{calc}''$) and plot the results for these three cases in **Figure 4.5**.

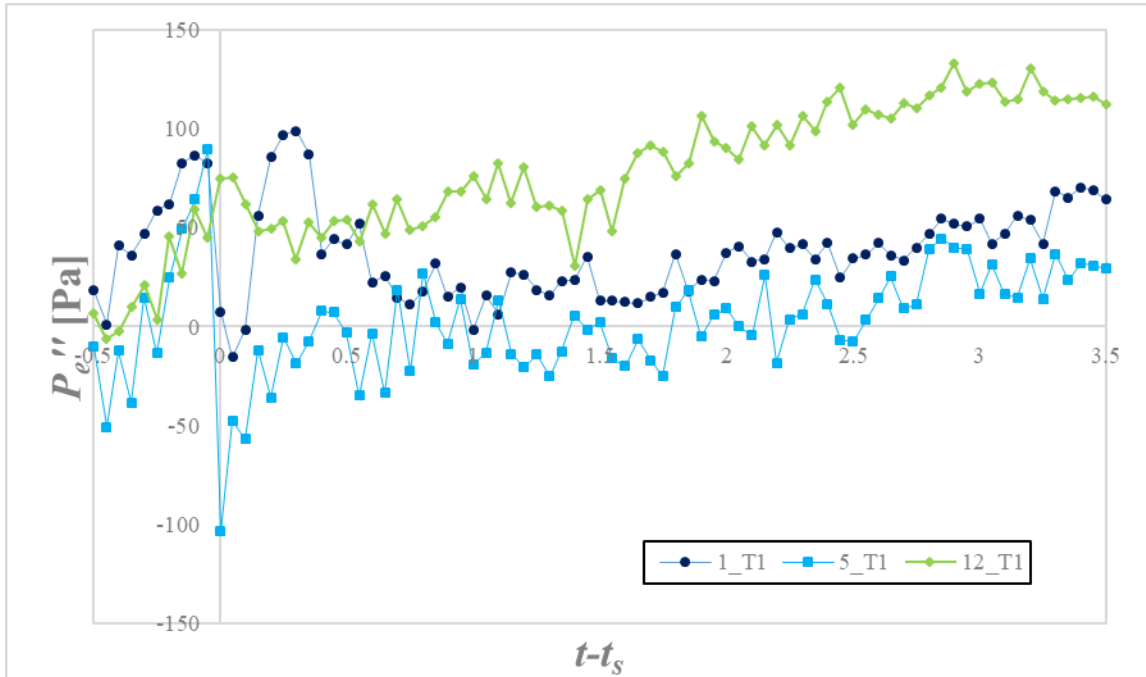


Figure 4-5. P_e'' ($P_e'' = P_{sen} - P_{calc}''$) plotted through time.

These new results indicate that the excess pore pressure (the measured pore fluid pressure that exceeds that predicted from the height of the flow) is due to the fluidization of particles in the top spares layer and a partial fluidization of the dense layer. We note that this accounting is not entirely consistent across interstitial fluid viscosity. This indicates to us that fluidization of the particles must be associated with dynamics in addition to (or other than) simply the local solid fraction, such as local shear rates and granular temperatures. This is a topic beyond the scope of the thesis and a subject of ongoing work in our group.

Having partially resolved the source of the partial fluid pressure over the duration of the experiments, we return our attention to the relationship between the newly adjusted excess pore pressure P_e'' and the entrainment rate in **Figure 4.6**. We note that these parametric plots are essentially identical to those in **Figure 4.4**. In other words, while in **Figure 4.5**, the plots indicate that we have effectively accounted for nearly all of the excess pore pressure for the three cases of lowest interstitial fluid viscosity in our experiments, we did not account for the part that seems to be correlated with the entrainment rates.

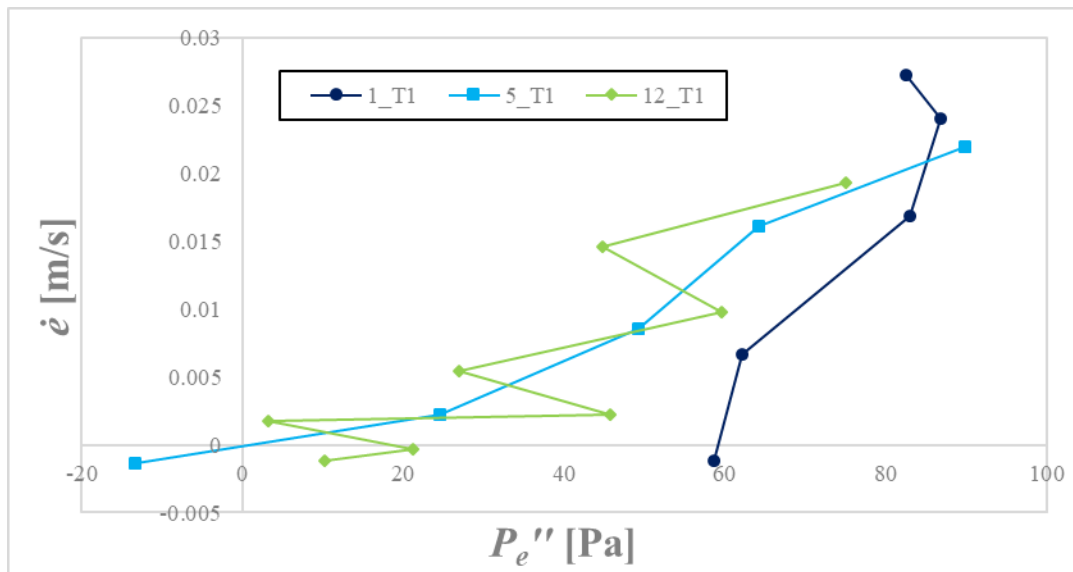


Figure 4-6. \dot{e} plotted against P_e'' from **Figure 4-5** The corresponding time is from $-0.3 < t - t_s < 0$.

To reconcile this apparent contradiction, we consider the temporal plots of excess pore pressure P_e'' (**Figure 4-5**) as compared with the temporal plots of the thickness of the dense flowing layer (**Figure 3-5b**) and the temporal plots of the entrainment rates (**Figure 3-7**). We note first that the entrainment rate increases most dramatically for

these cases before $t-t_s = 0$, that is before the denser part of the debris flow arrives at the location at which the images are being recorded. We note that this is also true for the excess pore pressure re-calculated based on a partial fluidization of the particles in the dense part of the flowing layer (**Figure 4-5**). In contrast, we note that the dense part of the flowing layer does not grow appreciably until $t-t_s > 0$. In other words these results imply that there must be some other source of pore pressure that we are not accounting for in these analyses that is significant during the initial impact of the debris flow with the bed. This may be associated with an initial compaction of the bed, as discussed in *Mangenay* [2009] which could be investigated by studying how this effect changes when bed initialization is changed systematically. While the source of this excess pore pressure is beyond the scope of the thesis, its presence is important as our results in **Figure 4-6** imply that it is likely driving the entrainment of bed material, particularly in particle-fluid flows in which the interstitial fluid viscosity is relatively low.

5 Field Data and Analysis

5.1 Toward Relating Laboratory Data to Field

Data

In order to understand the bearing of the experimental data on understanding field scale debris flows, we need a way to relate our simple flows of monosized granular materials with a viscous fluid with multi-sized particles, clay, and water in a real debris flow. To do so, we consider again statements such as those in *Iverson* [1997], indicating that the amount of fine particles (clay and silt) affects the viscosity of a typical field-scale debris-flow pore fluid is between 10^{-3} Pa-s (equivalent to that of water with few if any fine particles) and 10^{-1} Pa-s (thicker fluid with higher fine particle fraction). *Whipple and Dunne* [1992] found that debris-flow behavior is most controlled by the manner in which bulk-sediment concentration affects rheology of the interstitial fluid. Building in part on this idea, *Kaitna et al.* [2014] performed experiments in such a way that they considered, separately the influence of the grain size distribution of large ($> 2\text{mm}$) particles in a debris flow and the fine particle content (considered part of the fluid).

We performed our experiments on the somewhat lower side of the range suggested by *Iverson* [1997] for natural debris flows (1 to 60 cP compared with 1 to 100 cP typical of interstitial debris flow fluids in nature [*Iverson*, 1997]). Ideally, we would relate the grain size data from the field directly to interstitial fluid viscosities in our experiments. However, we were not able to obtain such data. Instead, we turn to the results from *Phillips and Davies* [1991] who determined that relatively high fine particle fraction in the overall grain size distribution leads to a plastic or viscoplastic flow. With this in mind, we consider grain size distributions from different fans in Owens Valley. In this case, historical weather patterns were likely the same from one fan to the next, but morphology varied from one to the next. We describe the field sites from which we

collected particles and data for grain size analysis in the next section and conclude this chapter by considering the implications of our results.

Here we briefly describe the field trip we took and then present the data we collected in Owen's Valley, CA. A discussion on how these data relate to the experiments performed in lab will be touched on, while describing some future possibilities.

5.2 Summary of Area

Owen's Valley is a depression formed from faults running parallel to the edges of two mountain ranges; the White and Inyo, to the east, and the Sierra Nevada, to the west. As a response to this relatively discrete depression, alluvial fans have formed through sediment transport out of the nearby mountains. This sediment transport has occurred primarily through gravity driven flows, particularly debris flows [*Whipple and Dunne, 1992*]. Loose sediment from high-elevation areas in combination with relatively rare, likely extreme water from rainfall events or snowmelt, formed these debris flows.

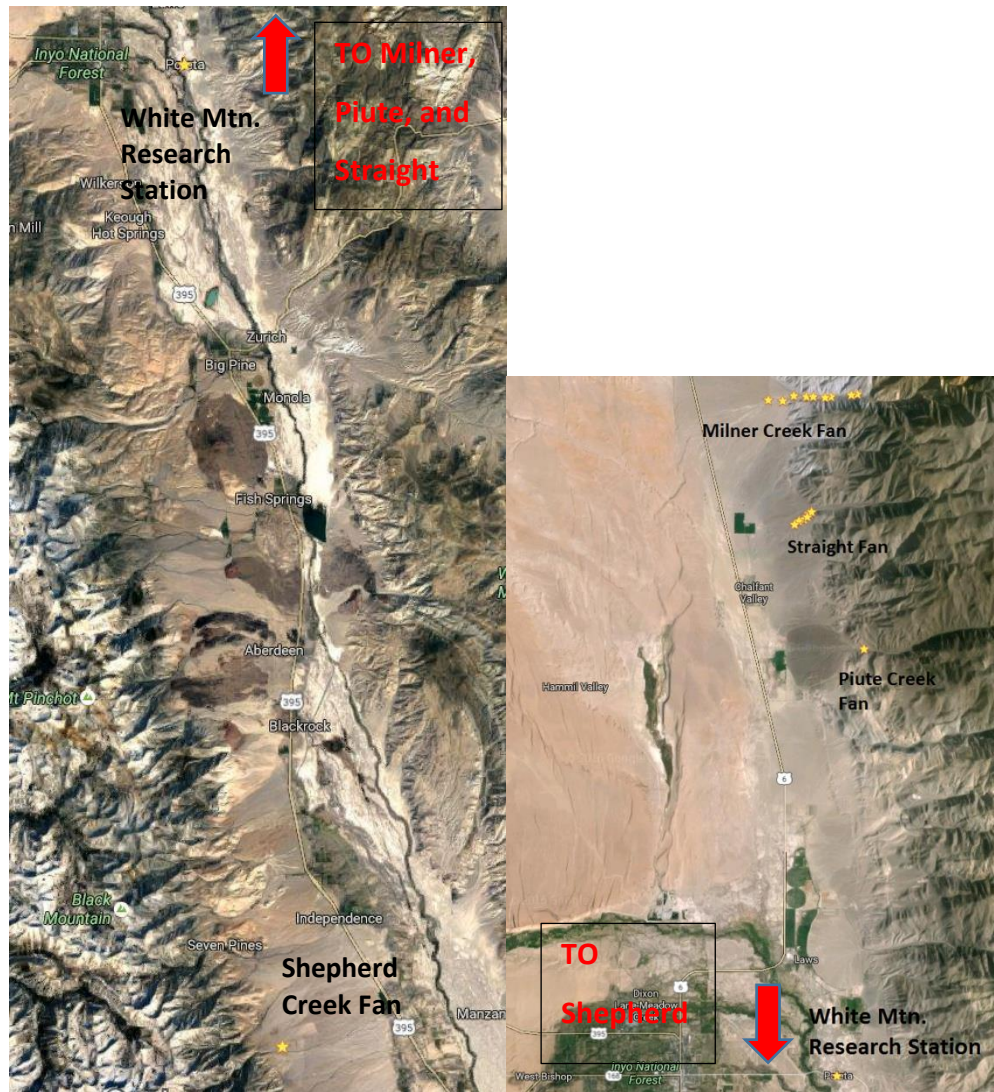


Figure 5-1. Locations of the debris flow fans of interest in this study.

For this study, we focused on 4 different fans, 3 of them located on the White-Inyo range and 1 on the Sierra Nevada. Each fan has its own sediment shed and contains lithology and grain size distributions that may be distinct from those of other sections along the range. Fans were preferentially chosen based on availability of a historical debris flow event and a differing lithology.



Figure 5-2. Milner Creek Fan seen from above. The stars and numbers represent location where either sediment samples were obtained and/or measurements were taken.

Milner Creek is located farthest north out of the fans in this study. There is fluvial influence evidenced in the channels through super elevation on the left bank (looking down fan). Particles are clearly sorted within the channel. There is sage brush and small trees located in the fan with multiple trees buried within. There are 5 different layers evident when looking at the main channel wall near the beginning of the alluvial fan. There was little imbrication evident, meaning these deposits were indeed formed from debris flows.



Figure 5-3. Outcrop from Milner Creek Fan main channel. We note the layering that is displayed.



Figure 5-4. Straight Creek Fan from above. The stars and numbers represent location where either sediment samples were obtained and/or measurements were taken (See appendix for description).

Straight Creek Fan is located directly south of Milner Creek Fan and is covered by a smaller sediment shed than Milner Creek. The deposits contain more boulders and appears by eye to be more clast supported than matrix supported. Milner Creek lacks any

obvious vertical segregation. In the field we witnessed a silt and clay matrix rather than a sandy matrix.



Figure 5-5. Shepherd Creek Fan from above. The star represents the location where we collected soil samples and took a Wolman Count.

Shepherd Creek Fan was the only fan we used for this study that was located in the Sierra Nevadas. The grain size distribution on this fan appeared coarser than the others we investigated with far less silt or clay content. The benefit of using this fan is that we could utilize previous data from *Dünforth et al.* [2007] to determine the approximate geologic timeframe that is related to the fan from radiometric dating. The hydrology during different timeframes formed different flow patterns as debris flows continually built the fan through the Ice Age (data from ~80-20 ka) to how we see it today.



Figure 5-6. Piute Creek Fan from above. The stars and numbers represent location where either sediment samples were obtained and/or measurements were taken (See appendix for description).

Piute fan is located south of Straight and Milner Creek Fan. There is little evidence for recent deposits. In this fan we saw clear evidence of inverse grading. We also observed fewer channels per area compared to other fans we investigated and the few that we investigated on this fan were much deeper than those witnessed at Milner Creek and Straight Creek. The fan contains fewer boulders than Straight Creek. The lithology of the fan is primarily metamorphic silt stone, with some meta- sandstone, volcanic rocks, and granite. There are larger trees nearby the fan as well, indicating the most recent debris flow event was likely older than those on the other fans where no large trees were observable in or around the active channel.

5.3 Fan analysis and discussion

5.3.1 Grain size analysis

At each selected fan, we took either a Wolman Pebble Count [Wolman, 1954] for the coarse grain sizes > 0.2 cm (boulders, cobbles, and pebbles), a soil sample for fine grains (sand, silt and clay), or both to accurately find the grain size distribution as possible.

While these grain size analyses were geared at finding an accurate grain size on the known debris flow events, this has limitations as rain-wash or other fluvial transports may have added more foreign sediment to the original deposits. To avoid this as much as possible, we took soil samples from below large immovable objects, such as boulders and logs. The soil sample locations and descriptions are located within the appendix. In addition, we measured the slope and a height of the flows inside channels and at the “toe” of the debris flows to attempt to discern the relation between these factors and avulsions. These measurements are in the appendix. We focus on the grain size analysis we performed for the results we present here and how we hypothesize we can relate these results to the interstitial fluid viscosity of our experimental flows.

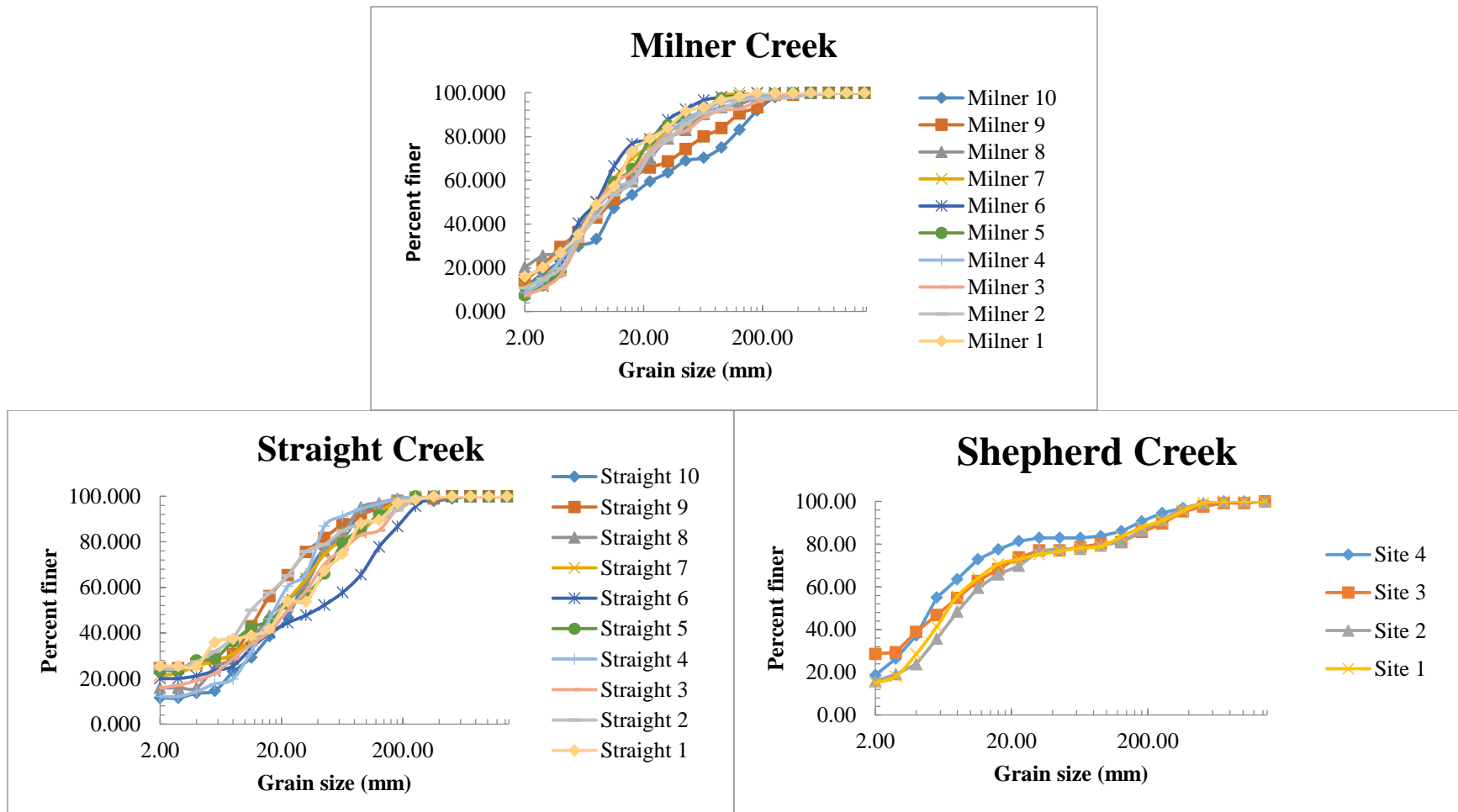


Figure 5-7. The coarse grain size distribution of Straight, Shepherd, and Milner Creek Fans. Note that we did not perform coarse grain analysis (Wolman Test) at Piute Creek Fan.

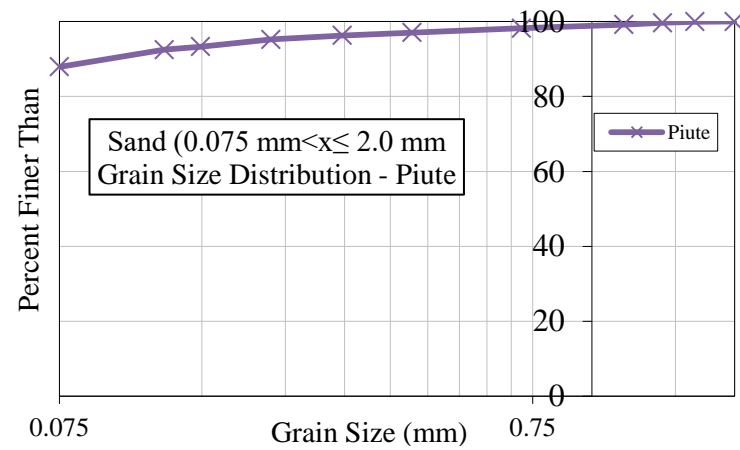
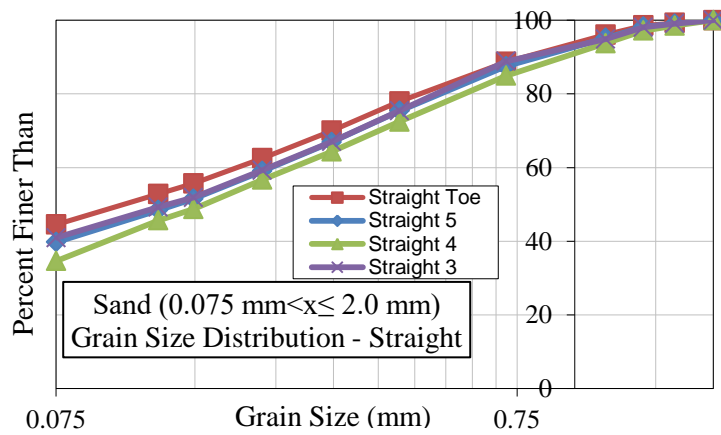
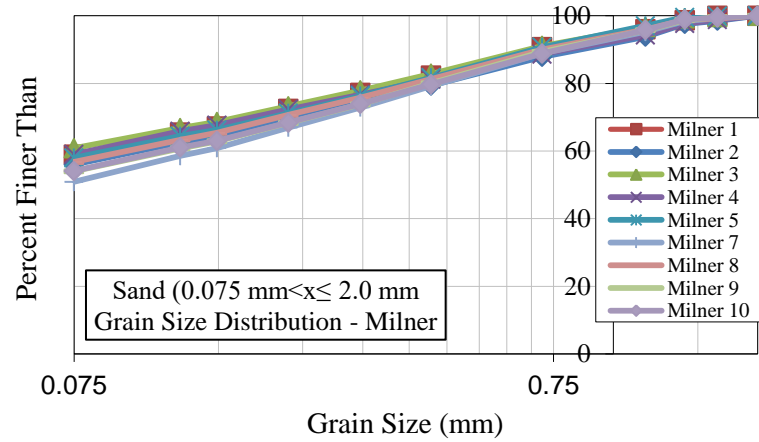
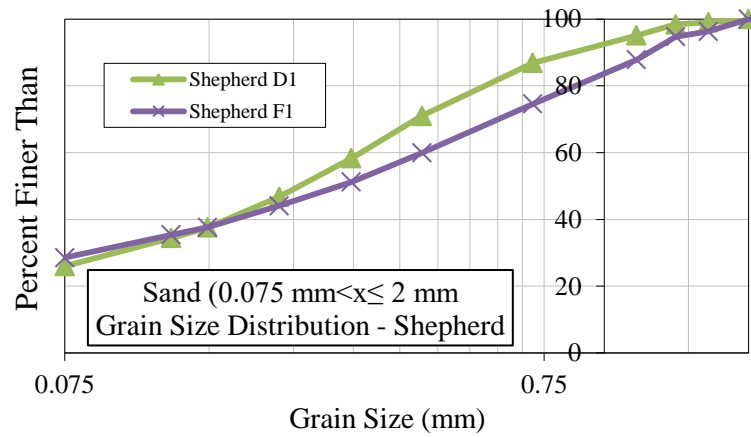


Figure 5-8. Sand Grain Size distribution (0.075 mm to 2.0 mm). The grain size distribution is found here by fine sieves and the data begins at 100% of particles <math>< 2.0\text{ mm}</math> (see **Figure 5-7** for coarse data).

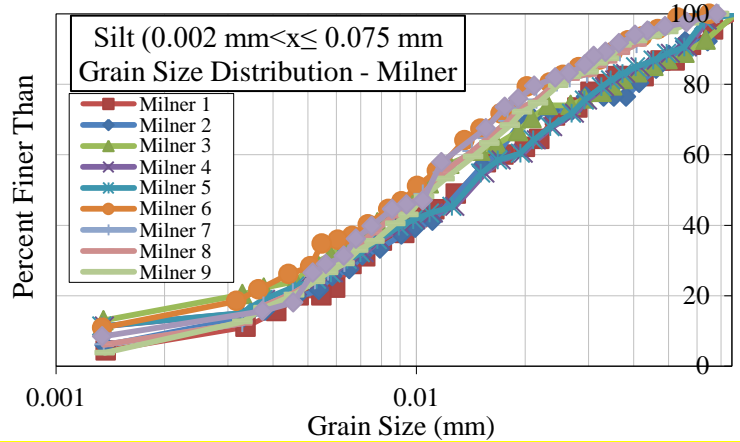
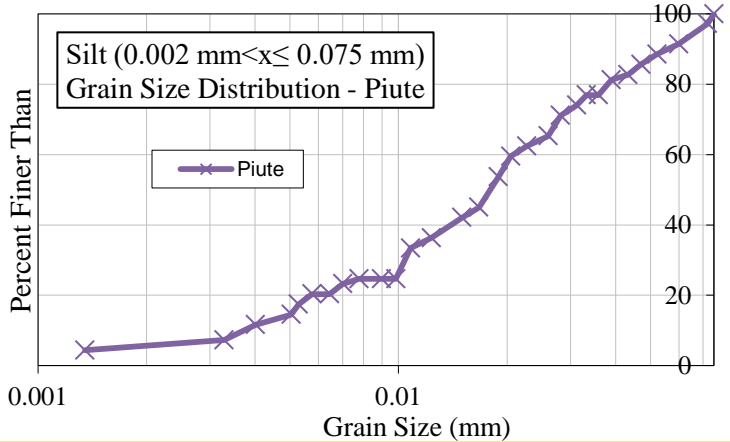
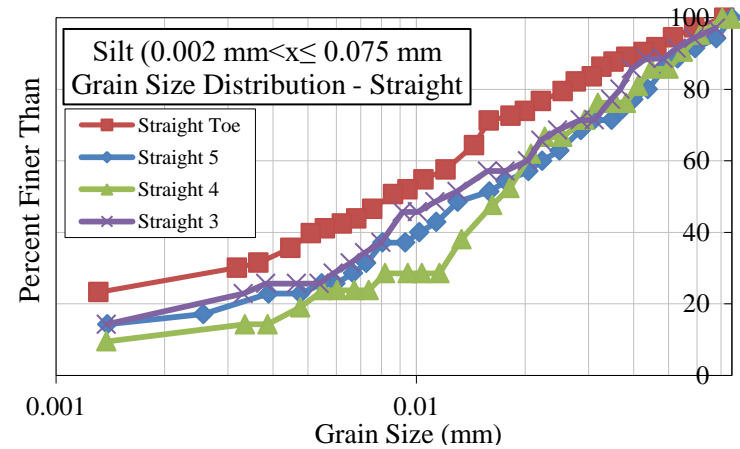
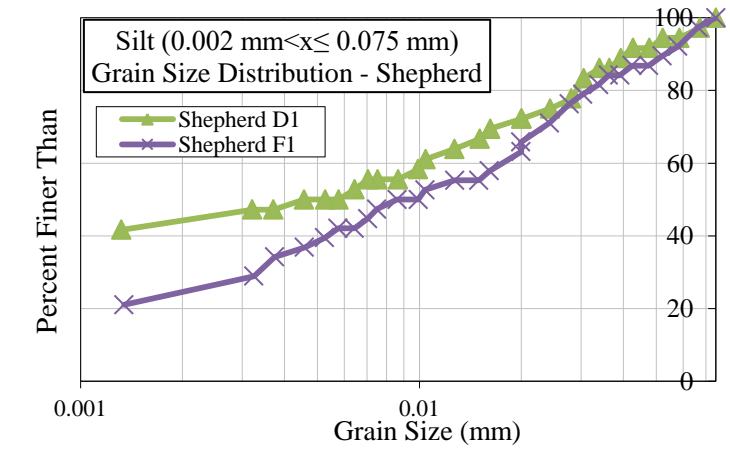


Figure 5-9. Silt grain size distribution. See Figure 38 for coarse data and Figure 39 for sand data.

From the grain size data, we see that Milner Creek contains the highest percentage of coarse grains, followed by Straight Creek Fan, and then Shepherd Creek Fan (Due to time constraints, we did not perform a Wolman count at Piute Creek fan). The greatest sand concentration was at Shepherd Creek fan, followed by Straight canyon, then Milner Creek, and finally Piute Creek fan. The greatest silt concentration was at Piute Creek fan, followed by Milner Creek fan, then Straight Creek fan, and Shepherd Creek fan. There was variation between different sites of the fans; however, this thesis will not focus on the spatial difference between individual fans.

5.3.2 Relation to Lab data

Considering the grain size distributions of these different fans, we can suppose certain details of the behaviors of the flows. Before doing so, we note that minimally we would need to measure the rheology of the fine particle content of these systems mixed with water. More than that, it would be helpful to know the water content of the actual flows, almost impossible for the historic and prehistoric flows that formed these fans. Thus, in this last subsection we present hypotheses of how the fine contents we measured in some of these deposits may have affected the viscosity of their interstitial fluid, their flow behaviors, including erosional and depositional behaviors, and subsequently the details of the channels, levees and tongues of the deposit. First, we note that the deposits that formed Piute Creek Fan had the highest fines content. We hypothesize that these flowed as highly-viscous flows because the grain size distribution was very fines-heavy. In contrast, the largest grains (>2 mm) are from Shepherd Creek Canyon. The fan exhibiting what we consider to be the fewest channels, and likely, the fewest avulsions, was Piute Creek fan; this fan was dominated by very deep developed channels. In contrast, on the Shepherd creek fan, we saw evidence of many avulsions, with somewhat shallower channels. This suggests that as the amount of fines (<0.075 mm) increases, the avulsion probability will decrease. On the other hand, a flow with more greater-than-sand sized particles will tend to avulse more.

We note that these results could simply be a function of something much different causing, for example, differences in levee heights and subsequently differences in repeated debris flow events. Still, because the fans are from similar climate, geographic location, and relief, we believe the lithology and therefore grain size to have an impact on the morphology of a debris flow fan. Regardless, these observations form the basis for a deeper investigation of how fine particle content and the effective interstitial fluid viscosity lead to predictably different flow behaviors and hazard potential.

6 Summary and Outlook

To summarize the primary activities described in this thesis:

- We performed tabletop debris flow experiments to describe and explain the dynamics of wet debris flows in a controlled setting by altering the viscosity of the interstitial fluid. We tracked both the dependence of average and instantaneous entrainment rate with the following findings:
 - **Average:** we found that once the viscosity of the interstitial fluid is increased above that of water (i.e., > 1 cP) increasing it further does not affect the neutral angle.
 - **Instantaneous:** we found that the experiments performed with higher interstitial fluid viscosities resulted in the deepest *instantaneous* values of entrainment, the highest maximum shear stress, and the highest *instantaneous* excess pore fluid pressure. The timing and magnitude of these behaviors varied together with viscosity, displaying that viscosity of the interstitial fluid does affect *instantaneous* debris flow dynamics.
- Using high-speed video and tracking programs, we measured quantities for debris flow continuum theory including a flow hydrograph, entrainment depth, entrainment rate, shear stress, Reynold's shear stress, and granular temperature.
- We utilized basal pore fluid pressure sensors in the erodible bed of the debris flow apparatus that measured the pore fluid pressure that existed within the debris flow through the extent of flow.
- We investigated a variety of physical mechanisms that could have been driving the debris flow movement and entrainment, specifically: shear stress, granular temperature, and pore fluid pressure.

- Among these three mechanisms, we found a correlation only between entrainment rate and *excess* pore fluid pressure

In the future, there are numerous different directions to pursue. Because these data only delve into a few cases for study, more experiments to eliminate any discrepancies between real and pseudo correlations would be an important first step to further analyze the relationships found within this thesis. Another avenue of study would be to develop the tracking code in both dry and wet experiments. In dry experiments, developing a way to track multiple sized particulate would be a huge step into simulating real debris flows in nature. In wet flows, a more exact measurement of the height of the fluid layer would be useful for more accurately and precisely relating sensor data to high speed camera results.

We note that in these studies, unlike previous studies on dry granular flows, we did not find any correlation between shear stress and entrainment rate or granular temperature and entrainment rate. Because there are previous explanations describing these mechanisms as effectors to flow dynamics, it would be useful and interesting to more deeply investigate the potential correlation. Because these mechanisms differ in timescale from entrainment dynamics, perhaps there are dynamics within the flow, particularly the flow front, which have not yet been observed or explained. We have procured a larger flume within our group that could limit some of the effects of using a small flume, and repeating these experiments on that flume could provide scaling and confirmation of findings within this thesis. This new flume also could provide variation in the direction perpendicular to the flow direction and simulate a true 3-dimensional flow, including flow margin and more natural flow front dimensions. However, we feel confident that this flume can yield further results about the physics of particle-particle and particle-fluid interactions and how they vary with different time scale ratios noted in Table 2.8.

References

- Bagnold, R. A. (1954, August). Experiments on a gravity-free dispersion of large solid spheres in a Newtonian fluid under shear. *In Proceedings of the Royal Society of London A: Mathematical, Physical and Engineering Sciences* (Vol. 225, No. 1160, pp. 49-63). The Royal Society.
- Berger, C., B. W. McArdeell, and F. Schlunegger (2011) Direct measurement of channel erosion by debris flows, Illgraben, Switzerland. *Journal of Geophysical Research-earth Surface* 116.
- Berti, M., R. Genevois, R. LaHusen, A. Simoni, and P. R. Tecca (2000) Debris flow monitoring in the Acquabona watershed on the Dolomites (Italian Alps). *Phys. Chem. Earth Part B* 25(9), 707– 715.
- Bouchut, F., E. D. Fernandez-Nieto, A. Mangeney, and G. Narbona-Reina (2014) A two-phase shallow debris flow model with energy balance, *Math. Model. Num. Analy.*, accepted.
- Buckingham, E., (1914), “On the foundations of Similar Systems: Illustrations of the Use of Dimensional Analysis”, *Physical Review*, 4 (4): 345-376.
- Cassar, C., M. Nicolas, O. Pouliquen (2005) Submarine granular flows down inclined planes, *Physics of Fluids* 17, 103301 (2005); doi: 10.1063/1.2069864
- Cheng, N. S. (2008). Formula for the viscosity of a glycerol– water mixture. *Industrial & engineering chemistry research*, 47(9), 3285-3288.
- Coussot, P., S. Proust, and C. Ancey (1996) Rheological interpretation of deposits of yield stress fluids, *Journal of Non-Newtonian Fluid Mechanics.*, 66(1), pg. 55-70 doi: 10.1016/0377-0257(96)01474-7
- Darcy, H. (1856). Les fontaines publiques de la ville de Dijon. Paris: Dalmont.
- de Haas, T., L. Braat, J. R. F. W. Leuven, I. R. Lokhorst, and M. G. Kleinhans (2015), Effects of debris flow composition on runout, depositional mechanisms, and deposit morphology in laboratory experiments, *J. Geophys. Res. Earth Surf.*, 120, 1949–1972, doi:10.1002/2015JF003525.

- Dühnforth, M., A. L. Densmore, S. Ivy-Ochs, P. A. Allen, and P. W. Kubik (2007), Timing and patterns of debris flow deposition on Shepherd and Symmes creek fans, Owens Valley, California, deduced from cosmogenic ^{10}Be , *J. Geophys. Res.*, 112, F03S15, doi: 10.1029/2006JF000562.
- Egashira, S., N. Honda, and T. Itoh (2001) Experimental study on the entrainment of bed material into debris flow. *Phys. Chem. Earth, Part C* 26(9), 645– 650.
- Enos, P. (1977), Flow regimes in debris flow, *Sedimentology* 24(1), pg.133-142. Doi: 10.1111/j.1365-3091.1977.tb00123.x
- Farin, M., A. Mangeney, and O. Roche (2014), Fundamental changes of granular flow dynamics, deposition, and erosion processes at high slope angles: Insights from laboratory experiments, *J. Geophys. Res. Earth Surf.*, 119(3), 504-532, doi:10.1002/2013JF002750.
- Floris, M., A. D'Alpaos, C. Squarzoni, R. Genevois, and M. Marani (2010) Recent changes in rainfall characteristics and their influence on thresholds for debris flow triggering in the Dolomitic area of Cortina d'Ampezzo, north-eastern Italian Alps. *Nat. Hazards Earth Syst. Sci.*, 10, 571–580.
- Forterre, Y., & Pouliquen, O. (2008). Flows of dense granular media. *Annu. Rev. Fluid Mech.*, 40, pg. 1-24. Doi: 40.111406.102142
- Fraccarollo, L., & Papa, M. (2000). Numerical simulation of real debris-flow events. *Physics and Chemistry of the Earth, Part B: Hydrology, Oceans and Atmosphere*, 25(9), 757-763.
- Giola, G., S. E. Ott-Monsivais, and K. M. Hill (2006), Fluctuating Velocity and Momentum Transfer in Dense Granular Flows, *Phys. Rev. Lett.*, 96(13), 138001.
- Herschel, W. H., & Bulkley, R. (1926, June). Measurement of consistency as applied to rubber-benzene solutions. *In Am. Soc. Test Proc* 26(2), pg. 621-633.
- Hill, K. M., G. Giola, and V. V. Tota (2003), Structure and Kinematics in Dense Free-Surface Granular Flow, *Phys. Rev. Lett.*, 91(6), 064302.
- Hungr, O., D.F. VanDine, D.R. Lister, Debris Flow Defenses in British Columbia (1987), Geological Society of America, Volume VII, pg. 202-222. doi: 10.1130/REG7-p201
- Hungr, O., S. McDougall, and M.J. Bovis (2005) Entrainment of material by debris flows. Chapter 7. *In Hazard assessment of debris flows and related phenomena*. Edited by M. Jakob and O. Hungr. Praxis-Springer Publishers, Heidelberg pp135-158.
- Iverson, R. M. (1997), The physics of debris flows, *Rev. Geophys.*, 35(3), 245, doi:10.1029/97RG00426.

- Iverson, R. M., and R. P. Denlinger (2001) Flow of variably fluidized granular masses across three-dimensional terrain 1. Coulomb mixture theory. *Journal of Geophysical Research* 106, 537 - 552.
- Iverson, R. M. (2003). The debris-flow rheology myth. *Debris-flow hazards mitigation: mechanics, prediction, and assessment*, 1, 303-314.
- Iverson, R. M., Logan, M., LaHusen, R. G., & Berti, M. (2010). The perfect debris flow? Aggregated results from 28 large-scale experiments. *Journal of Geophysical Research: Earth Surface*, 115(F3).
- Iverson, R. M., M. E. Reid, M. Logan, R. G. LaHusen, J. W. Godt, and J. P. Griswold (2011), Positive feedback and momentum growth during debris-flow entrainment of wet bed sediment, *Nat. Geosci.*, 4(2), 116–121, doi:10.1038/ngeo1040.
- Iverson, R. M. (2012), Elementary theory of bed-sediment entrainment by debris flows and avalanches, *J. Geophys. Res. Earth Surf.*, 117(3), 1–17, doi:10.1029/2011JF002189.
- Iverson, R. M., and C. Ouyang (2015), Entrainment of bed material by Earth-surface mass flows: Review and reformulation of depth-integrated theory, *Rev. Geophys.*, 53, 27–58, doi:10.1002/2013RG000447.
- Johnson, A. M. (1965). A model for debris flow: a thesis in geology. *Pennsylvania State University*.
- Kaitna, R., M. M. Palucis, K. M. Hill, and W. E. Dietrich (2016), Effects of Coarse Grain Size Distribution and Fine Particle Content on Pore Fluid Pressure and Shear Behavior in Experimental Debris Flows, *J. Geophys. Res. Earth Surf.*, 120, doi: 10.1002/2015JF003725.
- Major, J. J., & Pierson, T. C. (1992). Debris flow rheology: Experimental analysis of fine-grained slurries. *Water resources research*, 28(3), 841-857. doi: 10.1029/91WR02834
- Major, J. J., & Iverson, R. M. (1999). Debris-flow deposition: Effects of pore-fluid pressure and friction concentrated at flow margins. *Geological Society of America Bulletin*, 111(10), 1424-1434. doi: 10.1130/0016-7606(1999)111
- Mangeney, A., Tsimring, L. S., Volfson, D., Aranson, I. S., & Bouchut, F. (2007). Avalanche mobility induced by the presence of an erodible bed and associated entrainment. *Geophysical Research Letters*, 34(22).
- Mangeney, A., O. Roche, O. Hungr, N. Mangold, G. Faccanoni, and A. Lucas (2010), Erosion and mobility in granular collapse over sloping beds, *J. Geophys. Res. Earth Surf.*, 115(3), 1-21, doi:10.1029/2009JF001462.

- McArdell, B. W., P. Bartelt, and J. Kowalski (2007) Field observations of basal forces and fluid pore pressure in a debris flow. *Geophys. Res. Lett.* 34, L07406.
- McCoy, S.W., J.W. Kean, J.A. Coe, G.E. Tucker, D.M. Staley, and T.A. Wasklewicz (2012), In situ measurements of sediment entrainment from the headwaters of a steep catchment, *J. Geophys. Res.-Earth Surf.*, 117, F03,016, doi:10.1029/2011JF002278.
- GDR Midi (2004), On Dense Granular Flows, *The European Physical Journal E*, 41, 341-365, doi: 10.1140/epje/i2003-10153-0
- Moberly, D. (2015), Laboratory Experiments Investigating Entrainment by Debris Flows, M.S. thesis, Department of Civil, Environmental, and Geo-Engineering, University of Minnesota, 86 pp.
- Mueller, R. & Loew, S. (2009) , Swiss Predisposition and cause of the catastrophic landslides of August 2005 in Brienz (Switzerland), *J. Geosci.* 102(2), pg. 331-344. doi:10.1007/s00015-009-1315-3
- Phillips, C.J., T. R. H. Davies (1991), Determining rheological parameters of debris flow material, *Geomorphology*, 4(2), pg. 101-110. doi: 10.1016/0169-555X(91)90022-3
- Pierson, T. C. (1981). Dominant particle support mechanisms in debris flows at Mt Thomas, New Zealand, and implications for flow mobility. *Sedimentology*, 28(1), pg. 49-60. doi: 10.1111/j.1365-3091.1981.tb01662.x
- Pierce, J. L., G.A. Meyer, and A.J.T. Jull (2004) Fire-induced erosion and millennial-scale climate change in northern ponderosa pine forests. *Nature* 432, 87 - 90.
- Pierson, T. C., & Costa, J. E. (1987). A rheologic classification of subaerial sediment-water flows. *Reviews in Engineering Geology*, 7, pg.1-12. doi: 10.1130/REG7-p1
- Pitman, E. B., & Le, L. (2005). A two-fluid model for avalanche and debris flows. *Philosophical Transactions of the Royal Society of London A: Mathematical, Physical and Engineering Sciences*, 363(1832), 1573-1601.
- Rickenmann, D., Weber, D., & Stepanov, B. (2003). Erosion by debris flows in field and laboratory experiments. *Debris-flow hazards mitigation: mechanics, prediction, and assessment*, 883-894.
- Savage, S.B. and R.M. Iverson (2003). Surge dynamics coupled to pore-pressure evolution in debris flows. *Proc. 3rd Int. Conference on Debris-Flow Hazards*.
- Schürch, P., A. L. Densmore, N. J. Rosser, and B. W. McArdell (2011), Dynamic controls on erosion and deposition on debris-flow fans, *Geology*, 39, 827–830.
- Shieh, C.-L., C.-D. Jan, and Y.-F. Tsai (1996) A Numerical Simulation of Debris Flow

and Its Application. *Natural Hazards* 13, 39 - 54.

Stiny, J. (1910). Die Muren [Debris flows]. *Wagnerschen Univ.*, [English translation, EBA Consult., Vancouver, Canada, 1997.].

Stock, J. D., and W. E. Dietrich (2003) Valley incision by debris flows: evidence of a topographic signature. *Water Resources Research* 39(4), 1089 – 1104.

Stoffel, M., and M. Beniston (2006) On the incidence of debris flows from the early Little Ice Age to a future greenhouse climate: A case study from the Swiss Alps. *Geophys. Res. Lett.* 33, L16404.

Tai, Y. C., & Kuo, C. Y. (2008). A new model of granular flows over general topography with erosion and deposition. *Acta Mechanica*, 199(1), pg. 71-96. doi: 10.1007/s00707-007-0560-7

Terzaghi, K. (1943). Theory of consolidation (pp. 265-296). *John Wiley & Sons, Inc.*.

Takahashi, T. (1981), Debris flow, *Annu. Rev. Fluid Mech.*, 13(1), 57–77, doi:10.1146/annurev.fl.13.010181.000421.

Varnes, D. J. (1978). Slope movement types and processes. *Special report*, 176, pg. 11-33.

Whipple, K.X, and T. Dunne, (1992) The Influence of debris-flow rheology on fan morphology, Owens Valley, California, *Geological Society of America Bulletin*, v. 104, p. 887-900

Wolman, M. Gordon, (1954) A method of sampling coarse river-bed material, *Earth and Space Science News*, 35(6), pg. 951-956. Doi: 10.1029/TR035i006p00951

Yano, K., & Daido, A. (1965). Fundamental study on mud-flow. *Bulletin of the Disaster Prevention Research Institute*, 14(2), pg. 69-83.

Yohannes, B., Hsu, L., Dietrich, W. E., & Hill, K. M. (2012). Boundary stresses due to impacts from dry granular flows. *Journal of Geophysical Research: Earth Surface*, 117(F2). doi: 10.1029/2011JF002150

Appendix

I. Definition of symbols

θ = angle of inclination of flume [°]	k_{HB} = consistency index [Pa]
θ_n = neutral angle [°]	k_B = plastic viscosity [cP]
a = power law exponent	μ_c = colomb friction coef.
b = particle for integration []	μ_{fl} = fluid viscosity [cP]
B_y = horizontal bin []	m_s = supply mass [kg]
C = ratio of yield stress to reference pressure []	m_o = eroded mass [kg]
d = bead diameter [m]	m_e = net mass erosion [kg]
D = hyd. Diffusivity [m^2/s]	N_P = ratio of length to diffusivity []
\dot{e} = entrainment rate [m/s]	N_t = number of beads
ε = length scale []	N_R = Reynolds parameter []
F = net force over a debris flow [N]	P = pore fluid pressure [Pa]
F_{tot} = Total local force [N]	p_{bed} = Est. basal pore pressure [Pa]
f = solid volume fraction []	P_{calc} = Pore fluid pressure based on high speed camera using ρ_f [Pa]
f_{crit_DFL} = Critical volume fraction for the dense flowing layer []	P_{calc}' = Pore fluid pressure calculation based on high speed camera using ρ_f in dense flowing layer using ρ_s and ρ_f in top fluid layer [Pa]
f_{crit_top} = Critical volume fraction for the top fluid layer []	P_{calc}'' = Pore fluid pressure calculation based on high speed camera using ρ_s and ρ_f in top fluid layer and dense flowing layer [Pa]
g = acceleration due to gravity [m/s^2]	P_e = Excess Pore fluid pressure [Pa]
$\dot{\gamma}$ = shear rate [s^{-1}]	P_e' = Excess Pore fluid pressure based on high speed camera using ρ_f in dense flowing layer using ρ_s and ρ_f in top fluid layer [Pa]
H = entrainment height [m]	P_e'' = Excess Pore fluid pressure based on high speed camera using ρ_s and ρ_f in top fluid layer and dense flowing layer [Pa]
H_{max} = Maximum flow height [m]	
H_o = initial height of the bed [m]	
h_{DFL} = thickness of dense flowing layer [m]	
h_b = height of a bin [m]	
h_{top} = Thickness of the top fluid layer [m]	
IP = initial position []	
i = image []	
I = inertial number []	

P_{hyd} = Hydrostatic pore fluid pressure [Pa]	Δt = timestep [s]
P_{sen} = Pore fluid pressure recorded from the weighted average of 2 sensors (equal to S_{avg}) [Pa]	t = time [s]
P_{top_f} = Pore fluid pressure in the top fluid layer [Pa]	t_s = adjusted starting time [s]
P_{DFL_f} = Pore fluid pressure in the dense flowing layer [Pa]	T = granular temperature
P_{st_f} = Pore fluid pressure in stationary layer [Pa]	τ = basal shear stress [Pa]
Q = Excess shear stress ratio	τ_R = Reynold's Shear Stress [Pa]
ρ = bulk density [kg/m^3]	τ_y = yield stress [Pa]
ρ_0 = reference density [kg/m^3]	u = horizontal velocity [m/s]
ρ_s = density of particles [kg/m^3]	u_{crit} = critical horizontal velocity [m/s]
ρ_f = Interstitial fluid density [kg/m^3]	u' = hor. velocity fluctuations [m/s]
R = Ratio of ref. density to bulk dens. []	$\overline{u'u'}$ = avg. hor. Vel. fluctuations [m/s]
R_f = Ratio of fluid dens. to bulk dens. []	v = vertical velocity [m/s]
σ_{bed} = Estimated basal normal stress [Pa]	v' = vert. velocity fluctuations [m/s]
σ_{eff} = effective stress [Pa]	$\overline{v'v'}$ = avg. vert. vel. fluctuations [m/s]
σ_{tot} = normal stress from ρ [Pa]	V = volume of bin [m^3]
S = Savage number []	Y = ratio of yield stress to reference pressure []
$S\#$ = pore pressure sensor #	y = vertical position [m]
S_{avg} = Weighted average from pore pressure sensor (equal to P_{sen})	y_{DFL} = top of dense flowing layer [m]
	y_{ucrit} = top of the fluid layer [m]
	y_{top} = top of the fluid layer
	ζ = Percentage in suspension []

II. Field Locations and descriptions

Milner Creek Fan

Location	UTM coords	Elevation (m)	Levee or Lobe?	Matrix Sample? (Sample Label)	Walman count?	Dominantly fine or coarse?	Matrix or clast supported	Height	Slope	Width	Other Description
Milner-1 (April 22, 2016)	383654 416193 7	1938	Levee	YES (Milner -1)	YES	silt or silt clay matrix (very little sand)	Matrix				Taken from below 2 m log at downstream end of transect – clearly in place on Right bank
Milner-2 (April 22, 2016)	383404 416193 3	1911	Levee	YES (Milner -2)	YES						Taken below log along Right flow margin at downstream end of levee deposit
Milner-3 (April 22, 2016)	382621 416189 5	1829	Levee	YES (Milner -3)	YES						Taken from under 1.4 m log on Right flow margin near upstream end of GSD transect

Milner-4 (April 22, 2016)	382389 416187 2	1817	Lobe	YES (Milner -4)	YES			1.2 ± 0.1 m	0.87 m in 10 m	21.3 m	Taken from below 0.8 m boulder embedded in 1952 flow front, 0.5 m below flow top
Milner-5 (April 23, 2016)	381954 416189 7	1765	Levee	YES (Milner -5)	YES						Taken from below 1 m long log at Right edge of flow margin
Milner-6 (April 23, 2016)	381671 416191 7	1733	Lobe	YES (Milner -6)	YES			0.6 m ± 0.1	0.85m in 10 m	9.23 m at widest point	Taken from Right margin of surge lobe, 15 cm below the surface in a vertical water-worn cut
Milner-7 (April 23, 2016)	381200 416196 6	1691	Levee	YES (Milner -7)	YES						Taken from 0.4 m below fan surface
Milner-8	380770 416180	1648	Levee	YES (Milner -8)	YES						Taken from below 1.4 m log embedded in

(April 23, 2016)	3										flow top
Milner-9 (April 23, 2016)	380219 416186 1	1596	Levee	YES (Milner -9)	YES						Taken from under 0.6 m boulder on Left levee margin, 0.4 m below levee top
Milner-10 (April 23, 2016)	380542 416188 9	1632	Lobe	YES (Milner -10)	YES			0.8 m \pm 0.1	0.85 m in 10 m	16.8 \pm 0.2 m	Taken from under 0.6 m boulder on Left levee margin, 0.6 m below flow surface at surge front
A1 (April 17, 2016)	380737 416177 6	1632	Lobe	NO	NO			0.45 \pm 0.5 m	5.97 ^o - M 5.64 ^o -L 5.57 ^o - R	12.6 (10 \pm 0.1) m	

Straight Creek Fan

Location	UTM coordinates	Elevation (m)	Levee or Lobe?	Matrix Sample? (Sample Label)	Walman count?	Dominantly fine or coarse?	Matrix or clast supported ?	Height	Slope	Width	Other Description
Straight-1 (April 22, 2016)	0381817 4157530	1551	Lobe	NO	YES						1918 flow?
Straight-2 (April 22, 2016)	0381816 4157532	1565	Levee	NO	YES						1918 flow?
Straight-3 (April 22, 2016)	0381728 4157467	1548	Levee	YES (Straight-3)	YES		Matrix				
Straight-4 (April 22, 2016)	0381638 4157333	1528	Levee	NO	YES						
Straight-5 (April 22, 2016)	0381512 4157255	1503	Levee	YES (Straight-4)	YES		Matrix				
Straight-6 (April 22, 2016)	0381357 4157182	1476	Levee	NO	YES						1918 flow?

Straight-7 (April 22, 2016)	0381328 4157184	1470	Levee	YES (Straight-5)	YES		Clast				
Straight-8 (April 22, 2016) Same lobe as Straight- 9	0381155 4157066	1446	Lobe	NO	YES			1.10 ±0.10 m	7.29° - M, 3.89° - L; 3.57° - R	20.2 ± 0.5 m	Lower Transe ct
Straight-9 (April 22, 2016) Same lobe as Straight- 8	0381160 4157068	1445	Lobe	NO	YES			1.10 ±0.10 m	7.29° - M, 3.89° - L; 3.57° - R	20.2 ± 0.5 m	Upper Transe ct
Straight-10 (April 22, 2016) Same lobe as Straight- 11	0380919 4157066	1411	Lobe	YES (Straight-TOE)	YES		Clast	0.60 ± 0.05 m	6.17° - M, 6.97° - R; 4.32° - L	23.1 ± 0.1 m	Lower Transe ct

Straight-11 (April 22, 2016) Same lobe as Straight-10	0380929 4157070	1412	Lobe	NO	YES			0.60 ± 0.05 m	6.17° - M, 6.97° - R; 4.32° - L	23.1 ± 0.1 m	Upper Transe ct
A1 – April 18 Same lobe as Straight-8 and 9	381144 4157071	1444	Lobe	NO	NO			1.10 ± 0.10 m	7.29° - M, 3.89° - L; 3.57° - R	20.2 ± 0.5 m	
A2 – April 18 Same lobe as Straight-11 and 12	380911 4157071	1404	Lobe	NO	NO	Coarse (50 cm)	Clast	0.60 ± 0.05 m	6.17° - M, 6.97° - R; 4.32° - L	23.1 ± 0.1 m	

Piute Creek Fan

Location	UTM coordinates	Elevation (m)	Levee or Lobe?	Matrix Sample? (Sample Label)	Walman count?	Dominantly fine or coarse?	Matrix or clast supported?	Height	Slope	Width	Other Observations
Piute-1	382956 415232 6	1565	Levee	YES (Piute)	NO		Clast				Large streamcut on Right bank of active channel. Positioned top of cut along edge of Chalfant Loop Road

Shepherd Creek Fan

Location	UTM coordinates	Elevation (m)	Levee or Lobe?	Matrix Sample? (Sample Label)	Walman count?	Matrix or clast supported	Other Observations
Shepherd-1 (Lobe D)	389124 4065249	1669	Levee	NO	NO		Position on Right levee crest of channel
Shepherd-2	389142	1668	Levee	YES	NO	Sediment is clast	Taken from Left bank levee of S channel of

(Lobe D)	4065299			(Shepherd-D1)		supported; cobble-boulder conglomerate; boulder dominantly 0.2 – 0.8 m to 1.3 m; matrix is silty very fine-fine sand; dark to medium brown in color	Surface D Below 80 cm granite boulder set into Left channel wall, within 0.5 m of channel bed and 1.3 ± 0.1 m below levee crest
Shepherd-3 (Lobe D)	388959 4065122	1678	Lobe	NO	YES		Lower Transect
Shepherd-4 (Lobe D)	388947 4065114	1680	Lobe	NO	YES		Upper Transect
Shepherd-5 (Lobe E)	390119 4065556	1575	Lobe	NO	YES		Lower Transect
Shepherd-6 (Lobe E)	390112 4065547	1579	Lobe	NO	YES		Upper Transect
Shepherd-7 (Lobe F)	388642 4064356	1703	Levee	YES (Shepherd-F1)	NO		Taken from Right bank of Shepherd creek at gauging station downstream of road crossing, station marked (on dam) "5-20-98" in Dühnforth's active lobe F Taken 1.2 m below Right bank top in clast supported, massive cobble-boulder